

Microemulsion: Prediction of the Phase diagram with a modified Helfrich free energy



MAX-PLANCK-GESELLSCHAFT



Harsha Mohan Paroor

Max Planck Institute for Polymer Research Mainz, Germany and
Johannes Gutenberg University, Mainz, Germany

A thesis submitted for the degree of
Doctor of Philosophy in Natural Sciences

May 2012

I would like to dedicate this thesis to all my teachers...

Abstract

Microemulsions are thermodynamically stable, macroscopically homogeneous but microscopically heterogeneous, mixtures of water and oil stabilised by surfactant molecules. They have unique properties like ultralow interfacial tension, large interfacial area and the ability to solubilise other immiscible liquids. Depending on the temperature and concentration, non-ionic surfactants self assemble to micelles, flat lamellar, hexagonal and sponge like bicontinuous morphologies. Microemulsions have three different macroscopic phases (a) 1Φ -microemulsion (isotropic), (b) 2Φ -microemulsion coexisting with either expelled water or oil and (c) 3Φ -microemulsion coexisting with expelled water and oil.

One of the most important fundamental questions in this field is the relation between the properties of the surfactant monolayer at water-oil interface and those of microemulsions. This monolayer forms an extended interface whose local curvature determines the structure of the microemulsions. The main part of my thesis deals with the quantitative measurements of the temperature induced phase transitions of water-oil-nonionic microemulsions and their interpretation using the temperature dependent spontaneous curvature ($c_0(T)$) of the surfactant monolayer. In a 1Φ -region, conservation of the components determines the droplet (domain) size (R) whereas in 2Φ -region, it is determined by the temperature dependence of $c_0(T)$. The Helfrich bending free energy density includes the dependence of the droplet size on $c_0(T)$ as $F = \frac{2\kappa\phi_s}{l_s R^2} \left\{ [1 - Rc_0(T)]^2 + \frac{\bar{\kappa}}{2\kappa} \right\}$ where l_s is the effective length of a surfactant molecule, κ and $\bar{\kappa}$ are the bending and Gaussian moduli. However, this approach cannot account for the 3Φ

region. Therefore, a modified Helfrich equation is proposed which describes the three macroscopic phases. It assumes that within a well defined temperature interval two spontaneous curvatures coexist. The consequences of this assumptions are investigated. As model systems, a moderate and a weak surfactant (short-chain) microemulsions are used. Systematic scattering and calorimetry experiments were conducted to predict the phase behaviour and thereby to investigate the validity of this assumption.

A quantitative prediction of the concentration dependence of the phase transition temperatures for 1Φ -, 2Φ - and 3Φ - microemulsions is one of the highlights of my work. For this purpose, microemulsions with different ratios of the components have been studied. A relation between the temperature dependency of the spontaneous curvature and the hydration of surfactant is facilitated. The generalised description for water-oil-surfactant system using the modified 'Helfrich bending free energy' is shown to be a successful concept. The experiments lead to a clear picture of the validity of the modified Helfrich bending free energy for a wide range of surfactants and phase transitions in these systems.

Contents

Contents	vi
List of Figures	ix
1 Introduction	1
1.1 Motivation and Objectives	1
1.2 Surfactants and Classification	2
1.3 Surfactants in water	5
1.4 Surfactants in non-polar solvent (oil)	6
1.5 Different morphologies of surfactant aggregates	7
1.6 Helfrich free energy	11
1.7 Emulsions	16
1.8 Microemulsions	17
1.9 Phase Behavior of Microemulsion	18
1.9.1 Gibbs phase triangle	18
1.9.2 Fish cut phase diagram	21
1.9.3 Strong and weak surfactant	23
1.10 Concepts and Theoretical Modeling of Microemulsions	24
1.11 Free energy discussions for the non-ionic microemulsion	28
1.12 Size of droplets	29
1.12.1 One Phase Region	29
1.12.2 Two Phase Region	30
1.13 Linear dependence of c_0 with T	33
1.14 Emulsification boundary - 1Φ meets 2Φ region	35
1.15 Nucleation and phase separation	36

1.16 Specific Heat	37
2 Materials and Experimental Techniques	40
2.1 Materials	40
2.2 Phase behavior studied with thermo stated water bath	41
2.2.1 Apparatus	41
2.2.2 Procedures to determine phase behavior	42
2.3 Differential Scanning Calorimetry	43
2.3.1 Apparatus	44
2.3.2 Sample	44
2.3.3 Procedures to determine the step in the specific heat	45
2.4 Dynamic Light Scattering (DLS)	46
2.4.1 DLS Theory	47
2.4.2 Experimental set up	49
2.4.3 Sample preparation for DLS	50
2.5 Tensiometry	51
2.5.1 Critical Micelle Concentration (CMC)	51
2.5.2 Wilhelmy Plate method	52
2.5.3 du Noüy ring method	53
3 Experimental Results and Discussions	55
3.1 Phase Behaviour	55
3.2 Phase behavior of water-decane- C_8E_3	56
3.2.1 Phase Diagram of microemulsion samples of fixed water to oil ratio (fish cut)	56
3.2.2 Phase Diagram of samples with fixed Surfactant Concentration	58
3.3 Experimental Results : DSC of water-decane- C_8E_3	60
3.3.1 Comparison of the phase transition temperature determined from turbidity measurements and DSC	66
3.4 Experiment Results of DLS	67
3.4.1 Calculated versus measured domain size	68
3.5 Results from Tensiometry	70

3.6	Validating the predictions to the phase boundaries	75
3.6.1	Fitting and the Material Parameters: R_w^{mic} , T_l , a_w , R_o^{mic} , T_u and a_o	75
3.6.2	Interfacial surfactant after the CMC correction	76
3.6.3	Microemulsion with equal proportion of water and decane (1:1)	76
3.6.4	Microemulsion with 3:7 and 7:3 water to decane ratio . . .	78
3.7	Prediction of the phase boundaries	81
3.8	Coexistence of the curvatures and the interpretation of the curva- ture plot for C_8E_3	86
3.9	Prediction of the step of the specific heat	90
3.10	Predictions to weak surfactant microemulsion water-octane- C_4E_1 .	96
4	Conclusions	97
	Appendix A	99
	Appendix B	100
.0.1	The height of the specific heat-step at the emulsification boundary	100
	References	103

List of Figures

1.1	Schematic diagram of a surfactant molecule. Here the red circle represents the hydrophilic head while the blue chain represents the hydrophobic tail.	2
1.2	Surfactant classification according to the nature of the hydrophilic group and examples. The red colored part represents the hydrophilic head and the blue colored part represents the hydrophobic chains of the surfactant.	4
1.3	Schematic diagram of surfactant molecules at the air-water interface as well as inside water (blue color) (a) at concentration below CMC : surfactant monolayer formation at air-water interface and monomers in bulk water. The hydrophilic heads prefer water while the hydrophobic tails try to avoid water and (b) at concentrations above CMC: micelles (spherical aggregates) with hydrophilic heads towards water and hydrophobic tails inside the micelle are formed.	5
1.4	Schematic diagram of a reverse micelle which is a spherical aggregate of several surfactants. Hydrophilic heads are towards water while hydrophobic tails try to minimise the contact with water by being in oil.	7

LIST OF FIGURES

1.5	Sketches of different self-assembled structures of surfactant in water. (a) Spherical micelle with hydrophobic core and hydrophilic surface. The radius of the core is approximately equal to the length of the hydrophobic chain (l_{max}). (b) In reverse/inverted micelles the hydrocarbon tails are organised towards the oil medium, while the head groups are inside the micelle. Inverted structures can be cylinders or vesicles too. (c) Cylindrical micelles with a cross-section similar to spherical micelles. They are usually polydisperse due to the incorporation of more surfactants, causing the cylinder grow. (d) Bicontinuous cubic structure with interconnected monolayer channels separating both oil and water continuous medium. (e) In lamellar structure or planar bilayer, the bilayer thickness is nearly 1.6 times l_{max} [1]. The plane layers separates the continuous oil and water medium without any channels in the surfactant monolayer and (f) Vesicles are formed by several closed bilayers, without any connection between adjacent bilayers. The aqueous compartment is isolated from the oil compartment.	9
1.6	A small section of a spherical micelle. Packing conformation of surfactant molecules depend on a_{op} , chain volume (v) and chain length (l_c). Equilibrium forces in water between repulsive headgroups and attractive tails defines the optimum headgroup area a_{op}	10
1.7	Packing parameters, parameter shape and the various self assembled structures formed by surfactant in water. Hydrophilic part is exposed to water and the hydrophobic part is shielded away from water.	11
1.8	Schematic phase diagram of binary water-nonionic surfactant (C_iE_j) system as a function of temperature.	12
1.9	Definition of the principal curvature radii for a sponge-like structure formed by a surfactant monolayer. A sponge has saddle-like elements, that can be characterized by the two principal curvature radii, c_1 and c_2	13

LIST OF FIGURES

1.10 Morphologies determined by different curvatures of surfactant layer, spherical, cylindrical and lamellar structures.	14
1.11 Curved interface formed by hydrophilic heads and hydrophobic chains of surfactant molecules of a swollen inverted micelle with oil (yellow) in water (blue).	15
1.12 Schematic diagram of changing size of the polar region of a non-ionic surfactant molecule with changing hydration. Blue color represents hydrated water molecules.	16
1.13 normal curvature of the surfactant monolayer (less water molecules to hydrate) and spontaneous curvature of the surfactant monolayer(no constraint of water molecules). Blue and yellow color represents water and oil respectively.	17
1.14 'Unfolded' phase prism of water-oil-nonionic surfactant system showing the three binary phase diagrams. Shaded portions in figure show the miscibility gaps.	19
1.15 Schematic phase prism for a water-oil-nonionic surfactant system with broken critical lines. Macro-state of the microemulsion sample is sketched in the left side. For a description see the text. Figure adapted from [2]	20
1.16 Schematic phase prism of water-oil-nonionic surfactant mixture. The shaded region shows a vertical section with fixed water to oil ratio. microemulsion	21
1.17 Schematic 'fish cut' phase diagram of a non-ionic microemulsion with equal water to oil proportion as a function of surfactant concentration. The 'body' of the fish has a surfactant-rich phase coexisting with a water and a oil-rich phase, from a temperature region T_l to T_u (marked with dashed line). The 'tail' of the fish has a single phase region starting from $\bar{\phi}_s$ towards higher ϕ_s . On the either side of the body of the fish, a microemulsion phase coexist with a water-rich or oil-rich phase.	22
1.18 Comparison of the phase diagrams of microemulsions with a weak (C_4E_1) and a strong ($C_{12}E_5$) surfactant.	24

LIST OF FIGURES

1.19	Oil (shaded) and water (unshaded) domains generated by the Voronoi process. Heavy lines denote the surfactant monolayer	25
1.20	Array of cubical cells randomly filled with water (shaded) and oil (white). Surfactants reside on the dark lines separating oil and water domains.	26
1.21	A small portion from the fish cut phase diagram to show the droplet size in the 1Φ and 2Φ region. Red squares show the water emulsification boundary, WEB. Blue circles are the schematic representation of water droplets. At temperatures $T < T_{web}$, droplet size is independent of temperature while at $T > T_{web}$ the size of droplets are temperature dependent. Along the dashed line droplet size is the same.	31
1.22	Change of droplet radius with increasing temperature. The schematic diagram shows how the radius changes with temperature, ranging from one phase ($T < T_{web}$) to two phase ($T > T_{web}$), when crossing the water emulsification boundary(T_{web}).	32
1.23	Sketch of a microemulsion with water droplets (blue circles) in an oil matrix (yellow color) under constant heating. This schematic diagram shows an idealised version of the phase separation process covering a temperature window of $T \approx T_{WEB} \pm 1K$. 1Φ microemulsion consists of N droplets of radius $R^{1\Phi}$. This radius equalises the optimum radius at the emulsification boundary. At WEB, one big drop of radius R^{big} forms and the size of other droplets($R^{2\Phi}$) decrease. In 2Φ this big drop sedimented at the bottom.	36
2.1	Sketch of the top view of the experimental setup: water bath, Haake temperature controller, a CCD camera, a cold light source, a mirror, a magnetic stirrer and a digital thermometer. Microemulsion samples are observed in reflected light.	41

2.2	Microemulsion samples in 2cm wide viols are observed in reflected light. Left: 1Φ microemulsion appears dark due to the complete transmission of light without any scattering. Center: A 2Φ microemulsion looks turbid due to scattered light by the comparatively big droplets formed during phase separation. Right: In a 3Φ microemulsion, a thin surfactant rich area coexists with an upper oil-rich and a lower water-rich area.	42
2.3	Schematic diagram of the adiabatic chamber of VP-DSC. Sample and the reference solution are filled in two lollipop shaped cells shown in blue color. ΔT shows the relative temperature differences.	44
2.4	A DSC curve for water-decane- C_8E_3 microemulsion of equal volume fraction of water and oil and surfactant volume fraction, $\phi_s = 0.31$. There are two jumps of the signal: a step at lower temperature T_2 due to the oil emulsification failure across T_{OEB} (1Φ to underline- 2Φ) and the phase transition from 1Φ to 2Φ -overline is identified with a step at higher temperature T_1 in the signal (across T_{WEB}). The area under the step is shaded. Dashed line shows the baseline in one-phase region.	45
2.5	Hydrodynamic radius (R_H) of a water swollen micelle (blue color) in an oil matrix (yellow color). Hydrodynamic diameter is shown as a dashed circle.	47
2.6	Left: The exponentially decaying autocorrelation function (green line). Right: Decay rate versus scattering vector at different scattering angles (black triangle) with a linear fit (red line).	48
2.7	The sketch of the definition of the scattering vector $\vec{q} = \vec{k} - \vec{k}_0$. The scattering vector \vec{q} is determined by the scattering angle θ and the wavelength λ of the laser light	49
2.8	DLS setup	50
2.9	Kink formation due to micelle formation showed by the surface tension against concentration curve obtained from a tensiometer experiment.	52

LIST OF FIGURES

2.10 (a) Schematic diagram of du Noüy ring. The ring registers the contact with the liquid surface and is pushed through the liquid surface to a few millimeters down. Then it is pulled up until the maximum Force is reached. (b) Schematic diagram of a Wilhelmy plate during surface tension measurement. The plate is wetted by a length l and makes an angle θ with the liquid surface. A force F acts due to the contact with liquid.	53
3.1 Experimental value of the T_{WEB} for 1:1 water: oil microemulsion, under cooling and heating in a water bath.	56
3.2 Microemulsion fish-cut phase diagram with 1:1 water-decane. Water emulsification boundary, WEB [blue squares] and oil emulsification boundary, OEB [green squares] are shown for samples with varying surfactant concentration and with increasing temperature.	57
3.3 Microemulsion phase diagram with 3:7 (black squares) and 7:3 (green triangles) water-decane. T_{WEB} [solid symbols] and T_{OEB} [open symbols] are shown for microemulsion samples with increasing surfactant concentration.	58
3.4 Temperature of the water emulsification (T_{WEB}) (solid circles) and oil emulsification (T_{OEB}) (open circles) boundaries for water-decane- C_8E_3 microemulsion with $\phi_s = 35\%$ (green) and varying oil to water + oil ratio; T_{WEB} and T_{OEB} for the same ingredient sample with $\phi_s = 40\%$ (blue) and varying α_o ; T_{WEB} and T_{OEB} at varying α_o for microemulsion samples with $\phi_s = 50\%$ (orange).	59

- 3.5 (a) The schematic fish cut phase diagram with the temperature line (red color arrows) along which calorimetry is done. Red arrows show the direction and the temperature intervals investigated by calorimetry. A sketch of 1Φ microemulsions (water droplets in oil or oil droplets in water) to the *overline* – 2Φ or *underline* – 2Φ microemulsion (microemulsion with water or oil droplets coexisting with expelled water or oil) is shown. (b) A step in the specific heat signal (solid squares) when passing T_{WEB} during an upscanning from 1Φ region to the *overline* – 2Φ region (right). Data taken at a scan speed of 2 K/h (pink) and 5 K/h (yellow) are shown. The average height of the step is given by the arrows. Solid lines denote the baseline in the 1Φ region and the dashed lines shows the baseline in the 2Φ region. While downscanning, the specific heat shows a step when passing the oil emulsification boundary (left Fig. with open squares). The data plot at 2K/h is shifted along the y-axis in both figures for better eye guidance. 61
- 3.6 Analysed DSC data for microemulsions with 1:1 water : oil and 31% of surfactant volume fraction. ΔC_v^{step} while crossing WEB and OEB, at two different scan rates, hardly depend on scan rate within experimental accuracy. T_{WEB} and T_{OEB} are also recorded. 62
- 3.7 DSC data for microemulsion sample with 1:1 water:oil and 35% of surfactant volume fraction. Experiments are done at 1.4 K/h. ΔC_v^{step} while crossing WEB is obtained with an accuracy of 0.01 cal/ $^{\circ}$ C. The T_{WEB} showed a reproducibility with an accuracy of 0.1 $^{\circ}$ C. The mean height of the step is shown by dotted and dashed lines. 63
- 3.8 Dependence of ΔC_v^{step} on phase transition temperature T_{WEB} for 1:1 water-decane microemulsion samples with varying surfactant concentrations. Solid symbols shows the full height of ΔC_v^{step} while open symbol shows the mean height of ΔC_v^{step} . Different colors correspond to different surfactant concentrations (ϕ_s). The various symbols for one T_{WEB} are the data taken at various scan rate ranging between 2 K/h to 15 K/h. 64

LIST OF FIGURES

3.9	Dependence of ΔC_v^{step} on phase transition temperature T_{WEB} for sample with 3:7 water-to-oil ratio and varying surfactant concentration. Different data points for the same T_{WEB} denote the scattering of the data at varying scan rates between 2K/h to 15 K/h. Solid symbols show the full height of ΔC_v^{step} while open symbol shows the mean height of ΔC_v^{step}	64
3.10	Dependence of ΔC_v^{step} on phase transition temperature T_{WEB} for sample with 7:3 water-decane ratio and varying surfactant concentration ranging between 35% and 55% (different colored diamonds). Solid symbols show the full height of the step in the specific heat ΔC_v^{step} , while open symbols show the mean height of the step. The data at different scan rates on the same sample are shown by the same colored symbols.	65
3.11	Mean height of the specific heat-step with increasing temperature for water emulsification boundaries. The data correspond to three different compositions : 7:3 water-decane (purple diamond), 1:1 water-decane (wine pentagons) and 3:7 water-decane microemulsion (orange circles). A third order polynomial fit is given for a better eye guidance.	65
3.12	Difference in the phase transition temperature obtained from visual inspection (scattering) in water bath and microcalorimetry (DSC) for microemulsion sample with equal water to oil ratio. The scan rate is added in brackets.	66
3.13	Refractive index of the microemulsion samples with different surfactant concentrations at different temperatures.	67
3.14	Fish cut phase diagram of a 1:1 water-decane microemulsion as a function of ϕ_s . T_{WEB} and T_{OEB} are shown by the blue and black circles respectively. The temperatures at which samples are investigated by DLS are marked by pink crosses. The macroscopic appearance of the microemulsion is sketched too.	68
3.15	Hydrodynamic radius of oil/water domains obtained from DLS. Microemulsion samples with 1:1 water-decane and three different surfactant concentrations are used.	69

LIST OF FIGURES

3.16	Calculated and the experimental data (DLS) of the domain sizes of 1:1 water-decane microemulsion sample with varying surfactant concentration at 24 ⁰ C. Results are presented in nanometers. . . .	69
3.17	The concentration dependence of the surface tension of a C ₈ E ₃ solution at 20.4 ⁰ C obtained using a Wilhelmy plate. The complete data set is shown in the inset.	70
3.18	Measurement of dependence of the surface tension on surfactant concentration using a Wilhelmy plate (solid squares) and a ring geometry (open circles). The surfactant solutions with an initial concentrations of 4 times CMC was dispensed to pure water. . . .	71
3.19	Concentration dependence of the surface tension of a C ₈ E ₃ solution at 20.5 ⁰ C measured using a Wilhelmy plate. A solution of 5 times CMC (green up triangles) and 4 times CMC (purple right triangles) are dispensed to pure water, respectively.	72
3.20	Appearance of 3Φ region (red dotted line) according to the CMC of C ₈ E ₃ in water. The experimental data for the emulsification boundaries [T _{WEB} [green squares] and T _{OEB} [blue squares]] for 1:1 water to oil ratio microemulsion with varying surfactant concentration.	73
3.21	Tensiometric data of the concentration dependent surface tension of C ₈ E ₃ in decane.	74
3.22	Variation of the critical micelle concentration (CMC) of C ₈ E ₃ in water with increase in temperature. A linear decline upto 50 ⁰ C is observed.	74
3.23	Table showing the actual volume fraction of the surfactant in the sample and the interfacial active surfactant obtained using the equation 3.3	76
3.24	The least square fitting (red line) of the emulsification boundary data for 1:1 water to oil ratio microemulsion, according to the modified equation. Water emulsification boundary, T _{WEB} [solid blue circles] and oil emulsification boundary, T _{OEB} [solid black circles] are shown for the microemulsion samples with varying surfactant concentration.	77

LIST OF FIGURES

3.25 Values for the parameters from the fitting of the emulsification boundary data for 1:1, 3:7 and 7:3 water to oil ratio microemulsion according to the modified Helfrich equation. Fitting of T_{WEB} yielded R_w^{mic} , T_l and a_w . The effective length of the surfactant is kept fixed, $l_s = 1\text{nm}$. Fitting of the oil emulsification boundary, T_{OEB} gave R_o^{mic} , T_u and a_o	78
3.26 Fits of the emulsification boundaries for microemulsion with a 3:7 water to oil ratio according to the modified equation. Water emulsification boundary, T_{WEB} [solid blue circles] and oil emulsification boundary, T_{OEB} [solid black circles] are shown for the microemulsion samples with varying surfactant concentration. The red lines show the fits.	79
3.27 Fitting of the emulsification boundary data for 7:3 water to oil ratio microemulsion according to the modified equation. Water emulsification boundary, T_{WEB} [solid blue circles] and oil emulsification boundary, T_{OEB} [solid black circles] are shown for the microemulsion samples with varying surfactant concentration. The red line shows the fitting	80
3.28 Experimental data for the water emulsification boundary, T_{WEB} [solid blue circles] and oil emulsification boundary T_{OEB} [solid black circles] of 3:7 water to oil ratio microemulsion. Predicted emulsification boundaries with the modified equations is given as green lines.	82
3.29 Plotting of the emulsification boundary for 7:3 water to oil ratio microemulsion according to the prediction with the modified equation (green line). Experimental data for the water emulsification boundary, T_{WEB} [solid blue circles] are shown for the microemulsion samples with varying surfactant concentration.	83

<p>3.30 Experimental data for the evolution of water and oil emulsification boundaries with temperature and varying α_o are given by solid and open circles respectively. Surfactant concentration is fixed at 35% (green), 40% (blue) and 50% (orange). The predictions (lines) for the water emulsification boundaries (solid lines) and the oil emulsification boundaries (dotted lines) according to the modified equation for the three different surfactant concentrations are shown. The dashed line shows the temperature T_l and T_u. Microstructure of the sample at various temperatures are sketched.</p>	84
<p>3.31 Spontaneous curvature as a function of temperature for a microemulsion with equal proportion of water to oil. At higher and lower temperatures the water and oil droplet reaches inverse micellar radii R_{mic}^w and micellar radii R_{mic}^o respectively. $'a'_w$ and $'a'_o$ gives the scaling of the surfactant morphology from a droplet structure to inverse micelle and micelle.</p>	86
<p>3.32 Sketch of the coexisting spontaneous curvature as a function of temperature for a microemulsion with equal proportion of water and oil. At higher and lower temperatures the water and oil droplet reaches inverse micellar radii R_{mic}^w and micellar radii R_{mic}^o respectively. $'a'_w$ and $'a'_o$ gives the scaling of the surfactant morphology from a droplet structure to inverse micelle/micelle.</p>	87
<p>3.33 Temperature dependent variation of the specific heat for equal water to oil ratio and surfactant concentration $\phi_s = 0.31$ (orange diamonds), $\phi_s = 0.45$ (purple diamonds) and $\phi_s = 0.55$ (dark cyan diamonds). Data has been subtracted with a baseline. Mean height of the specific heat and the prediction (with the pre-factor) are shown. The thermograms are taken at 5 K/h across water emulsification boundary.</p>	90

LIST OF FIGURES

3.34	Experimental data from DSC (open circles) and the prediction to the height of the specific heat-step according to Eq.3.12 (dashed line) and Eq.3.13 with prefactor (solid line) with increasing phase transition temperature for (a) 1:1 water to oil ratio microemulsion; (b) 3:7 water to oil ratio microemulsion and (c) 7:3 water to oil ratio microemulsion.	92
3.35	Experimental data (open circles) for the the mean height of the specific heat-step for with increasing T_{WEB} for (a) 1:1 water to oil ratio microemulsion (purple) ; (b)3:7 water to oil ratio microemulsion (black) and (c) 7:3 water to oil ratio microemulsion (blue). Theoretical prediction of the height of the specific heat-step with prefactor are shown by solid lines (magenta) for the three different data.	94
3.36	The mean height of the specific heat-step of microemulsion samples with three different $\alpha_o = \alpha_o/(\alpha_o + \alpha_w)$ and fixed surfactant volume fraction 0.35: from the differential scanning calorimetry (open circles) and according to the prediction Eq.3.13(cross).	95
3.37	Experimental data for the T_{WEB} (blue circles) and T_{OEB} (black circles) for the C_4E_1 - octane - water microemulsion. A 10% surfactant-volume fraction the sample is in 2Φ . Dotted line separates 2Φ and 3Φ . Green line shows the prediction.	96

Chapter 1

Introduction

Phase studies are inevitable for the basic understanding of general phase behaviour and kinetics of the structural changes of a system. This is not only of fundamental interest but also is very important for any industrial and technological processes. Phase diagrams for microemulsions are quite complex since there are at least three components- water, oil and surfactant. These structured fluids have a readily deformable surfactant interface, which bend either towards water or oil or both. A wide range surfactants can produce microemulsion. I will introduce non-ionic microemulsion that has served as model system for this work. Properties of non-ionic surfactants are sensitive to the changes in the temperature. Non-ionic microemulsion goes through a multitude of micro and macro structures in less than $20^{\circ}C$. The generic phase behaviours, dominated by the surfactant properties, for microemulsion are evaluated.

1.1 Motivation and Objectives

It was the goal of this work to investigate the phase behaviour of non-ionic microemulsions and predict the phase transition boundaries including the three-phase region using a modified Helfrich free energy. The phase behaviour is approached in two ways : (a) composition dependent and (b) through the bending free energy. The consistency of the phase transition boundaries in these two different approaches are checked. Experiments and predictions are examined for phase

boundaries of microemulsions according to the strength of the surfactant too. The spontaneous curvature of the surfactant monolayer at various temperatures and its influence on the phase behaviour are investigated. By careful experiments and theoretical interpretations, the origin of the phase behaviour is probed.

The thesis is organised as follows: at the beginning, the fundamentals of microemulsions starting from a molecular picture of surfactant assemblies along with the theories and models are reviewed in Chapter 1. A detailed description of the characterisation of the phase behaviour (temperature and composition-dependent) of water-oil-nonionic microemulsion are given in Chapter 2. As main experimental methods I used video microscopy, differential scanning calorimetry, tensiometry and dynamic light scattering. In Chapter 3, the data are analysed with the modified Helfrich bending free energy functions preceded with the discussions on the coexisting of the spontaneous curvature of the surfactant monolayer. Finally, the results allow for the generic predictions to the phase transition boundaries including three phase region. Chapter 4 summaries my work.

1.2 Surfactants and Classification

Surfactants are organic molecules having a characteristic molecular structure making them "surface active agent". They are amphiphilic molecules, with a hydrophilic (the head) and a hydrophobic group (the tail) with molecular weight ranging from a few hundred to thousand [3]. The hydrophilic part is usually a

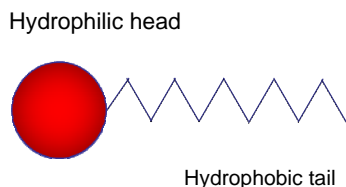


Figure 1.1: Schematic diagram of a surfactant molecule. Here the red circle represents the hydrophilic head while the blue chain represents the hydrophobic tail.

non-ionic (polar) or an ionic group attached covalently to the hydrophobic part which is usually a long hydrocarbon chain. The hydrophilic region associates with the hydrogen bond network of water [4], whereas the hydrophobic region in general includes hydrocarbon chain which do not favors contact with water. Water molecules are more ordered around a hydrophobic group than in bulk water. Therefore it is entropically unfavorable to restructure or reorient the water molecules near to a nonpolar molecule, giving it a hydrophobic nature. Briefly, a single surfactant molecule has both a water soluble and a water insoluble part. A surfactant molecule, in general is picturised with a head and tail as shown in FIG 1.

Depending on the nature of the hydrophilic group, surfactants are further classified [3, 5, 6] as

1. Anionic: The surface active part bears negative charge. The relatively low cost in manufacture makes them the most sort after surfactant in the industry. Sodium dodecylsulfate (SDS) is a well known example with the molecular formula $\text{CH}_3(\text{CH}_2)_{11}\text{SO}_4^- \text{Na}^+$. In here the dodecane is insoluble in water (hydrophobic tail), whereas the ionisable property makes the sulphate portion strongly hydrophilic [see FIG. 1.2]. Other examples are $\text{RCOO}^- \text{Na}^+$ (soap) and $\text{RSO}_3^- \text{Na}^+$ (sulfonates).

2. Cationic: The surface active part bears positive charge. They are non-biodegradable and are used as bactericides. Due to the tendency to be adsorbed at negatively charged surfaces, they are anticorrosive and antistatic agents [see FIG. 1.2]. Examples: $\text{RNH}_3^+ \text{Cl}^-$ (salt of long-chain amine), $\text{RN}(\text{CH}_3)_3^+ \text{Cl}^-$ (quaternary ammonium chloride), CTAB.

3. Zwitterionic: These surfactants contain both cationic and anionic groups. In general their properties highly depend on the pH of the solution [see FIG. 1.2]. Example: $\text{RH}^+ \text{H}_2\text{CH}_2\text{COO}^-$ (long-chain amino acid), $\text{RN}^+(\text{CH}_3)_2\text{CH}_2\text{CH}_2\text{SO}_3^-$ (sulfobetaine).

4. Non-ionic: Apparently bears no ionic charge but are polar. Two important classes of non-ionic surfactants are the ones based on ethylene oxide, referred to

as ethoxylated surfactants and the multihydroxy products such as glycerols and sucrose esters. The former category has a general form $\text{H}(\text{CH}_2)_i(\text{OCH}_2\text{CH}_2)_j\text{OH}$ (abbreviated as C_iE_j). Octyl triethylene glycol ether (C_8E_3) is an example of an ethoxylated surfactant [see FIG. 1.2]. The carbon chains form the hydrophobic tail while the ethylene oxide (EO) chains form the hydrophilic head. The solubility of ethylene oxide chains highly depend on temperature. At a low temperature, water is a good solvent for ethylene oxide chains due to hydrogen bond formation. Increasing temperature causes high entropy leading to the breakage of these hydrogen bonds. This makes water a poor solvent for the same surfactant at higher temperatures.

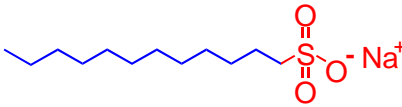
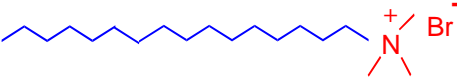
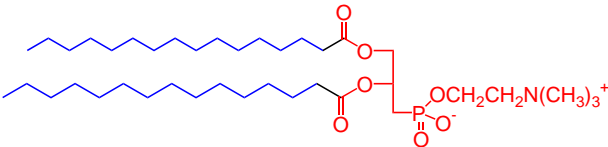
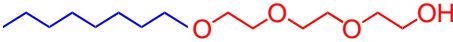
Anionic	 <p>Sodium dodecylsulfate (SDS)</p>
Cationic	 <p>cetyltrimethylammonium bromide (CTAB)</p>
Zwitterionic	 <p>Dipalmitoylphosphatidylcholine (lecithin)</p>
Nonionic	 <p>Octyl triethylene glycol ether (C_8E_3)</p>

Figure 1.2: Surfactant classification according to the nature of the hydrophilic group and examples. The red colored part represents the hydrophilic head and the blue colored part represents the hydrophobic chains of the surfactant.

1.3 Surfactants in water

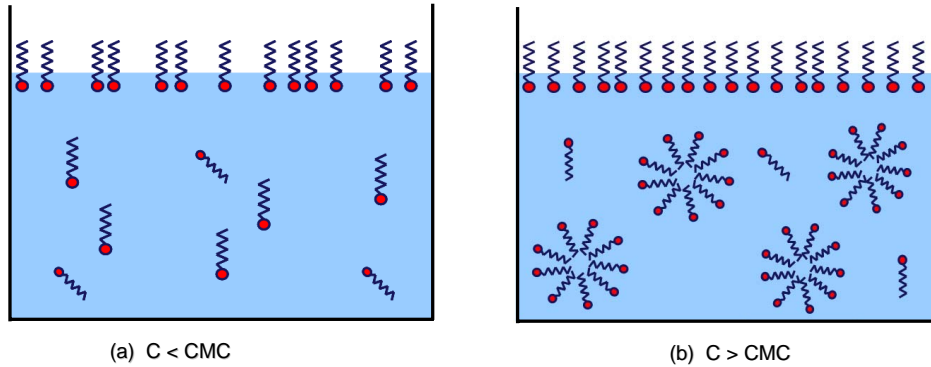


Figure 1.3: Schematic diagram of surfactant molecules at the air-water interface as well as inside water (blue color) (a) at concentration below CMC : surfactant monolayer formation at air-water interface and monomers in bulk water. The hydrophilic heads prefer water while the hydrophobic tails try to avoid water and (b) at concentrations above CMC: micelles (spherical aggregates) with hydrophilic heads towards water and hydrophobic tails inside the micelle are formed.

Surfactants show distinct behavior while interacting with different solvents due to the quite different solubility criterion within a molecule. To-date most investigations are focused on aqueous surfactant solutions [7], while a few research are done on surfactants in non-aqueous media [8, 9]. At low concentration surfactant molecules exist as monomers in water. The hydrophilic groups strongly interact with water while the hydrophobic alkyl chains try to avoid contact with water. As the hydrophobic groups distort the arrangement of water molecules, they increase the free energy of the system. Hydrophobic groups have to be avoided to reduce this free energy. Surfactants achieve this state by self assembling in different ways [FIG. 1.3, FIG. 1.5]. Along the water surface they spontaneously form a monolayer with hydrophilic part inside water and hydrophobic part towards air [FIG. 1.3]. This could significantly alter the surface properties of water and thereby cause a reduction in surface tension and thus decreasing the free energy. Increasing the surfactant concentration saturates the water surface. And any further increase in the concentration causes the molecules to dissolve in water and thereby changes the way of arrangement of surfactant molecules. To

reduce water-tail contact, the system starts self-assembling. Surfactant molecules aggregate in spherical forms with hydrophobic tails within the spheres and hydrophilic part towards water. These aggregates are called micelles [FIG. 1.3 (b)]. Typical micelle contains 50 to 100 monomers depending on the type of surfactant. The critical concentration above which spontaneous formation of micelles occurs is called critical micelle concentration (CMC). Further increase in surfactant concentration above CMC increases the number of micelles which are in dynamic equilibrium with the monomers in the solution and the saturated water-air interface. FIG. 1.3 shows the state of surfactant in water below and above the critical micelle concentration. CMC is an important measure for surfactant characterization.

1.4 Surfactants in non-polar solvent (oil)

The behavior of surfactants in nonpolar media is equally relevant in understanding the characteristics of ternary mixtures, as well as for the applications in oil recovery and the synthesis of colloidal particles [10, 11]. However, the information of the physical properties of non-ionic surfactants in non-polar media is scarce. The obvious difference between micelles in polar and non-polar media is the structural reversion, with polar core covered by hydrophobic tails known as reverse or inverted micelle [see FIG. 1.4]. As mentioned before, the CMC in aqueous media can be explained by the additional ordering of the water molecules upon addition of surfactant. In contrast to this, in non-polar media the presence of surfactants hardly induces structural changes to the solvent molecules [12]. The interaction of the hydrophobic tails with solvent is also favourable with the other hydrophobic tails. Hence surfactants do not migrate to the solvent-air interface. Furthermore, air is highly hydrophobic. Therefore the head groups try to avoid air as well as the solvent. The dipole-dipole interactions between the polar head groups lead to the formation of small aggregates. Unlike the large micellar aggregate in water, aggregation number in non-polar solvents is moderate, ranging from 7 to 30 [7, 13]. Moreover, the average life time of a molecule at the interface is lower due to a high exchange rate between molecules molecularly dissolved and in aggregates. The average aggregation number at 25°C for (a)AOT in dodecane is around 28,

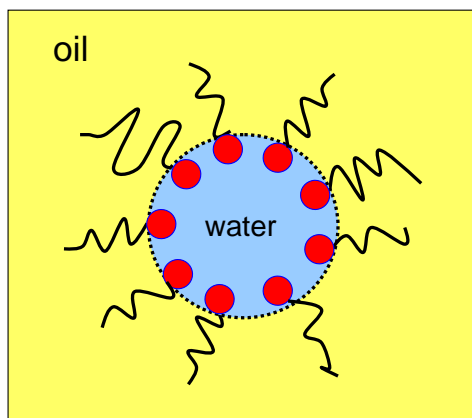


Figure 1.4: Schematic diagram of a reverse micelle which is a spherical aggregate of several surfactants. Hydrophilic heads are towards water while hydrophobic tails try to minimise the contact with water by being in oil.

determined by ultracentrifugation [7]. In CCl_4 the average aggregation number is determined as 17 by vapour pressure osmometry [7]; (b) critical micellar concentration of non ionic surfactant C_{12}E_j ($j = 3,4,5$) is determined by small angle neutron scattering measurements. The average aggregation numbers remain very low of about 10 [14]. AOT is soluble in both polar and apolar solvents. This may be a reason for the high aggregation number of AOT in oil when compared with other surfactants. Close to the CMC there is no significant change in the aggregation number of surfactant in non-polar solvent. This causes an absence of a sharp change in the physical properties of the solution in non-polar media. This leads to the uncertainty in the precise measurement of CMC of non-ionic surfactants.

1.5 Different morphologies of surfactant aggregates

Increase in surfactant concentration steadily increase the number of micelles which are in dynamic equilibrium with the monomers in the solution. Changes in the surfactant concentration changes the morphology of the surfactant aggregate. Aggregation in different shapes like spherical micelles, cylindrical micelles,

lamellar structure, hexagonal, bicontinuous structure etc. have been observed. A few morphologies are sketched in FIG. 1.5 [1].

Israelachvili et al. tried to predict these shapes in terms of geometrical shape of the individual surfactant molecules. Therefore, Israelachvili introduced a dimensionless parameter called '*packing parameter*', P . It can be defined as

$$P = \frac{v}{a_{op}l_c} \quad (1.1)$$

where a_{op} is the optimal head group area of the surfactant, v the hydrocarbon chain volume and l_c the chain length [FIG. 1.6].

In water, the surfactant layer experience opposing forces at the water-hydrocarbon tail interface [FIG. 1.6]. Hydrophobic attractive force try to decrease the interfacial area whereas repulsive force try to increase the area ' a ' per molecule. This result in an optimal interfacial area ' a_{op} ' [3, 4]. Though often hard to quantify, the '*packing parameter*' P is useful to estimate the shape of surfactant aggregates. Structures taken by surfactant molecules with different packing parameters are shown in FIG. 1.7 and FIG. 1.5. Surfactants with charged headgroups get a large head group area a_{op} and thus $P < 1/3$ and they tend to form spherical micelles. Those surfactants with smaller headgroup area such that $1/3 < v/a_{op} l_c < 1/2$ cannot pack into spherical micelle but forms cylindrical (rod-like) micelles. Another category of surfactants possess bulky hydrocarbon chains and small head groups but maintain the surface area at its optimal value. Their $v/a_{op} l_c$ value lie close to 1 and they form bilayers. Finally for surfactants with very small head group areas and bulky hydrocarbon chains, the packing parameter value exceeds unity and they form inverted micelles.

There are various factors affecting the geometric packing parameter, P . Since we are focusing on non-ionic surfactants, the effect of temperature is the relevant factor here. Changing the temperature can alter both a_{op} and l_c . Also in non-ionic surfactant by changing the length of the polyethyleneoxide chains, a_{op} is changed. Then the monolayer structure and thereby the phase behavior varies too. FIG. 1.8 [15] shows a general phase diagram for non-ionic surfactant in water as a function of temperature. The surfactant molecules are dissolved in water until the surfactant concentration reaches its CMC. Just above CMC, a micellar solution

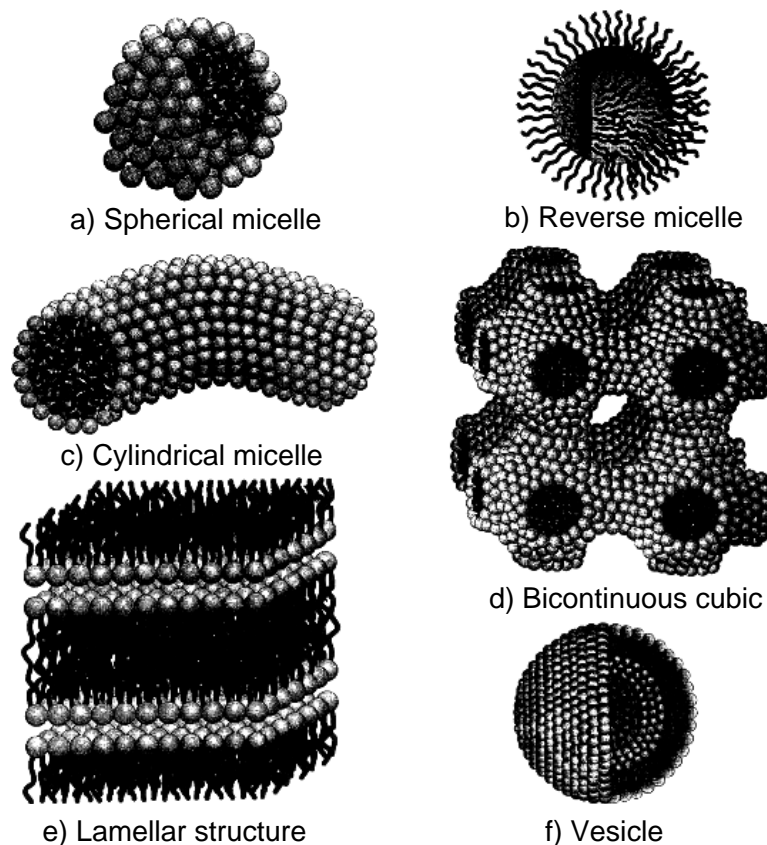


Figure 1.5: Sketches of different self-assembled structures of surfactant in water. (a) Spherical micelle with hydrophobic core and hydrophilic surface. The radius of the core is approximately equal to the length of the hydrophobic chain (l_{max}). (b) In reverse/inverted micelles the hydrocarbon tails are organised towards the oil medium, while the head groups are inside the micelle. Inverted structures can be cylinders or vesicles too. (c) Cylindrical micelles with a cross-section similar to spherical micelles. They are usually polydisperse due to the incorporation of more surfactants, causing the cylinder grow. (d) Bicontinuous cubic structure with interconnected monolayer channels separating both oil and water continuous medium. (e) In lamellar structure or planar bilayer, the bilayer thickness is nearly 1.6 times l_{max} [1]. The plane layers separates the continuous oil and water medium without any channels in the surfactant monolayer and (f) Vesicles are formed by several closed bilayers, without any connection between adjacent bilayers. The aqueous compartment is isolated from the oil compartment.

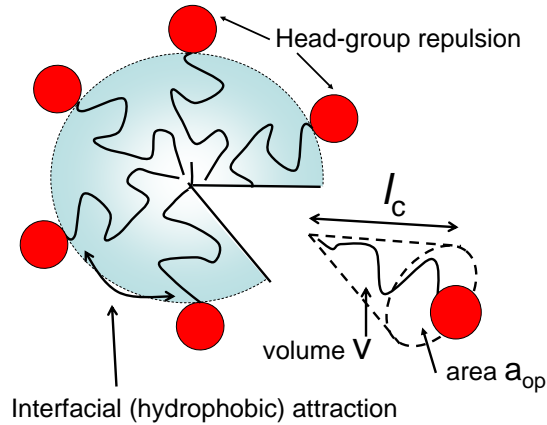


Figure 1.6: A small section of a spherical micelle. Packing conformation of surfactant molecules depend on a_{op} , chain volume (v) and chain length (l_c). Equilibrium forces in water between repulsive headgroups and attractive tails defines the optimum headgroup area a_{op}

is observed. At higher concentrations most surfactants form liquid crystalline mesophases. They start to pack together in geometric arrangements depending upon the preferred volume of the head and the tail of the surfactant molecule. Then they have an ordered molecular arrangement like solid crystals. Further increase in concentration leads to the arrangement of micelles in a cylindrical way and these long cylindrical micelles can arrange on a two-dimensional hexagonal lattice to form a hexagonal phase. Here each cylindrical micelle is surrounded by six other cylindrical micelles. With increasing surfactant concentration, the cylindrical micelles becomes branched and interconnected to form a bicontinuous cubic structure [16]. A lamellar phase consisting of stacks of bilayers could be formed at even higher concentrations. In this phase, bilayers of surfactant layers alternate with the water layers. Further increase of concentration can lead to a hexagonal phase made of inverted cylindrical micelles. Hexagonal and lamellar phase are anisotropic and can be detected by the radiance under polarizing sheets.

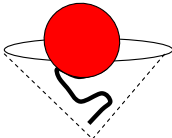

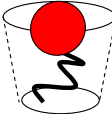
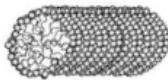
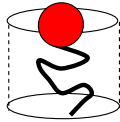
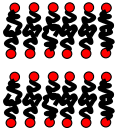
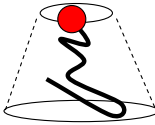
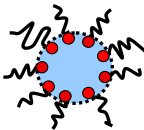
Surfactant	$P = v / (a_0 l_c)$	Shape	Aggregate formed
Large head group area	$< 1/3$	Cone 	Spherical micelle 
Small head group area	$1/3 - 1/2$	Truncated cone 	Cylindrical micelle 
Double chain surfactants with small head group area	~ 1	Cylinder 	bilayers 
Double-chain surfactants with very small head group area or with long HC chain	> 1	Inverted truncated cone 	Inverted micelle 

Figure 1.7: Packing parameters, parameter shape and the various self assembled structures formed by surfactant in water. Hydrophilic part is exposed to water and the hydrophobic part is shielded away from water.

1.6 Helfrich free energy

Surfactants monolayers or bilayers are a physical realization of fluctuating surfaces. These monolayers are soft, flexible and incompressible. This is due to the van der Waals forces, hydrophobic, hydrogen-bonding and screened electrostatic interactions. These monolayers are very thin sheets with a height of 3-10 nm depending on the effective length of surfactant. In the aqueous solution they self-assemble in a variety of different morphologies. For example, in a small section of bicontinuous structure, the continuous phase is interwoven by surfactant bilayers. Due to the amphiphilicity at the interface, surfactant layers gets a bimetallic

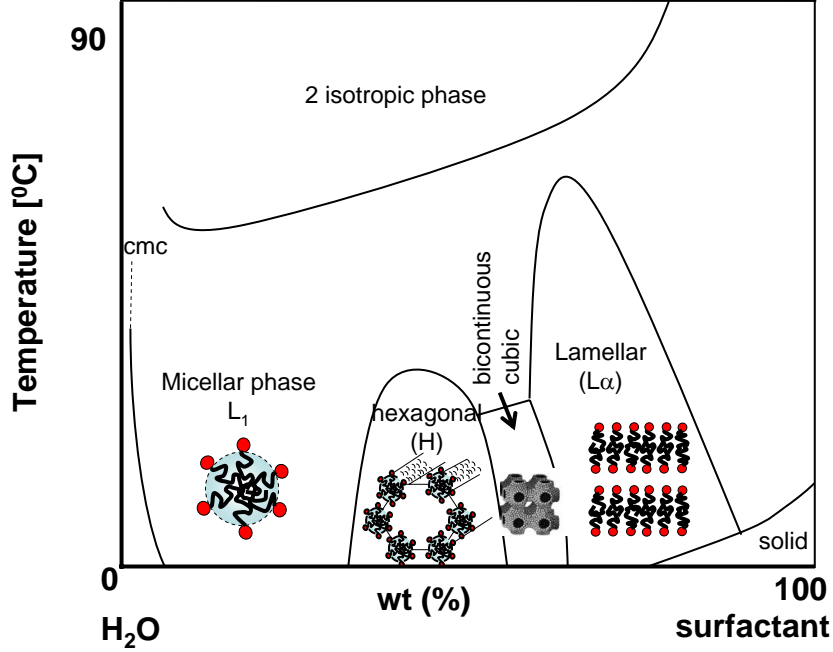


Figure 1.8: Schematic phase diagram of binary water-nonionic surfactant (C_iE_j) system as a function of temperature.

strip effect. This causes the hydrophilic-hydrophobic interface to be curved. The curvature of the surface is defined by the principal radii of curvatures R_1 and R_2 [FIG. 1.9]. The principal curvatures describe the maximum bending of the surface in perpendicular direction at an infinitesimal small area of the surface.

Three simple and common morphologies are discussed below.

a) When both principal curvatures are the same, the surface has spherical morphology [FIG. 1.10].

$$c = c_1 + c_2 = \frac{1}{R_1} + \frac{1}{R_2} = \frac{2}{R}. \quad (1.2)$$

b) If one of the principal curvature is equal to zero, the total curvature is given by $1/R$ which holds for cylindrical morphology [FIG. 1.10].

$$c = c_1 + c_2 = \frac{1}{R_1} + 0 = \frac{1}{R}. \quad (1.3)$$

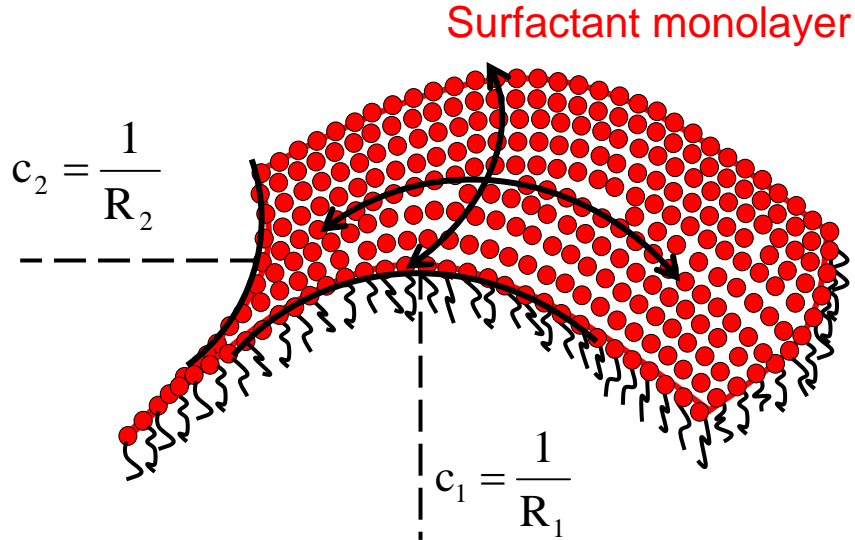


Figure 1.9: Definition of the principal curvature radii for a sponge-like structure formed by a surfactant monolayer. A sponge has saddle-like elements, that can be characterized by the two principal curvature radii, c_1 and c_2 .

c) If both principal curvatures are zero then the monolayer is flat, i.e. for example in case of a lamellar morphology [FIG. 1.10].

By describing the surfactant layer as a mathematical surface, the curvature energy concept proposed for lipid bilayers by Helfrich in 1973 can be adapted in here [17]. Helfrich recognized that the lipid bilayer resembles a nematic liquid crystal at room temperature and then proposed the curvature energy per unit area for the lipid bilayer. Inspired from this, the flexible surface model is useful for a theoretical analysis of the structures formed by the surfactants [18, 19]. The basic concept in the Helfrich description is to assign a curvature free energy (F_b) to a small section of surface (1.4), obtained as a surface integration of a local curvature free energy density f . Equation (1.4) defines the energy required to bend a layer of area of preferred curvature c_0 to a shape with principal curvatures c_1 and c_2 . To get the total free energy, the local free energies are summed up for all

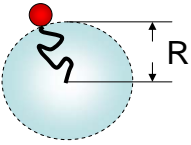
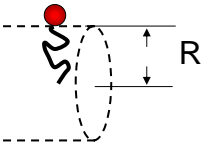
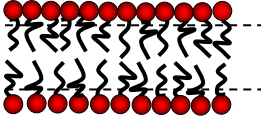
Principal radius R_1	Principal radius R_2	Curvature c	Morphology taken
R	R	$\frac{1}{R} + \frac{1}{R} = \frac{2}{R}$	sphere 
R	∞	$\frac{1}{R} + 0 = \frac{1}{R}$	cylinder 
∞	∞	0	lamella 

Figure 1.10: Morphologies determined by different curvatures of surfactant layer, spherical, cylindrical and lamellar structures.

small areas of the monolayer (1.6) .

$$f_{bend}^{Hel} = \frac{1}{2}\kappa(c_1 + c_2 - c_0)^2 + \bar{\kappa} c_1 \cdot c_2. \quad (1.4)$$

$$F_b = \int f_{bend}^{Hel} dA \quad (1.5)$$

$$F_b = \int_{membrane} \left\{ \frac{1}{2}\kappa(c_1 + c_2 - c_0)^2 + \bar{\kappa} c_1 \cdot c_2 \right\} dA \quad (1.6)$$

κ and $\bar{\kappa}$ are the mean and Gaussian curvature elastic moduli. These moduli are also termed as bending and saddle splay moduli. In a membrane, the bending moduli κ is related to the thickness of the membrane and controls the amplitude of thermal curvature fluctuations. The saddle splay modulus $\bar{\kappa}$ depends on the topological complexity [3], for example $\bar{\kappa}$ gives the elastic energy required in the variation of topology lamellae, by introducing passages between layers to become sponge. Also the Helfrich bending free energy contains a characteristic

curvature c_0 , called the "spontaneous curvature". We have discussed the normal curvatures of the surfactant monolayer, but did not discuss yet how it differs from the "preferred" or the "spontaneous curvature". As sketched in FIG. 1.11 and FIG. 1.13, each piece of monolayer is curved at the hydrophilic-hydrophobic interface of the surfactant molecule. The size of the polar head can be varied by

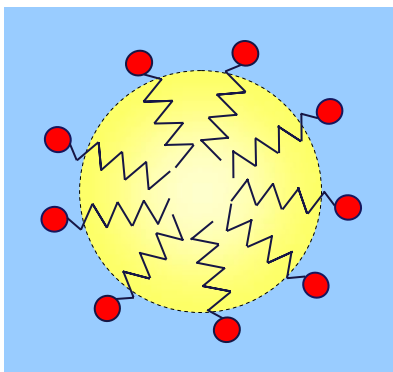


Figure 1.11: Curved interface formed by hydrophilic heads and hydrophobic chains of surfactant molecules of a swollen inverted micelle with oil (yellow) in water (blue).

regulating the number of water molecules attached to the hydrophilic head group (known as hydration) [FIG. 1.12]. Micelle hydration number per amphiphile in SDS is reported as around 9 [20]. This variation of the water molecules attached to the polar heads, changes the curvature of the surfactant monolayer. Often there are no sufficient water molecules available such that the head groups can be optimally hydrated.

What happens if there are sufficient solvent molecules to provide an optimal hydration of the surfactant? In such situations, as a result of the instinctive property of the surfactant, the curvature formed is spontaneous in a given environment. But what happens if there is a constraint of less water molecules for the surfactant layer? Then the surfactant molecules have to be satisfied with less hydration. Thus the curvature formed with the scarcity of water molecules is different from the spontaneous curvature formed with enough water molecules [FIG. 1.13]. The surfactant molecules self-assemble into aggregates with an interfacial curvature 'c' closest to the spontaneous curvature, c_0 .

For non-ionic surfactants, hydration of ethylene oxide molecules determine

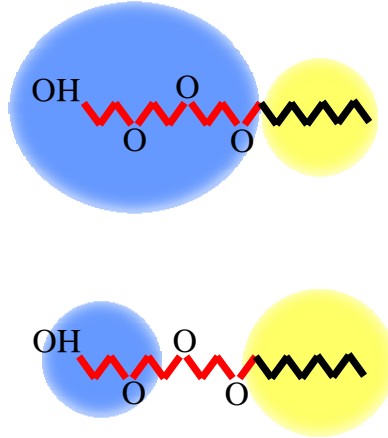


Figure 1.12: Schematic diagram of changing size of the polar region of a non-ionic surfactant molecule with changing hydration. Blue color represents hydrated water molecules.

the head group size. Since the solubility of non-ionics are highly dependent on temperature, α_{op} too depends on temperature. This means that the curvature of non-ionics has a strong temperature dependence.

1.7 Emulsions

Emulsions are immiscible liquid dispersions stabilised by surfactants. The term '*stabilise*' ranges from a few minutes to years. Depending on the size of the dispersed particles, emulsions can be classified to

- (1) macroemulsion: droplet size from 1.5 - 100 μm
- (2) miniemulsion: droplet size from 50 - 500 nm and
- (3) microemulsion: droplet size from 3 - 50 nm .

Physical appearance of the emulsion depends on the scattering of light by the droplets of the dispersed phase. The scattering intensity, $I \sim R^6$, where R is the droplet radius. As the droplet diameter decreases, appearance of the emulsions range from a milky solution or "macroemulsion" (scatters the entire spectrum of incident visible light) through a gray translucent solution or "miniemulsion" (the droplets are too small to scatter the entire spectrum of incident visible light) and

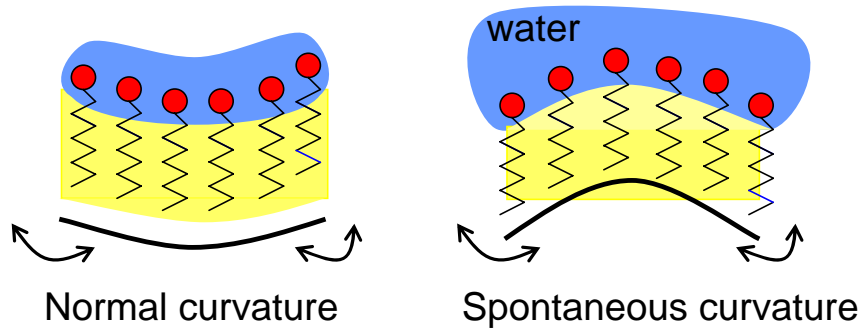


Figure 1.13: normal curvature of the surfactant monolayer (less water molecules to hydrate) and spontaneous curvature of the surfactant monolayer (no constraint of water molecules). Blue and yellow color represents water and oil respectively.

finally to a transparent solution or "microemulsion" (with droplet diameter less than the wavelength of the incident visible light).

Despite their structural similarities, microemulsion and macroemulsion differ substantially in their physical and thermodynamic properties. In the case of macroemulsions, the diameter of the droplets grows continuously with time, so that phase separation eventually occurs under gravitational forces; i.e., they are kinetically stable and their formation requires input of work. In the case of microemulsions, once the right physio-chemical conditions are achieved, microemulsification occurs spontaneously; they are thermodynamically stable and isotropic. Since creaming and flocculations are absent, microemulsions have been an interest for practical applications [21].

1.8 Microemulsions

Microemulsions, macroscopically homogeneous mixture of water and oil, spontaneously forms by the addition of surfactant. The word "microemulsion" was originally proposed by Jack H. Schulman in 1959, although the first paper on the topic dates from 1943 [22, 23, 24, 25, 26].

They are thermodynamically stable and transparent mixtures, in general with low viscosity. Microscopically they are heterogeneous and form a multitude of

structures. The fascinating shapes and forms of microemulsions are related to the properties of extended ($\approx 10..100 \text{ m}^2/\text{cm}^3$) surfactant monolayer at water-oil interface. Nearly monodisperse droplets, lamellar structure with alternative layers of water-surfactant and oil-surfactant, cylindrical and sponge like structures have been observed. They can have unique properties like, ultralow interfacial tension and the ability to solubilise other immiscible liquids. Their fascinating thermodynamic and kinetic behavior has been a focus of fundamental research in the colloid science for the last few decades. A gradual change in temperature of 10 K can lead to a succession of more than four phase transitions with vastly different macroscopic properties. For several systems, these morphologies and the approximate extent of the structures in the phase diagram is known due to the improved experimental techniques (microscopy, light-, electron- and neutron scattering, NMR). These improved characterization contributed to the theoretical and computational modeling of phase diagrams.

1.9 Phase Behavior of Microemulsion

A simple ternary system with water, oil (an alkane) and a non-ionic surfactant can form a microemulsion at appropriate conditions. The properties and phase behavior of this system is almost universal for many kind of microemulsion systems. The temperature and composition dependent phase diagram of microemulsion with non-ionic surfactants of type C_iE_j have been extensively studied by Kahlweit, Strey, Olsson and co-workers [27, 28, 29]. We have chosen C_8E_3 and C_4E_1 as model surfactants for our investigations due to the well characterised records of water-alkane- C_iE_j . Microemulsion have mainly three different macroscopic phases which have been systematised, and will be discussed in the following sections.

1.9.1 Gibbs phase triangle

A Gibbs phase triangle for microemulsions is a ternary phase diagram showing the phase behavior with changes in the volume fractions of water-oil-surfactant. This is an empirical visual observation of the system and sometimes neglects a

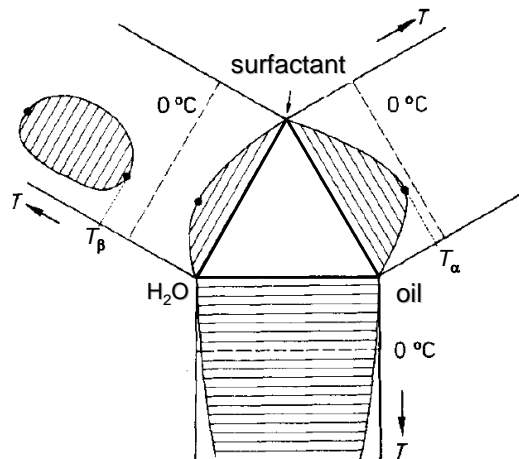


Figure 1.14: 'Unfolded' phase prism of water-oil-nonionic surfactant system showing the three binary phase diagrams. Shaded portions in figure show the miscibility gaps.

co-surfactant added to the mixture. Under isobaric conditions, a phase prism can be constructed with the Gibbs phase triangle water-oil-surfactant taken as the base of the phase prism and temperature as forth ordinate [see FIG. 1.14].

Unfolding the temperature axis gives three binary systems, water-oil, water-surfactant and surfactant-oil [2, 30] [see FIG. 1.14]. [T_α is the upper critical solution temperature (UCST) which is the critical temperature above which the components are miscible in all proportions. The critical temperature below which the components of a mixture are miscible for all compositions is the lower critical solution temperature (LCST) represented here as T_β]. At lower temperatures all these three systems show a miscibility gap. A miscibility gap is called the region in which two phases, with essentially the same structure, have no solubility in one another or do not mix. The water-oil binary system shows a miscibility gap over the complete experimental temperature range. The phase diagram for oil-surfactant mixtures show a lower miscibility gap. Its T_α (UCST) is mostly below zero degree Celsius. The phase diagram of water- surfactant mixture is more complicated in comparison with the other two systems. It shows two miscibility gaps at different temperature with a lower and upper critical points cp_β , cp_α at temperatures T_β and T_α . The LCST (T_β) of the upper miscibility loop could

probably play a role in the phase behavior of the microemulsion [2].

The schematic phase prism for water-oil-surfactant system with the phase diagrams at different temperatures is shown in FIG. 1.15.

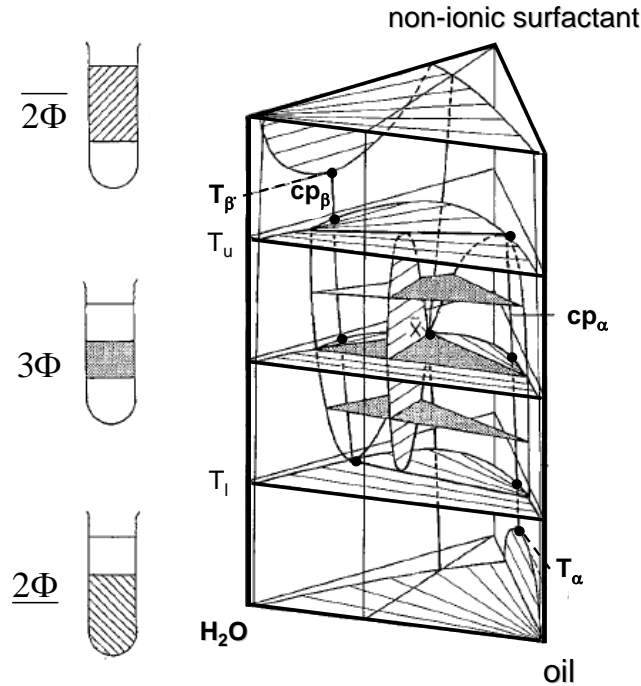


Figure 1.15: Schematic phase prism for a water-oil-nonionic surfactant system with broken critical lines. Macro-state of the microemulsion sample is sketched in the left side. For a description see the text. Figure adapted from [2]

1Φ - region : The single phase region is a macroscopically homogeneous phase (Winsor IV) [31]. Here microemulsion solubilises all water and oil. However, the surfactants self-assemble into different morphologies, depending on the temperature and composition. For example, water droplets in oil, lamellar structure, bicontinuous, oil droplets in water etc have been observed.

2Φ - region : There are two types of 2Φ - regions. (a) In $\overline{2\Phi}$, oil-in-water (o/w) microemulsions coexists with an oil rich phase where surfactants are only present as monomers at small concentration (Winsor I)[31]. (b) In $\underline{2\Phi}$, water-in-oil (w/o) microemulsions coexists with a surfactant-poor water phase (Winsor II)[31].

3 Φ - region : In a three-phase system, a surfactant-rich middle-phase (a microemulsion phase) coexists with both, a water rich and oil rich phases (Winsor III or middle-phase microemulsion) [31]).

1.9.2 Fish cut phase diagram

Determination of the entire phase prism is very time consuming. A section through the phase prism, where the ratio of two components is fixed, and the composition of the third component and temperature are varied, turned out to be very useful. As non-ionic microemulsions show a strong temperature-dependent phase behavior, sections at fixed water to oil ratio have frequently been studied [FIG. 1.16]. A section through Gibbs phase prism at constant water to oil ratio and varying non-ionic surfactant concentration is called a 'Fish cut' phase diagram [FIG. 1.17]. 'Fish cut' phase diagrams got the name due to its characteristic fish

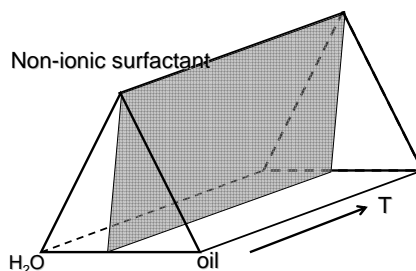


Figure 1.16: Schematic phase prism of water-oil-nonionic surfactant mixture. The shaded region shows a vertical section with fixed water to oil ratio. microemulsion

like shape [32] [FIG. 1.17]. Often a fish-cut phase diagram is given by volume fractions. We denote the volume fractions of water, oil and surfactant as ϕ_w , ϕ_o and ϕ_s respectively. The volume ratio of oil in the mixture of oil and water is ;

$$\alpha_o = \frac{\phi_o}{\phi_w + \phi_o}$$

The respective volume ratio of surfactant in the mixture is given by

$$\alpha_s = \frac{\phi_s}{\phi_w + \phi_o + \phi_s}$$

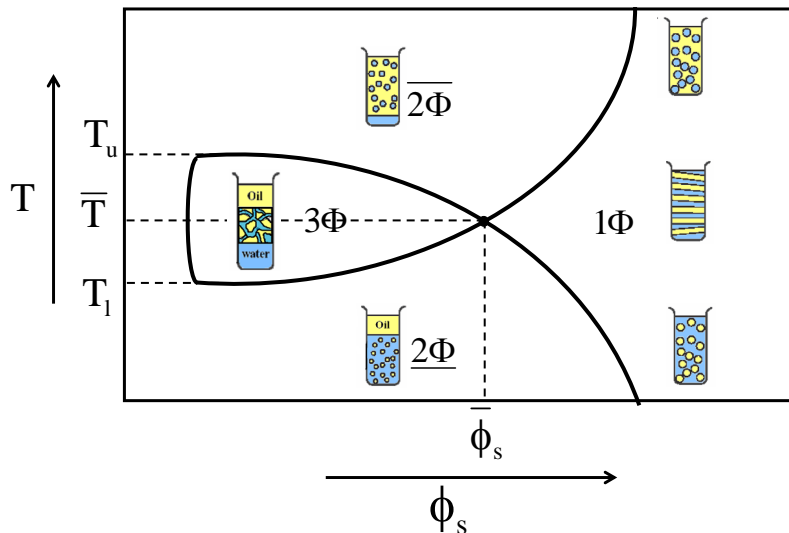


Figure 1.17: Schematic 'fish cut' phase diagram of a non-ionic microemulsion with equal water to oil proportion as a function of surfactant concentration. The 'body' of the fish has a surfactant-rich phase coexisting with a water and a oil-rich phase, from a temperature region T_l to T_u (marked with dashed line). The 'tail' of the fish has a single phase region starting from $\bar{\phi}_s$ towards higher ϕ_s . On the either side of the body of the fish, a microemulsion phase coexist with a water-rich or oil-rich phase.

The phase diagram shows the three-phase region floating like a 'fish' and the one-phase region forming the 'tail' of the fish. In a fish cut diagram the 3Φ -region extends from T_l to T_u . T_l to T_u are the lowest and highest temperature where a 3Φ -region can show up [32]. The temperature (\bar{T}) at which "fish body" intersects the "fish tail" is called the phase inversion temperature (PIT) or tricritical point [33]. The temperature $\bar{T} \approx (T_l + T_u)/2$. For some surfactant-oil-water mixtures, the phase diagram is symmetric on either side of \bar{T} . The phase inversion temperature (\bar{T}) depends only on the components of the particular microemulsion. The surfactant concentration at the tricritical point ($\bar{\phi}_s$) represents the efficiency of a surfactant too. It is the minimum amount of surfactant required to completely emulsify equal amounts of water and oil. In a fish cut diagram at very low concentrations, a gap can be formed before the body of the fish (3 phase region). This is related to the CMC of the surfactant. For long chain surfactants like $C_{12}E_5$, the 3Φ region starts at a surfactant concentration below 1 wt%, whereas for short

chain surfactants like C_4E_1 , the minimum amount of surfactant required to form a 3Φ microemulsion can be as high as 10 wt%.

The two phase boundaries which make a 'fish' are named according to the solvent emulsified. (a) At $T \geq \bar{T}$, across the phase boundary, microemulsion expels water [2, 34]. Now, a microemulsion phase coexists with a water-rich phase ($2\bar{\Phi}$). The phase boundary along which this happens is called water emulsification boundary [web] and the temperature is denoted by $T_{WEB}(\phi_s)$ [35]. (b) Under cooling a microemulsion expels oil if $T \leq \bar{T}$. Microemulsion then coexists with an oil-rich phase (2Φ). The phase boundary along which this happens is called oil emulsification boundary [oeb] and the temperature dependence is denoted by $T_{OEB}(\phi_s)$.

On an average, the surfactant monolayer is curved towards oil for $T \leq \bar{T}$ and curved towards water for $T \geq \bar{T}$. As discussed earlier, along $T = \bar{T}$, the morphology of the surfactant monolayer tends to be bicontinuous or lamellar. This again depends on the concentration of surfactant. At low concentrations, $\phi_s \leq \bar{\phi}_s$, the surfactant monolayer takes a bicontinuous topology whereas at high concentrations $\phi_s \gg \bar{\phi}_s$ a high viscous lamellar structure can be formed. Surfactant monolayer takes droplet form when it approaches the phase boundary.

1.9.3 Strong and weak surfactant

Surfactants can be classified according to their '*strength*' in their surface active properties. In the case of non ionic surfactants of type C_iE_j , for (i, j) larger than about $(8, 3)$, the surfactants are considered to have a long chain. They bind strongly to the interface and are called 'strong surfactants'. They possess a sharp interfacial profile. Surfactants with $(i, j) < (8, 3)$ possess short chains and hence attach to the interface in a rather disordered way. Due to the fast exchange of the surfactant molecules with water and oil, the interface tends to become diffuse for shorter chain surfactants. These surfactants are termed as weak surfactants. Example: Pentaethylene glycol monododecyl ether ($C_{12}E_5$) is a strong surfactant and 2-butoxyethanol (C_4E_1) is a weak surfactant and triethoxy mono-octylether (C_8E_3) is a moderate surfactant. The critical micellar concentration (CMC) for strong surfactant is much lower than for a weak surfactant. Example: CMC of

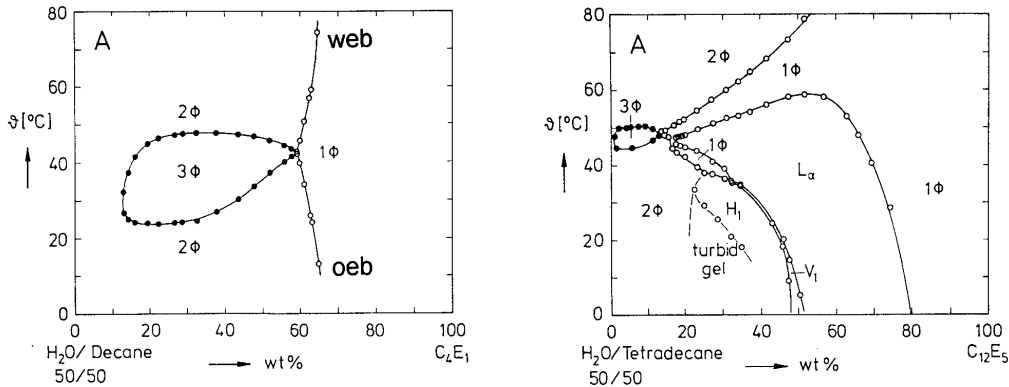


Figure 1.18: Comparison of the phase diagrams of microemulsions with a weak (C_4E_1) and a strong ($C_{12}E_5$) surfactant.

$C_{12}E_5$ is 0.07 mM and C_4E_1 is 1.2 M [36, 37]. So microemulsions with strong surfactants need comparatively less mass fraction of surfactant to form a macroscopically homogeneous mixture of water-oil-strong surfactant. While, water-oil-weak surfactant mixture need large mass fraction of surfactant to form a homogeneous microemulsion. If not stated otherwise, the surfactant concentration is given as volume fraction in the rest of this thesis.

Strong surfactants shows a rich phase behavior. Microemulsion with strong surfactants have a small 3Φ - region. On contrary microemulsions with weak surfactant have a comparatively simpler phase behavior with a large 3Φ - region.

1.10 Concepts and Theoretical Modeling of Microemulsions

Various theoretical models have been developed during the last few decades to understand the phase behavior of microemulsions. It is a big challenge to every theoretical model to explain the generic behavior of microemulsions observed in experiments especially the bicontinuous structure observed in microemulsions. Almost all the theoretical models of the microemulsions incorporate the amphiphilicity of the surfactant. Apart from lattice models [38, 39], Ginzburg-Landau [33, 40] and phenomenological (membrane and related approaches)[17, 41] have been in-

troduced [reviewed in [33]]. The major difference between different models is due to the variables - microscopic densities in the lattice models, order parameters in Ginzburg Landau and experimentally accessible parameters in phenomenological models.

Early papers on microemulsion theories are from Talmon and Prager [42]. They developed a thermodynamical model to describe bicontinuous microemulsions. Their approach picturise microemulsions as a random geometry of interspersed oil and water domains (Voronoi polyhedra) with the surfactant adsorbed at the boundaries. Here, the fluctuations of the monolayers are neglected.

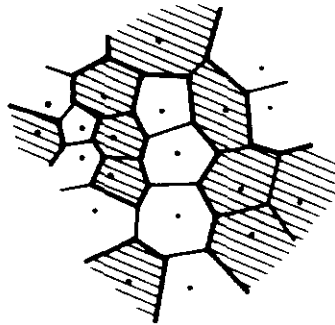


Figure 1.19: Oil (shaded) and water (unshaded) domains generated by the Voronoi process. Heavy lines denote the surfactant monolayer

Phenomenological lattice models have been investigated by Ruckenstein [43] De Gennes and Taupin [44], Jouffroy, Levinson, and De Gennes [45], Widom [46], Andelman [47] et al. These models employ a lattice parameter ' ξ ' as the characteristic length scale to calculate the configurational (mixing) entropy of a microemulsion. The lattice parameter is typically of the order of the dimension of an oil or a water mesophase.

Talmon and Prager's model was later modified by de Gennes and coworkers [44, 45]. They retained the physical content of Talmon and Prager's model for a bicontinuous morphology in a simpler picture of regularly packed arrays of cubic cells as sketched in FIG. 1.20.

These cubic cells are then randomly filled with oil and water. The surfactant film separates the cells. de Gennes justified his approach by Schulman's observation that a bicontinuous phase has a nearly vanishing interfacial tension, $\gamma \approx 0$.

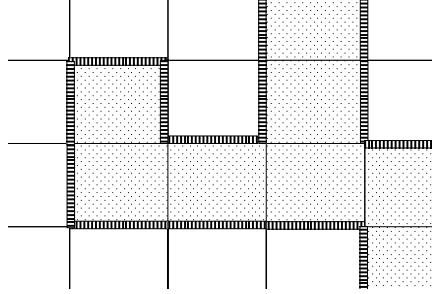


Figure 1.20: Array of cubical cells randomly filled with water (shaded) and oil (white). Surfactants reside on the dark lines separating oil and water domains.

Furthermore they assumed that the number of molecularly dissolved surfactant molecules are negligible [44, 48]. This allowed Andelman et al. to relate the ratio of the surfactant interfacial area (S) to the volume (V),

$$\frac{S}{V} = \frac{6\phi_o\phi_w}{\xi}$$

where ϕ_o and ϕ_w are the oil and water fractions and ξ is the edge length of the cubes. ξ is defined in such a way that at larger length scales the interface can be folded or wrinkled and for the length scale smaller than ξ , the interface is flat. Since ξ^2 is the average interfacial area between two differently filled cubes, it relates to the number of oil - water nearest neighbour domains.

De Gennes's description of the oil-water interface, for the explanation of certain phase transitions is purely entropy based. The geometrical entropy of the surfactant film is approximated by the entropy of random mixing. Within this picture, the energy per unit volume is $6\gamma\phi_o\phi_w/\xi$. Here γ is the oil-water interfacial tension. In order to minimise the free energy of a three phase system, to attain equilibrium, the cube cell size ' ξ ' is set to vary instead of keeping it fixed. So a mixing on a scale, smaller than ξ does not happen. Another variation of the model has been worked out by Reiss et al. Instead of the cube cell size, he took the molecular length of a surfactant molecule as the fundamental length scale for the analysis of entropy folding of the surfactant film [49]. Kahlweit, Reiss and co worker's emphasized on the effect of surfactant concentration on the film rather than the effect of curvature [50, 51].

Another class of models are **microscopic lattice models**. Here lattice points are considered for analytical convenience but several of these models had the disadvantage of artifacts. One of the earlier lattice model is from Wheeler and Widom [52]. They pictured the molecules as difunctional or 'diatomic' : AA (oil), BB (water) and AB (surfactant). Like many of the current lattice models, the configurations of the molecules are restricted in this model also. Here only the like ends of the molecules meet, so the configuration is uniquely A end or B end. This makes the model equivalent to a spin 1/2 Ising model, where each site is uniquely a \uparrow site or a \downarrow site. This earlier model had a draw back of the absence of a three phase region. This is due to considering only the nearest neighbour spin-spin interactions leading to one phase and two phase microemulsions.

Later this model has been generalised by including interaction energies, which gave extremely rich phase diagrams. These generalised models considered further neighbour sites and three-spin interactions too. Here the free energy of the system is obtained from the partition function which is again obtained from the sum of all possible numbers and all possible configurations of AA, BB and AB molecules (oil, water and surfactant). Similar kind of lattice models have been worked out by Schick and Shih [38], Robledo [53, 54], Matsen and Sullivan [55] and several other groups. But none of them could calculate the partition function analytically even though approximations were made [39]. Among those, "mean-field" approximation is most common. The mean-field approximation relates the free energy F_1 of a system with Hamiltonian H_1 to the free energy F_0 of a reference system with Hamiltonian H_0 by

$$F_1 = F_0 + \langle H_1 - H_0 \rangle_0$$

where the probability $\langle \rangle_0$ of a configuration is weighted with a Boltzmann factor proportional to $\exp(-H_0/kT)$. Mean field theories fail to account for the fluctuations of the surfactant film.

Ginzburg-Landau models is an approach characterised by an expansion in terms of an order parameter. It can explain many generic aspects of the considered ternary mixtures including the morphology of the surfactant monolayer close to phase transitions. This model has a disadvantage of coupling constants which are not directly related to physically measured quantities. Due to several parameters, a quantitative comparison between the result and experiment is also

difficult.

Phenomenological (membrane and related approaches) are particularly useful for investigating the phase behavior since the microstructures can be described via experimentally determined parameters. A description of the interface based on 'Helfrich energy' [56, 57, 58] which includes bending rigidities and spontaneous curvature (c_0) of the interfacial surfactant layer turned out to be successful in modeling the phase transitions in amphiphilic mixtures.

1.11 Free energy discussions for the non-ionic microemulsion

The most relevant contributions to the free energy result from (a) the bending energy of the interface F_b , (b) from the entropy of mixing of water and oil domains F_{mix} in a microemulsion phase, and (c) from the undulations of the monolayers F_u in a lamellar phase. Since the discussions are on non-ionic surfactants, electrostatic contributions to the free energy are irrelevant. The free energy arising from the bending of an interfacial monolayer was introduced by Helfrich for the description of lipid bilayers [56]. Later the concept was applied to describe surfactant monolayers at the water-oil interface by various authors starting from de Gennes and Taupin [44]. The free energy per unit area arising from the bending of the interfacial monolayer is

$$F_b = \frac{\kappa}{2} \left[\frac{1}{R_1} + \frac{1}{R_2} - 2c_0 \right]^2 + \bar{\kappa} \frac{1}{R_1 R_2} \quad (1.7)$$

Here R_1 and R_2 are the local radii of curvature. The bending modulus κ and the Gaussian modulus $\bar{\kappa}$ and the spontaneous curvature $c_o(T)$ are empirical material constants. The total water-oil interfacial area can be expressed as $A/V = \frac{\phi_s}{l_s}$. Then the free energy per unit volume can be written as,

$$F_b = \frac{\phi_s}{l_s} \left\{ \frac{\kappa}{2} \left[\frac{1}{R_1} + \frac{1}{R_2} - 2c_0 \right]^2 + \bar{\kappa} \frac{1}{R_1 R_2} \right\} \quad (1.8)$$

Helfrich [56] first calculated the free energy of the lamellar phase, which arises

from the steric interaction of undulating lamellar sheets. Fluctuations can have a major contribution to the free energy. Helfrich's calculation on the free energy has been generalized [47] to the specific case of bilayer sheets, so that the free energy density of the lamellar phase due to undulations is given by,

$$F_u = (k_B T)^2 \frac{\chi \phi_s^3}{\kappa 4l_s^3} \left(\frac{1}{\phi_o^2} + \frac{1}{\phi_w^2} \right) \frac{1}{\phi_o + \phi_w} \quad (1.9)$$

χ is a prefactor with a value approximately 0.05 [47, 59, 60].

Another contribution to the free energy is the different possibilities in distributing water and oil droplets in space.

$$F_{mix} = (k_B T) \frac{\phi_s^3}{6l_s^3 \phi^3 (1 - \phi)^3} \left[\phi \log \phi + (1 - \phi) \log(1 - \phi) \right] \quad (1.10)$$

where ϕ corresponds to the volume fraction of enclosed phase (either water droplet or oil droplet). The only temperature dependence of this entropy of mixing is the prefactor $k_B T$. Studies on the temperature dependence of the free energies per unit volume for single phase mixtures with different morphologies showed that the contributions to the free energy due to the entropy of mixing F_m and the undulations of the lamellae F_u are nearly constant within a temperature interval of 298 K to 320 K [60]. Moreover the values are similar. But the values for the bending free energies show a strong temperature dependence. For this reason the contributions to the interfacial free energy per unit volume due to undulations of the lamellae F_u and due to mixing of water and oil domains F_m are negligible, for the description of the temperature dependent phase diagrams and the specific heat of the microemulsion sample.

1.12 Size of droplets

1.12.1 One Phase Region

In the 1Φ - region the size of the droplet is determined by the composition of the microemulsion. It hardly depends on temperature, therefore its temperature dependence can be ignored in the following considerations. The size of the droplet

can be calculated from the conservation of volume and area.

Here according to the volume conservation,

$$V \cdot \phi_d = N \times \frac{4}{3}\pi R^3 \quad (1.11)$$

where N denotes the number of droplets in a volume element V . ϕ_d is the enclosed volume obtained from the sum of the interior volume and the respective oil/water soluble part of the surfactant. For symmetric surfactants, i.e surfactants where the volume of the hydrophilic head almost equalises those of the hydrophobic tail, ϕ_d is given by :

$$\phi_d^w = \phi_w + \frac{\phi_s}{2} \quad (1.12)$$

$$\phi_d^o = \phi_o + \frac{\phi_s}{2} \quad (1.13)$$

According to the area conservation,

$$V_s \cdot \phi_s = N \cdot 4\pi R^2 \cdot l_s \quad (1.14)$$

l_s gives the effective thickness of the surfactant monolayer. From the ratio of both (13) and (16), the radius of the water droplet is given as

$$R_w = \frac{3l_s\phi_d}{\phi_s} \quad (1.15)$$

and similarly we get the size of oil droplet as

$$R_o = -\frac{3l_s\phi_d}{\phi_s} \quad (1.16)$$

To distinguish water and oil droplets, the radius of oil droplet is taken to be negative.

1.12.2 Two Phase Region

According to Eq.1.15, with increasing volume fraction of water and fixed surfactant concentration, the average size of the droplets should increase. But above the emulsification boundary ($T > T_{WEB}$) droplets cannot emulsify all the water.

With increasing temperature the hydration of the hydrophilic group of the surfactant decreases, causing that the effective head volume decreases. This implies stronger bending of the surfactant monolayer towards water.

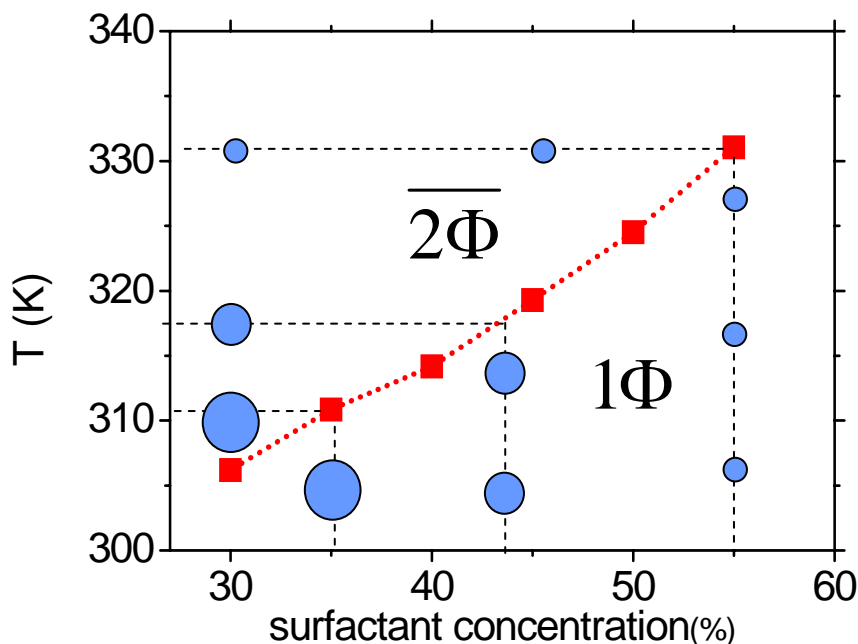


Figure 1.21: A small portion from the fish cut phase diagram to show the droplet size in the 1Φ and 2Φ region. Red squares show the water emulsification boundary, WEB. Blue circles are the schematic representation of water droplets. At temperatures $T < T_{web}$, droplet size is independent of temperature while at $T > T_{web}$ the size of droplets are temperature dependent. Along the dashed line droplet size is the same.

In other words, below (T_{WEB}) in the 1Φ region the microemulsion contains too little water for the droplets to take their optimum size (i.e. to get their spontaneous curvature). So at the emulsification boundary (T_{WEB}), the volume fraction of water that can be emulsified is maximum i.e. $\phi_w = \phi_w^{WEB}$. For $T > T_{WEB}$ the excess water is expelled and coexists with the microemulsion phase to form a 2Φ -microemulsion. So Eq.1.15 holds only upto the emulsification boundary. In a 2Φ region the droplet size is determined by the temperature. At the emulsification boundary, there is a maximal volume fraction of water that can be emulsified which leads to the optimal size of the droplets, R^{opt} . In a 2Φ region, the droplets

take a size R^{opt} [57]. Since non-ionic surfactant gets less hydrophilic with increase in temperature, R^{opt} for water droplet $R_w^{opt}(T)$ decreases with increasing temperature. At water emulsification boundary (WEB),

$$R_w = R_w^{opt}(T) \quad (1.17)$$

Similarly at oil emulsification boundary (OEB),

$$R_o = R_o^{opt}(T) \quad (1.18)$$

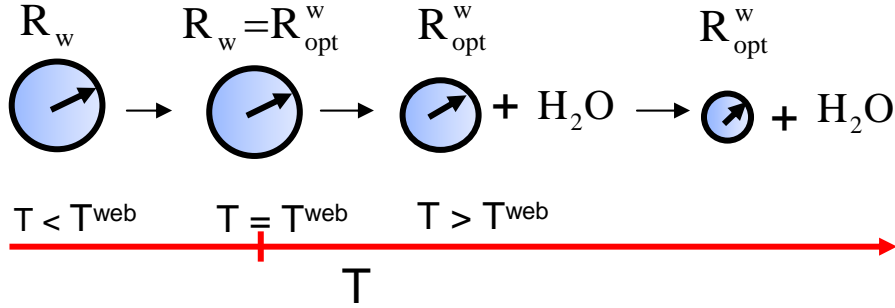


Figure 1.22: Change of droplet radius with increasing temperature. The schematic diagram shows how the radius changes with temperature, ranging from one phase ($T < T_{web}$) to two phase ($T > T_{web}$), when crossing the water emulsification boundary (T_{web}).

The temperature dependence of the droplet radius cannot be obtained from Eq 1.15 and Eq 1.16. The optimum radius in two-phase region has been determined by SANS experiment for $C_{12}E_5$ - water - octane and a phenomenological relation shows the variation of R^{opt} with temperature T [18, 61].

$$R^{opt}(T) \simeq \frac{1}{a(T - \bar{T})} \quad (1.19)$$

where $a = 1.2 \times 10^{-3} K^{-1} \text{\AA}^{-1}$ [18, 61]. This equation works good for long chain

(strong) surfactants in a well defined temperature region.

In a 2Φ - region, only the surface area of the droplet is preserved. Since R^{opt} is the radius that locally minimises the interfacial free energy, it depends on the spontaneous curvature. From Eq 1.8, Helfrich bending free energy per unit volume for spherical droplets ($R_1 = R_2 = R$) can be written as

$$F_b = \frac{\phi_s}{l_s} \left\{ \frac{\kappa}{2} \left(\frac{2}{R} - 2c_0 \right)^2 + \frac{\bar{\kappa}}{R^2} \right\} \quad (1.20)$$

$$F_b = \frac{2\kappa\phi_s}{l_s R^2} \left\{ [1 - Rc_0(T)]^2 + \frac{\bar{\kappa}}{2\kappa} \right\} \quad (1.21)$$

The optimum radius $R^{opt}(T)$ is specified by $\partial F/\partial R = 0$.

$$\frac{\partial F_b}{\partial R} = \frac{2\kappa\phi_s}{l_s} \frac{\partial}{\partial R} \left\{ \frac{[1 - Rc_0(T)]^2}{R^2} + \frac{(\bar{\kappa}/2\kappa)}{R^2} \right\} \quad (1.22)$$

$$= \frac{2\kappa\phi_s}{l_s} \left\{ \frac{-2[1 + \bar{\kappa}/2\kappa]}{R^3} + \frac{2c_0}{R^2} \right\} = 0 \quad (1.23)$$

which gives the optimum radius,

$$R^{opt}(T) = \frac{[1 + \bar{\kappa}/2\kappa]}{c_0(T)} \quad (1.24)$$

Equation 1.24 shows that the optimum radius depends on the spontaneous curvature which is depends on temperature via the temperature dependence of the spontaneous curvature, $c_0(T)$.

1.13 Linear dependence of c_0 with T

Inserting 1.19 in 1.24 gives:

$$\frac{1}{a(T - \bar{T})} = \frac{[1 + \bar{\kappa}/2\kappa]}{c_0(T)} \quad (1.25)$$

where $\bar{\kappa}$, κ and 'a' are material constants. Therefore, to first order,

$$c_0(T) \propto (T - \bar{T}) \quad (1.26)$$

where \bar{T} is the phase inversion temperature or the tricritical point. For strong surfactants (eg: $C_{12}E_5$) this relation is well established over a temperature region near to \bar{T} . But when $T \gg \bar{T}$ and $T \ll \bar{T}$ the relation cannot be valid anymore. This is due to the saturation of the spontaneous curvature $c_0(T)$ after the drop radius decreased so much that it approaches its micellar size. However, an expression for $R_w^{opt}(T)$ and $R_o^{opt}(T)$ is required for the calculation of the temperature dependence of the emulsification boundaries. This expression should satisfy certain properties like

1) For sufficiently high temperatures ($T \gg T_l$) the size of the water droplets approaches the inverse micellar size, i. e., $R_w^{opt}(T) \rightarrow R_w^{mic}$

2) For low temperatures ($T \ll T_u$) the size of oil droplets approaches the micellar size, i. e., $R_o^{opt}(T) \rightarrow R_o^{mic}$

3) A prediction of the three phase region.

An expression satisfying all these requirements and leading to good description of the experimental data is [35]

$$R_w^{opt}(T) \equiv R_w^{mic} \frac{1}{1 - \exp(a_w(T_l - T))} \quad (1.27)$$

where $R_w^{mic} > 0$ and $T > T_l$ and

$$R_o^{opt}(T) \equiv R_o^{mic} \frac{1}{1 - \exp(a_o(T - T_u))} \quad (1.28)$$

where $R_o^{mic} < 0$ and $T < T_u$. Here R^{mic} is the micellar radii and a_w and a_o characterize the change of the optimal radius with temperature.

1.14 Emulsification boundary - 1 Φ meets 2 Φ region

At the emulsification boundary $R^{1\Phi} = R^{opt}$. Now that we have the expressions for all the radii, insert Eq 1.15 and Eq 1.16 to Eq 1.27 and Eq 1.28 respectively.

$$\exp(a_w(T_l - T)) = 1 - \frac{R_w^{mic}}{R_w^{1\Phi}} \quad (1.29)$$

$$\exp(a_o(T - T_u)) = 1 - \frac{R_o^{mic}}{R_o^{1\Phi}} \quad (1.30)$$

Solving this equation for T_{WEB} and T_{OEB} gives the composition dependence of the emulsification boundaries of water and oil droplets.

$$T^{WEB} = T_l - \frac{1}{a_w} \ln \left(1 - \frac{R_w^{mic}}{3l_s} \frac{\phi_s}{\phi_w + x\phi_s} \right) \quad (1.31)$$

$$T^{OEB} = T_u + \frac{1}{a_o} \ln \left(1 - \frac{|R_o^{mic}|}{3l_s} \frac{\phi_s}{\phi_o + (1-x)\phi_s} \right) \quad (1.32)$$

These equations imply that the WEB and OEB can be determined from the material constants in the above equation - the upper and the lower bound of the 3 Φ region T_u and T_l respectively, the micellar radii R_w^{mic} and R_o^{mic} the change of the optimal radius with temperature a_w and a_o , the volume fraction of the hydrophilic head group of a surfactant molecule x and the effective length of the surfactant l_s .

Combining Eq 1.27 and Eq 1.28 with Eq 1.24 yields a generalised expression for the spontaneous curvature.

$$c_0^w(T) \equiv \frac{[1 + \bar{\kappa}/2\kappa]}{R_w^{mic}} 1 - \exp(a_w(T_l - T)) \quad (1.33)$$

$$c_0^o(T) \equiv -\frac{[1 + \bar{\kappa}/2\kappa]}{R_o^{mic}} 1 - \exp(a_o(T - T_u)) \quad (1.34)$$

The equations 1.31 and 1.32 gives prediction to emulsification boundaries. If all the material constants in these equation can determine T_{WEB} and T_{OEB} then

it implies that it can predict all the emulsification boundaries in the Gibbs phase prism.

1.15 Nucleation and phase separation

Heating rates affect the nucleation of the droplets. A slight increase of the phase transition temperature at increasing heating rates [62] is observed. At constant heating rate, microemulsion shows an amazing phase separation kinetics [60, 63, 64]. In the 1Φ region, droplet size is independent of temperature. Passing the phase transition temperature (T_{WEB}), large water droplets are nucleated which grow and eventually sediments [FIG. 1.23]. There is a periodic change in this process leading to periodic oscillations in the turbidity of the sample [62, 65, 66, 67]. At WEB, $T \approx T_{WEB}$. The microemulsion is still in 1Φ -region, with

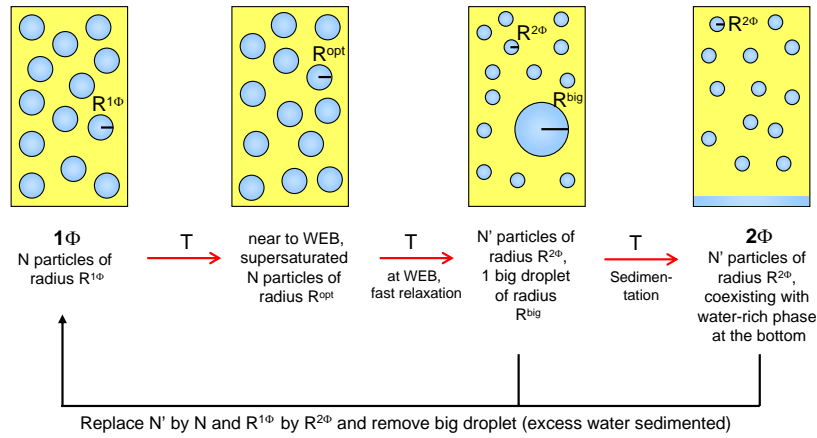


Figure 1.23: Sketch of a microemulsion with water droplets (blue circles) in an oil matrix (yellow color) under constant heating. This schematic diagram shows an idealised version of the phase separation process covering a temperature window of $T \approx T_{WEB} \pm 1K$. 1Φ microemulsion consists of N droplets of radius $R^{1\Phi}$. This radius equalises the optimum radius at the emulsification boundary. At WEB, one big drop of radius R^{big} forms and the size of other droplets ($R^{2\Phi}$) decrease. In 2Φ this big drop sedimented at the bottom.

N monodisperse droplets with radius $R^{1\Phi}$. With increase in temperature, the

water droplets want to decrease its size. This process is not easy due to the conservation of area and volume of water and surfactant. On the experimental time scale, diffusion of water molecules through the oil matrix is negligible. So the only way to exchange water and surfactant is via collisions [67]. Further heating of the sample leads to overheating and until it nucleates large droplets, which take the excess water allowing the majority of the small droplets to attain their optimum size [see FIG. 1.23]. The number of droplets continuously changes to conserve the total volume of water and of the area of the internal surface. These large droplets are energetically 'expensive' so the system has to pass an energy barrier before nucleation occurs. Large droplet takes the excess water and will merge with larger droplets. Further, they sediments to form the water-rich phase. The amplitude as well as the period of oscillations strongly depend on the heating rate (ν_s) as

$$\nu_s \equiv \frac{\Delta T}{\Delta t} \quad (1.35)$$

where T and t are the temperature and the time with which the oscillations periodically varies. These oscillations decay after several periods (nearly 20 periods) irrespective of the heating rate. A square root dependence of the period on the heating rate, $\Delta T \sim \sqrt{\nu_s}$ has been reported [62, 68].

1.16 Specific Heat

Since the phase transitions comprise changes of the structure and topology of the interface between water and oil, an effective free energy for the interface can be used to describe structural changes in the mixture [18, 19, 57, 58, 60, 69, 70]. The specific heat ' $C_v(T)$ ' involves the second temperature derivative, hence it probes the curvature of the free energy.

$$C_v = T \frac{\partial S}{\partial T} = -T \frac{\partial^2 F}{\partial T^2} \quad (1.36)$$

Bending energy for monodisperse droplets of radius R takes the form,

$$F_b = \frac{2\kappa\phi_s}{l_s R_{1\Phi}^2} \left[\left(1 - R_{1\Phi} c_0(T) \right)^2 + \frac{\bar{\kappa}}{2\kappa} \right] \quad (1.37)$$

Since the droplet radius in 1Φ ($R_{1\Phi}$) is fully determined by the composition, we can write

$$R_{1\Phi} = \frac{3l_s\phi_d}{\phi_s} \begin{cases} \approx \frac{3l_s(\phi_w+0.5\phi_s)}{\phi_s} \\ \approx \frac{-3l_s(\phi_o+0.5\phi_s)}{\phi_s} \end{cases}$$

In two phase region, the droplets can take the preferred size because only the overall interfacial area has to be conserved. Then the optimum radius is given by,

$$|R^{opt}(T)| = \frac{1 + \frac{\bar{\kappa}}{2\kappa}}{|c_o(T)|} \leq R_{1\Phi} \quad (1.38)$$

At the emulsification phase boundary ie, from 1Φ and 2Φ , droplet radius $R_{1\Phi} = R^{opt}$. Since c_0 is the only relevant temperature-dependent parameter [14,18,40], the specific heat in the 1Φ and 2Φ regions can be obtained. So the specific heat from 1.36,

$$C_v^{1\Phi} \equiv -T \frac{\partial^2 F(R_{1\Phi})}{\partial T^2} = \frac{-2\kappa\phi_s T}{l_s} \left[\frac{\partial^2 c_0^2(T)}{\partial T^2} - \frac{2}{R_{1\Phi}} \frac{\partial^2 c_0(T)}{\partial T^2} \right] \quad (1.39)$$

$$C_v^{2\Phi} \equiv -T \frac{\partial^2 F(R^{opt})}{\partial T^2} = \frac{-\phi_s T}{l_s} \left[\frac{\partial^2 c_0^2(T)}{\partial T^2} \right] \frac{\bar{\kappa}}{1 + \frac{\bar{\kappa}}{2\kappa}} \quad (1.40)$$

While crossing the phase transition boundary from 1Φ to 2Φ , a step in the specific heat signal is produced. The height of the signal is denoted by ΔC_v^{step} , which can be obtained by the difference between the specific heats in 1Φ and 2Φ .

$$\Delta C_v = C_v^{2\Phi} - C_v^{1\Phi} = \frac{4\kappa\phi_s T}{l_s} \left[\frac{\partial^2 c_0^2(T)}{\partial T^2} \frac{R_{1\Phi} - R_{opt}}{R_{1\Phi} R_{opt}} + \frac{\left(\frac{\partial c_0(T)}{\partial T} \right)^2}{\frac{1}{1 + \frac{\bar{\kappa}}{2\kappa}}} \right] \quad (1.41)$$

At the emulsification boundary $R_{opt} = R_{1\Phi}$,

$$\Delta C_v^{step} = \frac{4\kappa\phi_s T}{l_s} \frac{1}{1 + \frac{\bar{\kappa}}{2\kappa}} \left(\frac{\partial c_0(T)}{\partial T} \right)^2 \quad (1.42)$$

The specific heat is very sensitive to the changes in the curvature of the interface. This equation gives the information of change in curvature with temperature. So

from the change in the specific heat we can probe the curvature details. Since differential scanning microcalorimeter measures the temperature-dependent change of the values for the specific heat, microcalorimetry forms an extremely sensitive probe of the temperature dependence of the free energies.

Chapter 2

Materials and Experimental Techniques

2.1 Materials

Moderate surfactant: Triethylene glycol mono-n-octyl ether (C_8E_3) is a colorless and odourless liquid with molecular formula $C_{14}H_{30}O_4$ and density $0.95 \frac{g}{cm^3}$ at room temperature.

Weak surfactant: 2-butoxyethanol (C_4E_1) is a colorless liquid with ether-like smell. The molecular formula is $C_6H_{14}O_2$ and its density is $0.90 \frac{g}{cm^3}$ at room temperature.

Non-ionic surfactants are purchased from Bachem and used without further purification (water content). Water is deionised and double distilled with Milli Q purity with density $0.99 \frac{g}{cm^3}$ at $20^\circ C$. Decane and Octane (Fluka, Switzerland) used here have a purity of 99 percentage with densities $0.730 \frac{g}{cm^3}$ and $0.702 \frac{g}{cm^3}$ respectively.

Sample preparation: The samples are weighed in mass fraction according to the calculated volume fractions. Glass vials with teflon coated stoppers are used as sample containers. Sample is weighed with an accuracy of 1 milligram (Mettler toledo-AB204-S). A magnetic stirring bar was added to each vial to achieve proper mixing of the sample.

2.2 Phase behavior studied with thermo stated water bath

2.2.1 Apparatus

Phase diagrams are determined using a thermo-stated water bath [FIG. 2.1]. Briefly, it is composed of a temperature controller (HAAKE EK20), a water bath with glass windows, a magnetic stirrer, light source, a mirror and a CCD camera (Kappa,TV Lens C-0.45X, NIKON Japan). Samples are contained in 20 mm glass viols. The sample to be investigated is vertically placed in the water bath in front of the mirror. Temperature of the water bath is controlled using a HAAKE

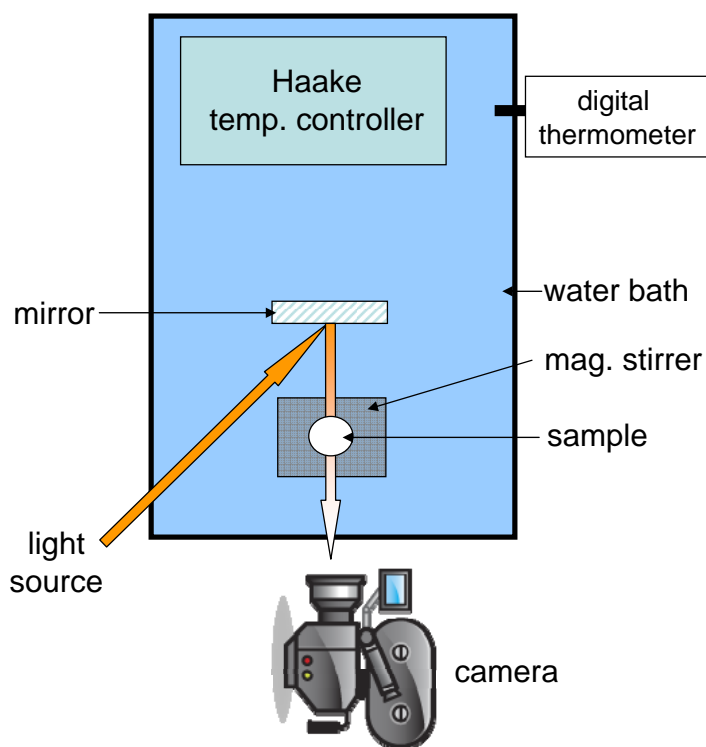


Figure 2.1: Sketch of the top view of the experimental setup: water bath, Haake temperature controller, a CCD camera, a cold light source, a mirror, a magnetic stirrer and a digital thermometer. Microemulsion samples are observed in reflected light.

EK20 with an accuracy of 0.01K. Light from the source after passing through

a cylindrical lens is directed to the mirror. The reflected light from the mirror illuminates the sample in the glass viols and the light scattered is captured in a CCD camera. This CCD is connected with a stereo microscope (NIKON US-3, Japan) so insitu the phase separation can be observed. The sensor of a digital thermometer is kept very close to the sample viol to record the temperature during the experiment.

2.2.2 Procedures to determine phase behavior

The viol containing sample is vertically immersed in a water bath. The sample is stirred using a magnetic stirring bar to ensure homogeneous mixing. A magnetic stirrer is placed under the glass vessel containing the water bath, along the vertical axis of the sample viol. The sample undergoes a temperature ramp with a predefined heating and cooling rate from 1Φ -region to final temperature of phase separation [T_{WEB} or T_{OEB}]. Simultaneously the temperature is recorded by an interfaced digital thermometer and the images are also taken.

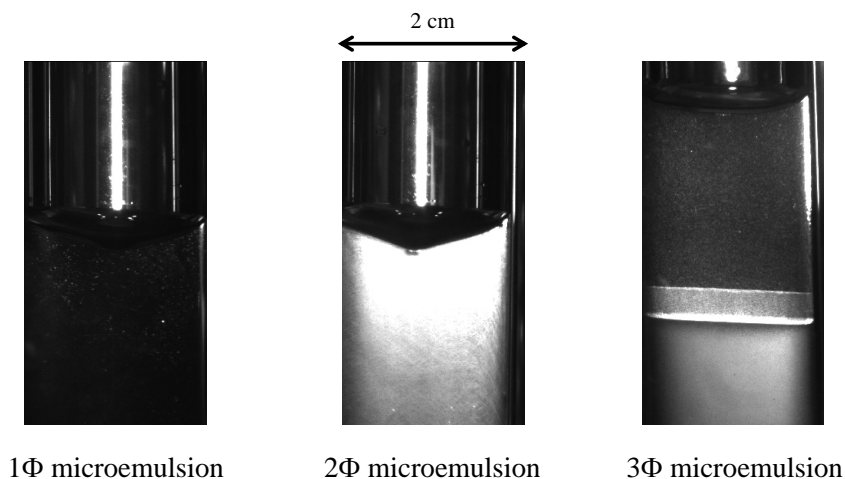


Figure 2.2: Microemulsion samples in 2cm wide viols are observed in reflected light. Left: 1Φ microemulsion appears dark due to the complete transmission of light without any scattering. Center: A 2Φ microemulsion looks turbid due to scattered light by the comparatively big droplets formed during phase separation. Right: In a 3Φ microemulsion, a thin surfactant rich area coexists with an upper oil-rich and a lower water-rich area.

Visual inspection of the sample in the scattered light gives three types of images as shown in FIG. 2.2. Since nanometer sized droplets do not scatter the white light, an isotropic- 1Φ microemulsion looks dark [FIG. 2.2, left]. From 1Φ -region, sample is heated to $\overline{2\Phi}$ get T_{WEB} whereas the sample is cooled to $\underline{2\Phi}$ to get T_{OEB} . During the temperature ramp, the system passes the emulsification boundary and bigger droplets are emulsified. These droplets make the sample turbid by scattering the light [FIG. 2.2, center]. The heating or cooling is stopped just after the appearance of the turbidity.

A 2Φ microemulsion under stirring appears turbid in the scattered light. Near to both the phase transition boundaries [T_{WEB} and T_{OEB}], average values are taken by heating and cooling across each boundary within a temperature window. T_{WEB} is the temperature of appearance (during heating from 1Φ to $\overline{2\Phi}$) or disappearance (during cooling from $\overline{2\Phi}$ to 1Φ) of the turbidity. For T_{OEB} , turbidity appears while cooling from 1Φ to $\underline{2\Phi}$ and disappears while heating from $\underline{2\Phi}$ to 1Φ . The values for T_{WEB} and T_{OEB} are averaged out from heating and cooling of a cycle [FIG. 3.1]. Due to the overheating, the experimental value of T_{WEB} from a heating cycle is slightly higher than from the cooling cycle.

Both 2Φ and 3Φ microemulsions appear turbid under stirring. Hence the surfactant rich middle phase in a 3Φ microemulsion is not distinguishable under stirring. So the phase transition temperatures of 2Φ to 3Φ cannot be determined with the earlier procedure. Instead undisturbed sample is observed at various temperatures near to the phase transition temperatures. The temperature is altered, followed by the stirring of the sample before leaving it undisturbed. Depending on the phase separation speed, the sample is kept undisturbed from hours to several days.

2.3 Differential Scanning Calorimetry

The variation of the specific heat of the solutions as a function of temperature is measured with a differential scanning calorimeter (VP-DSC, Microcal Inc.).

2.3.1 Apparatus

Calorimetric study is done using a VP-DSC which is a differential scanning microcalorimeter. It consists of two lollipop shaped fixed-in-place cells as shown in FIG. 2.3. The effective volumes of the cells are approximately 0.5 ml. The cells

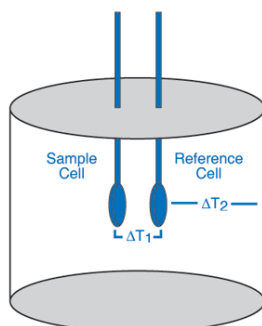


Figure 2.3: Schematic diagram of the adiabatic chamber of VP-DSC. Sample and the reference solution are filled in two lollipop shaped cells shown in blue color. ΔT shows the relative temperature differences.

are constructed from a tantalum alloy and protrude out of the adiabatic chamber via their 1.5 mm (inner diameter) access tubes. The approximate volume of each cell stem is 0.085 ml. The VP-DSC operates in the temperature range of -10^0 C to 130^0 C. Both the reference and sample cell are heated with the same constant power. The temperature difference (δT) between the cells are measured (FIG. 2.3) with a thermoelectric device. This temperature difference is driven to zero using a feedback circuit and is continuously monitored by a control unit. An exothermic (endothermic) reaction in the sample, during the temperature scan, requires less (more) power feedback to null δT . This gives the specific heat relative to a baseline. The VP-DSC is controlled by an user interface (VPViewer software) and data analysis is performed with 'Origin' software.

2.3.2 Sample

Microemulsion samples in 1Φ are used for the calorimetry because of the macroscopic homogeneity. Syringe and needle are brought to the same temperature as the sample before loading it to the cell to prevent phase separation while loading

the cells. After filling the cells are closed as soon as possible for minimising the contact with air. The air enclosed in the cell might change pressure and volume during the temperature scan. After filling the reference and the sample cell, the reference/base line is brought near to 0 cal/⁰C by adjusting the specific heat via the amount of water in the reference cell. Double distilled deionized water found to be an appropriate reference system due to the similar heat capacity.

2.3.3 Procedures to determine the step in the specific heat

A curve obtained from a calorimetric measurement at a scan rate 5K/h is shown in FIG. 2.4.

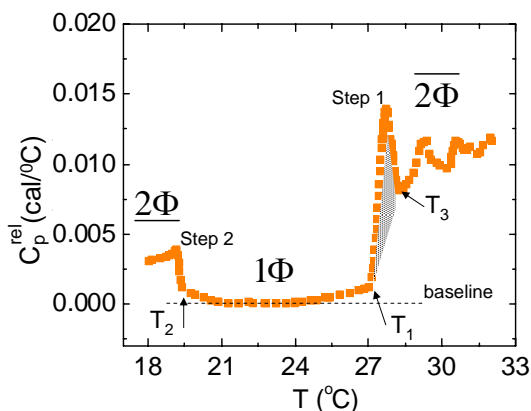


Figure 2.4: A DSC curve for water-decane- C_8E_3 microemulsion of equal volume fraction of water and oil and surfactant volume fraction, $\phi_s = 0.31$. There are two jumps of the signal: a step at lower temperature T_2 due to the oil emulsification failure across T_{OEB} (1Φ to underline- 2Φ) and the phase transition from 1Φ to 2Φ -overline is identified with a step at higher temperature T_1 in the signal (across T_{WEB}). The area under the step is shaded. Dashed line shows the baseline in one-phase region.

Here the absolute value for the specific heat is not determined, instead the specific heat of the microemulsion relative to a baseline set by the water-reference system is measured. This provides very precise data for the relative specific heat ' $C_v^{rel}(T)$ '. The liquid samples (incompressible) do not show significant change in the volume during phase transition. So we approximate $C_p^{rel} \approx C_v^{rel}$. Typical

heating rates are chosen in the range 7...30 K/h. In FIG. 2.4 two different steps can be seen at two different temperatures T_1 and T_2 .

The relative specific heat per unit volume is :

$$C^{rel}(T) \equiv \frac{\Delta Q}{\Delta T} \quad (2.1)$$

where ΔQ is the difference between the heat per unit volume absorbed by the sample and the reference system per temperature increment ΔT . The area under a step (shaded portion in FIG. 2.4) during the phase transition from 1Φ to 2Φ allows estimating the heat change ΔQ related to a structural transition

$$\Delta Q = \int_{T_1}^{T_3} dT [C_v^{rel}(T) - C_v^{base}(T)] \quad (2.2)$$

During a transition, the free energy of bulk water and oil hardly changes. A very small change of height of baseline after phase transition is due to this.

2.4 Dynamic Light Scattering (DLS)

When light passes through a microemulsion solution, the light will be scattered due to the Brownian motion of the droplets in the solution. These monodisperse scatterers are moving randomly in the scattering volume. Hence the density is fluctuating which leads to intensity fluctuations. The intensity autocorrelation is the fourier transform of the density autocorrelation. When the scattered light from two or more scatterers are added together, there will be a position and time dependent destructive or constructive interference. This leads to time-dependent fluctuations in the intensity of the scattered light. Dynamic light scattering (DLS) (Berne, 2000, Pecora, 1985), detects the fluctuations of the scattering intensity due to the Brownian motion of droplets/molecules in solution to measure the rate of diffusion of the droplets. The statistics of the scattering signal are analyzed with a correlator. The data is processed to derive the droplet size where the size is given by the "Stokes radius" or "hydrodynamic radius" of the droplet [FIG. 2.5]. This method has the advantages of short experiment duration and it is almost

all automatized.

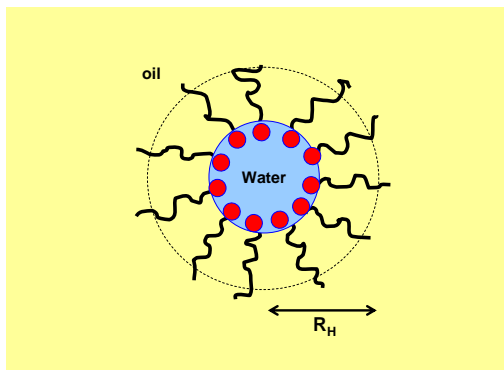


Figure 2.5: Hydrodynamic radius (R_H) of a water swollen micelle (blue color) in an oil matrix (yellow color). Hydrodynamic diameter is shown as a dashed circle.

2.4.1 DLS Theory

The experimental theory is based essentially on two assumptions. The first condition is that the particles are in Brownian motion (also called random walk) and the second assumption is that the scattering droplets used in this experiment, are spherical particles. The fluctuations are directly related to the rate of diffusion of the droplets through the solvent. The changing interference patterns due to the fluctuations in the scattering intensity can be analyzed to determine a hydrodynamic radius (R_H) for a droplet. The fluctuations are quantified via a second order correlation function given by,

$$g_2(\tau) = \frac{\langle I(t)I(t + \tau) \rangle}{\langle I(t)^2 \rangle} \quad (2.3)$$

where $I(t)$ is the intensity of the scattered light at time t , and the brackets indicate averaging. The intensity autocorrelation function $\langle I(t)I(t + \tau) \rangle$, depends only on the correlation time τ and is calculated for various values of τ ranging from 100ns to several seconds. [FIG. 2.6, left] shows a typical correlation function for a monodisperse sample. The correlation function for a monodisperse sample can

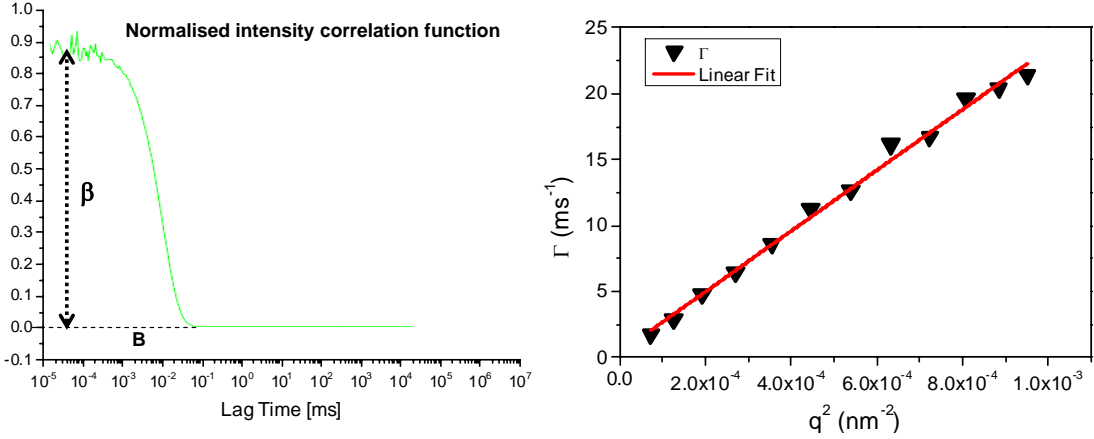


Figure 2.6: Left: The exponentially decaying autocorrelation function (green line). Right: Decay rate versus scattering vector at different scattering angles (black triangle) with a linear fit (red line).

be analyzed by the equation

$$g_2(\tau) = B + \beta \exp(-2\Gamma\tau). \quad (2.4)$$

where B is the baseline of the correlation function at infinite delay (dashed lines in FIG. 2.6 left), β is the correlation function amplitude at zero delay (dotted line in FIG. 2.6 left), and Γ is the decay rate. This measured correlation function is fitted using a regularised fit (ALV-Correlator software V.3.0) to retrieve the decay rate Γ . It is related to the diffusion coefficient using the relation [FIG. 2.6 right],

$$D = \frac{\Gamma}{q^2} \quad (2.5)$$

where q is the magnitude of the scattering vector [FIG. 2.7]. It is given by,

$$q = \frac{4\pi n}{\lambda} \sin(\theta/2) \quad (2.6)$$

where n is the refractive index of the solvent, λ is the wavelength of the incident light, and θ is the scattering angle.

The Stokes- Einstein-equation may be used to convert the measured diffusion

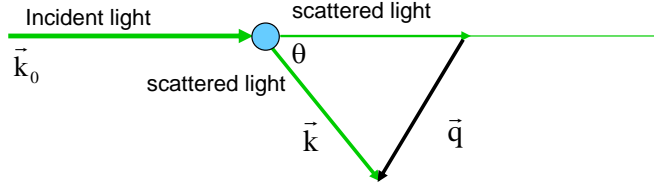


Figure 2.7: The sketch of the definition of the scattering vector $\vec{q} = \vec{k} - \vec{k}_0$. The scattering vector \vec{q} is determined by the scattering angle θ and the wavelength λ of the laser light .

coefficient

$$D = \frac{k_B T}{6\pi\eta R_H} \quad (2.7)$$

to determine the hydrodynamic radius ' R_H ' of the scattering particle (here droplet). k_B is the Boltzmann's constant and the sample temperature T . The temperature dependence of the solvent viscosity η should be known.

2.4.2 Experimental set up

The Dynamic Light Scattering experiments here are carried out using an ALV controlled goniometer (ALV/SP-125) system. FIG. 2.8 shows a schematic picture of the setup. The laser passes through a collimator lens and then hits the cell with the solution. The sample cell is immersed in a thermo-stated index matching bath (toluene). The scattered light is detected by two avalanche photodiodes in pseudo cross correlation. Signal processing is done using different electronic hardware components which are described in detail below.

The whole setup consists of following components :

- 1) The incident light source, giving a coherent and monochromatic light. Here a 532 nm solid state laser of 750 mW (Coherent-Verdi 2 Watt operated maximum at 150mW on the sample) is used.
- 2) The sample cell, a cylindrical quartz glass cuvette with inner and outer diameter of 8 and 10 mm respectively.
- 3) Index matching bath (toluene) which is thermostated. Index matching helps to suppress unwanted diffraction of the incident and the scattered light. The sealed sample cell is immersed inside this bath. The temperature can be varied

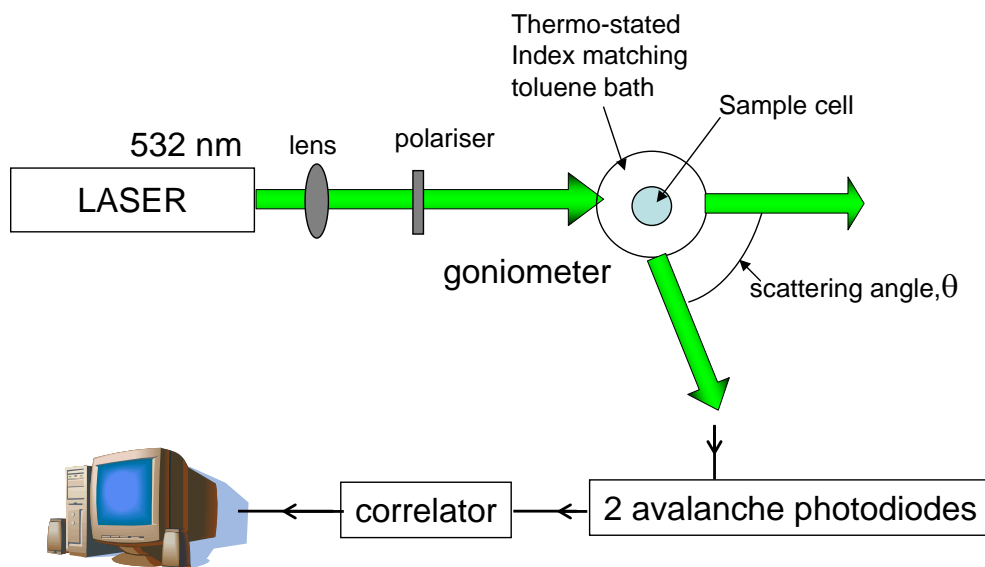


Figure 2.8: DLS setup

from -12°C to 150°C .

4) Avalanche Photo Diodes (Perkin Elmer) are used as detector which is in cross correlation. Associated optics are also mounted on the arm of the goniometer. The position of the detector is varied step-wise, with step size of 10° in an angular range of 30° to 150° .

5) The auto-correlator collects and integrates the intensity at the different delay times, τ , all in real time. The computer is also connected for the signal processing. The signal analyzer used here is an ALV digital correlator (ALV-5000/60XD digital correlator). The whole setup is mounted on an optical table to isolate it from all external vibrations.

2.4.3 Sample preparation for DLS

Microemulsion samples are filled in a special quartz cell which is cylindrical. This cell is thoroughly cleaned in an "acetone fountain" (fountain of hot freshly distilled acetone) for one hour before filling the sample. Microemulsion samples are filtered using a 200nm filter paper directly into these cells to have dust free sample. This is done in a dust free hood and the cell is sealed immediately with a

teflon tape. Microemulsion samples are sensitive to temperature so they are kept in the toluene bath for nearly 3 hours to equilibrate (1 phase samples). 2 phase samples are kept for longer duration (nearly 12 hours to 24 hours) to ensure that they reached thermodynamic equilibrium before measurement. While filtering some sample is lost due to filter paper. In case of 2-phase samples, this leads to an error and repeated measurement is required in that case to get an average good data.

2.5 Tensiometry

2.5.1 Critical Micelle Concentration (CMC)

Up to CMC the surface tension of water reduces significantly due to surfactant molecules at surface. Due to saturation, surface tension is constant above CMC. So measurement of the surface tension of the surfactant solutions is a principal method to determine the CMC.

Surface tension of a liquid is due to the cohesive interactions with neighboring molecules. In order to increase the surface area, mechanical work is required. So surface tension can be defined as the surface work dW required to increase the surface area A by dA . It can be viewed as a force exerted per unit length [mN/m]. Surfactant solutions exhibit a specific surface tension curve against concentration as shown in a schematic figure given below [FIG. 2.9].

From pure liquid up to a micellar solution the surface tension decreases linearly with the logarithm of surfactant concentration. Due to constant surface tension of the sample from CMC onwards, a kink is formed. The concentration at this kink is taken as the CMC. The measurement of surface tension (air-liquid interface) is based on force measurement. A probe is hung on a balance and brought into contact with the liquid surface. The balance experience a force, as the probe touch the liquid surface. These forces depend on many factors like the size and shape of the probe, the contact angle of the probe-liquid interaction and the surface tension of the liquid. The size and shape of the probe are easy to control. The du Noüy ring and Wilhelmy plate are mostly used probes (FIG. 2.10). We used a DCAT 11EC tensiometer from dataphysics for determining CMC. Tensiometer

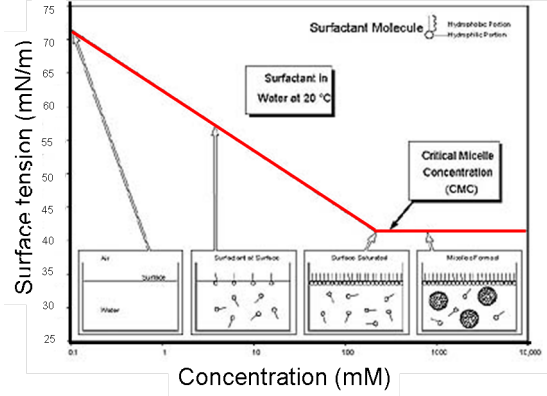


Figure 2.9: Kink formation due to micelle formation showed by the surface tension against concentration curve obtained from a tensiometer experiment.

is interfaced and works on weight based measurements.

2.5.2 Wilhelmy Plate method

Wilhelmy Plate method is used for measuring surface tension here. The thin plate is oriented perpendicular to the sample using a balance [FIG. 2.10]. The liquid sample is raised until the contact with the plate is registered. At the moment of contact, the balance experience maximum tension. Tension is calculated as,

$$\gamma_{air-water}^{wplate} = \frac{F_{max}}{L \cdot \cos \theta} \quad (2.8)$$

where $\gamma_{air-water}^{wplate}$ = surface tension, F_{max} = force acting on the balance, L = wetted length in mm and θ = contact angle. The plate is made of roughened platinum (high-energy surface) to get virtual zero contact angle. Then $\cos \theta$ has a value of approximately 1. Then only the measured force F_{max} and the wetted length of the plate need to be taken into consideration. The surfactant concentration series is generated automatically with a computer-controlled Liquid Dispensing Unit (LDU). Experiment starts with pure liquid and then an increasing concentration method is done using the LDU. For a concentrated sample, approximately 4 times CMC is used. This concentrated sample is dispensed at constant volume (0.5ml) using LDU at constant intervals. The measurements and their evaluation are carried out automatically.

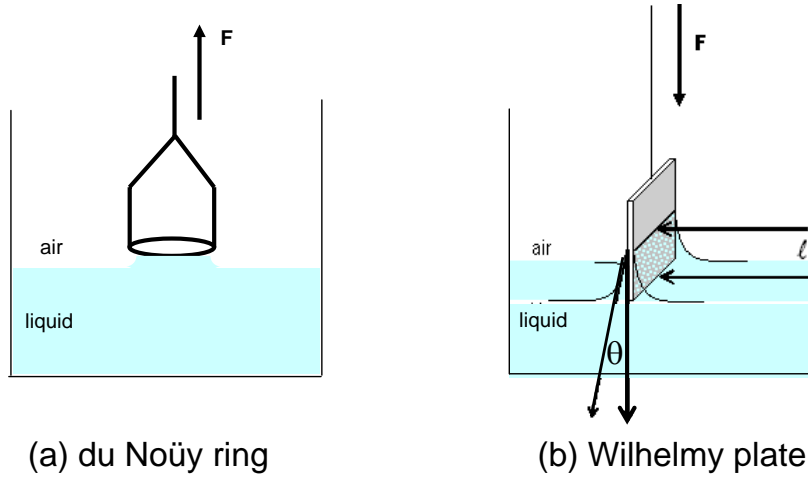


Figure 2.10: (a) Schematic diagram of du Noüy ring. The ring registers the contact with the liquid surface and is pushed through the liquid surface to a few millimeters down. Then it is pulled up until the maximum Force is reached. (b) Schematic diagram of a Wilhelmy plate during surface tension measurement. The plate is wetted by a length l and makes an angle θ with the liquid surface. A force F acts due to the contact with liquid.

2.5.3 du Noüy ring method

Another technique to measure surface tension using tensiometer is the du Noüy ring method [71] [FIG. 2.10]. Unlike the plate method, this method hardly affects the wetting properties. A du- Noüy ring is a platinum-iridium ring. This ring is attached to the balance after cleaning thoroughly with flame. Then it is lowered beneath the liquid surface.

The surface tension is measured by pulling the ring upward. The ring raises with a liquid meniscus. Maximum force required to break the ring free of the liquid meniscus is measured and this force is related to liquid's surface tension as follows.

$$\gamma_{air-water}^{ring} = \frac{F_{max}}{4\pi r} \quad (2.9)$$

where $\gamma_{air-water}^{ring}$ = surface tension; F_{max} = maximum force and r = radius of the ring. The contact angle goes to zero at maximum force. Due to the difference of the inner and outer diameter of the ring the maximum force experienced needs a

correction. Here the Harkins Jordan correction factor is used.

Chapter 3

Experimental Results and Discussions

3.1 Phase Behaviour

Phase diagrams are determined for the non-ionic microemulsions with surfactants C_8E_3 and C_4E_1 , following the procedures from the Section XV.B. Data from the optical measurement (appearance and disappearance of the turbidity) are discussed here. The averaged out values from the cooling and heating cycle is taken for water emulsification boundary (T_{WEB}) as well as for the oil emulsification boundary (T_{OEB}). Data for four different surfactant concentrations for a 1:1 water-oil microemulsion are shown in FIG. 3.1 as an example. Due to the nucleation of the droplets just before phase separation, overheating of the sample leads to a slight higher temperature for T_{WEB} on a heating cycle. A difference of 0.1K to 0.9K between cooling and heating is observed for T_{WEB} . For 60% surfactant concentration, T_{WEB} for cooling is slightly higher than the heating. This could be due to the evaporation of the water molecules at 328K which later condensed at the lid of the viol, changing the concentration of the microemulsion thereby T_{WEB} too.

ϕ_s	Temperature ramp rate	T_{WEB} (K)	
		heating	cooling
31 %	3 K/h	300.5	300.3
40 %	6 K/h	305.8	305.3
55 %	2 K/h	321.0	320.9
60 %	2 K/h	327.6	328.5

Figure 3.1: Experimental value of the T_{WEB} for 1:1 water: oil microemulsion, under cooling and heating in a water bath.

3.2 Phase behaviuor of water-decane- C_8E_3

Phase diagrams are determined for different compositions of C_8E_3 -water-decane. Microemulsion samples with fixed water to oil ratio as well as fixed surfactant volume fractions are investigated.

3.2.1 Phase Diagram of microemulsion samples of fixed water to oil ratio (fish cut)

Fish cut phase diagrams are determined for three different compositions of C_8E_3 -water-decane. The compositions studied are 1:1, 3:7 and 7:3 water-decane ratio with varying surfactant concentration.

A fish-cut phase diagram for equal water to oil (1:1) and varying surfactant concentration and temperature is given in FIG. 3.2. T_{WEB} and T_{OEB} is collected from $\phi_s = 0.15 - 0.65$ at an interval of nearly 0.05 surfactant volume fraction. The three different macroscopic phases 3Φ , 2Φ and 1Φ are observed for this concentration-temperature regime. In FIG. 3.2, each blue solid squares correspond to the T_{WEB} of a particular composition of water-oil-surfactant. At low surfactant volume fraction ($\phi_s \leq 21\%$), T_{OEB} is higher than T_{WEB} . With increasing surfactant volume fraction T_{OEB} decreases. In contrast, T_{WEB} contin-

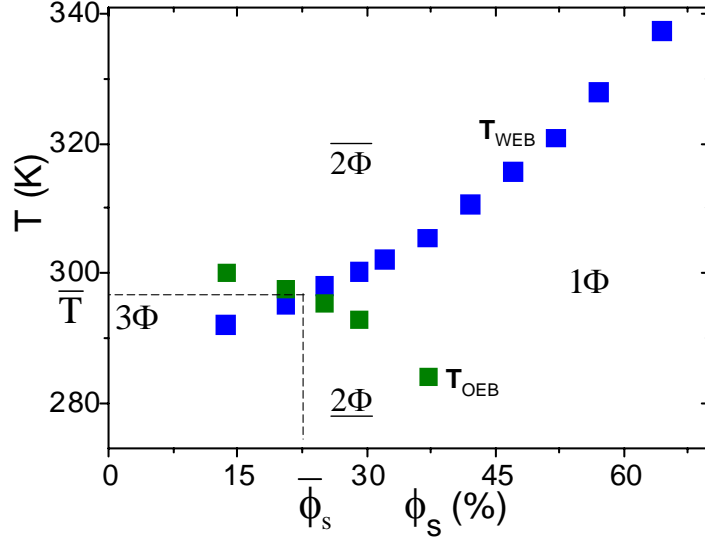


Figure 3.2: Microemulsion fish-cut phase diagram with 1:1 water-decane. Water emulsification boundary, *WEB* [blue squares] and oil emulsification boundary, *OEB* [green squares] are shown for samples with varying surfactant concentration and with increasing temperature.

ously increases with higher surfactant volume fractions. Both the emulsification phase boundaries cross each other at surfactant volume fraction $\bar{\phi}_s \approx 22\%$ and at tricritical temperature $\bar{T} \approx 297K$. Above $\bar{\phi}_s$, T_{WEB} exceeds T_{OEB} . Upto $\phi_s = 35\%$, T_{WEB} increases almost linearly. With further increase in surfactant concentration, T_{WEB} increases more steeply, whereas, T_{OEB} decreases strongly with increasing ϕ_s . Below 277K, due to the condensation of water on the glass windows of the water bath, T_{OEB} was not achievable.

The phase diagrams for the other two compositions, 3:7 and 7:3 water-decane are shown in FIG. 3.3. T_{WEB} of a 3:7 microemulsion increases almost linearly for a surfactant volume fraction range of 10% to 35% and then the increase is more sudden. T_{OEB} decreases almost linearly with ϕ_s for low surfactant volume fraction. A step decrease is observed above $\phi_s = 25\%$. T_{OEB} and T_{WEB} cross at $T \sim 300K$. In 7:3 water-decane microemulsion, the increasing T_{WEB} and decreasing T_{OEB} cross over at $T \sim 292K$. Also \bar{T} shifts. For 1:1 water-decane, \bar{T} is 297K and $\bar{\phi}_s = 0.23$; for 3:7 water-decane composition, \bar{T} is increased to 300K and $\bar{\phi}_s$ is decreased to 0.19. For 7:3 water-decane composition, $\bar{T} = 292K$ and $\bar{\phi}_s = 0.22$.

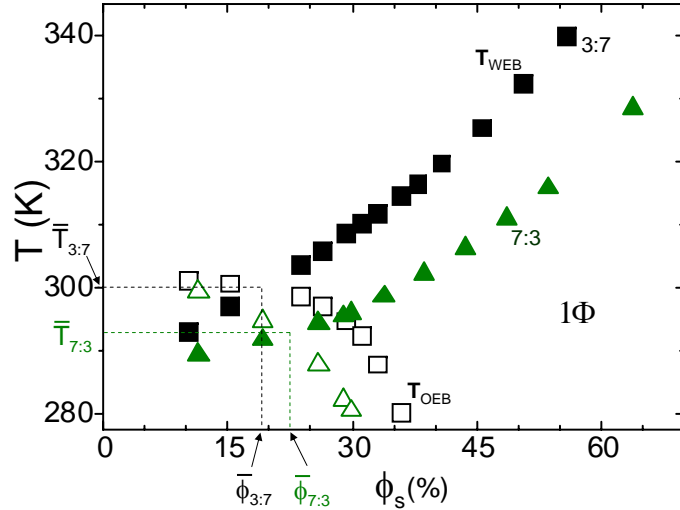


Figure 3.3: Microemulsion phase diagram with 3:7 (black squares) and 7:3 (green triangles) water-decane. T_{WEB} [solid symbols] and T_{OEB} [open symbols] are shown for microemulsion samples with increasing surfactant concentration.

The fish-cut moves upwards with decrease in water to water-oil proportion (3:7) while the emulsification temperatures decreases with an increase in the water to water-oil ratio (7:3).

3.2.2 Phase Diagram of samples with fixed Surfactant Concentration

The effect of surfactant on the microemulsion system is investigated by fixing the surfactant volume fraction and varying oil to oil + water ratios (α_o). Such a cut along the phase prism is sketched in the inset of FIG. 3.4, known as Shinoda cut [72, 73].

In FIG. 3.4, the water and oil emulsification boundaries are investigated for three different microemulsion samples with fixed surfactant volume fraction (ϕ_s) as a function of α_o . T_{WEB} is investigated for $\phi_s = 35\%$ (green solid circles in FIG. 3.4), 40% (blue solid circles) and 50% (orange solid circles). The narrow 1ϕ -region extends over the entire temperature regime and α_o . In 1ϕ -region, at low temperatures and a low oil to oil plus water ratio (α_o) the mixture takes bi-

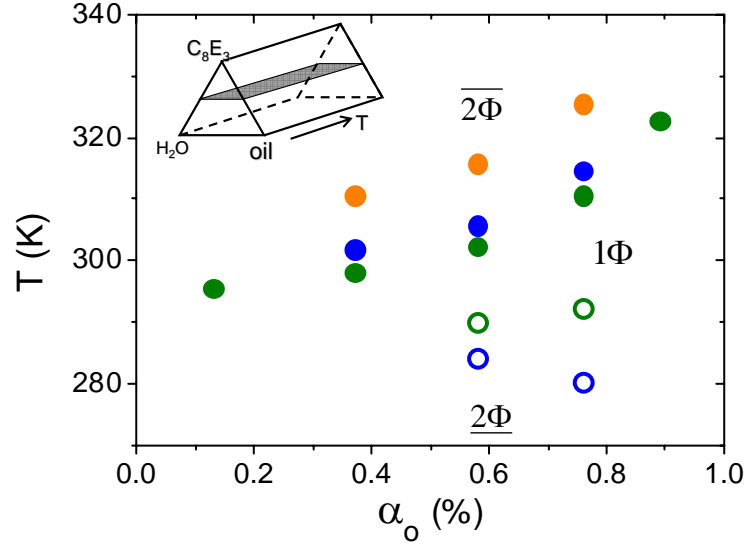


Figure 3.4: Temperature of the water emulsification (T_{WEB}) (solid circles) and oil emulsification (T_{OEB}) (open circles) boundaries for water-decane- C_8E_3 microemulsion with $\phi_s = 35\%$ (green) and varying oil to water + oil ratio; T_{WEB} and T_{OEB} for the same ingredient sample with $\phi_s = 40\%$ (blue) and varying α_o ; T_{WEB} and T_{OEB} at varying α_o for microemulsion samples with $\phi_s = 50\%$ (orange).

continuous structure while towards higher temperature it takes droplet structure (known from scattering data). The T_{WEB} increases with increasing α_o . Water emulsification boundaries of the samples show an increment with increase in surfactant volume fraction for the same α_o . For $\alpha_o = 38\%$, the three data belongs to $\phi_s = 35\%$, 40% and 50% . Among three of the compositions, for fixed α_o , $\phi_s = 35\%$ has lowest and 50% has highest T_{WEB} . With increase in surfactant concentration, the microstructure of the sample gets smaller and more stable, which leads to a higher emulsification temperature. Oil emulsification boundaries appear at lower temperatures for the three different concentration investigated here. T_{OEB} decreased with increasing surfactant concentration. Oil emulsification boundary for $\phi_s = 40\%$ showed a decrease with increase in α_o .

3.3 Experimental Results : DSC of water-decane- C_8E_3

The specific heat change of the microemulsion during phase transition across WEB (1Φ region to $\overline{2\Phi}$ region) and OEB (1Φ region to $\underline{2\Phi}$ region) is examined (FIG. 3.5). Each sample is scanned with different scan rates from 2 K/h to 15 K/h. Data values are determined within the experimental accuracy.

An upscanning or downscanning of the microemulsion sample from the 1Φ - $\overline{2\Phi}$ or 1Φ - $\underline{2\Phi}$ regions leads to a step in the specific heat at the emulsification failure point [FIG. 3.5]. The variation of the specific heat relative to the baseline obtained during an upscanning of a 1:1 water to decane microemulsion with 31% surfactant volume fraction is shown in FIG. 3.5(b) [right]. The specific heat step that occurs at $T \sim 27.1^\circ C$ (this T is represented as T_{WEB}) is followed by oscillations with gradual decrease in amplitude [FIG. 3.5(b) right]. The oscillations are caused by repeated nucleation, coarsening and sedimentation of droplets. The height of the first step is mentioned as 'full height' later. The dotted lines shows the average height (or mean height) of the oscillations. The difference of the height of the dotted line with the baseline gives ΔC_v^{step} . Thermograms are obtained at different scan rate of 2 K/h, 5 K/h and 10 K/h. The phase transition temperature varies only upto $0.2^\circ C$ for scan rates between 2 K/h and 20 K/h. Another example is the phase transition temperature T_{WEB} of 3:7 water-decane microemulsion with 40% surfactant concentration, $41.2^\circ C$ (at 1 K/h) and $41.3^\circ C$ (at 10 K/h). Such a small variation in the phase transition temperature is negligible for the analysis of the calorimetric studies in the range of heating rates here. Mean height of the signals had higher accuracy within the experimental accuracy. Data obtained for a microemulsion sample with equal water to oil ratio and 31% surfactant volume fraction are shown in FIG. 3.6 which is obtained from FIG. 3.5. The independency of the height of the specific heat-step on the scan rate is shown.

The reproducibility of the variation of the specific heat with temperature is checked by running the DSC of two microemulsion samples of 1:1 water-decane microemulsion with 35% of surfactant volume fraction FIG. 3.7. The first DSC run gave $T_{WEB} = 29.2^\circ C$ with a step height $\Delta C_v^{step} = 9.3 \times 10^{-3} cal/^\circ C$. Performing a second run after exchanging sample material, gave $T_{WEB} = 29.1^\circ C$

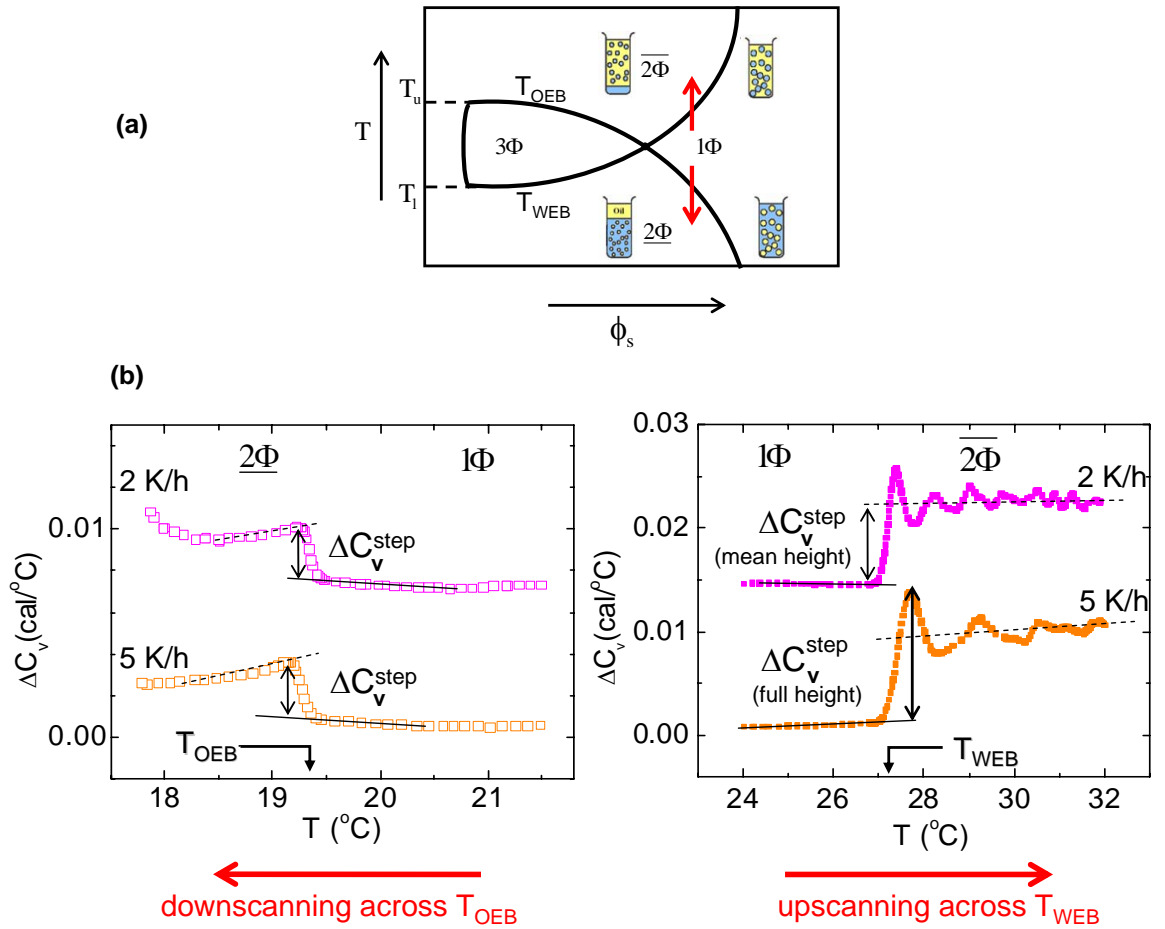


Figure 3.5: (a) The schematic fish cut phase diagram with the temperature line (red color arrows) along which calorimetry is done. Red arrows show the direction and the temperature intervals investigated by calorimetry. A sketch of 1Φ microemulsions (water droplets in oil or oil droplets in water) to the *overline*– 2Φ or *underline*– 2Φ microemulsion (microemulsion with water or oil droplets coexisting with expelled water or oil) is shown. (b) A step in the specific heat signal (solid squares) when passing T_{WEB} during an upscanning from 1Φ region to the *overline*– 2Φ region (right). Data taken at a scan speed of 2 K/h (pink) and 5 K/h (yellow) are shown. The average height of the step is given by the arrows. Solid lines denote the baseline in the 1Φ region and the dashed lines shows the baseline in the 2Φ region. While downscanning, the specific heat shows a step when passing the oil emulsification boundary (left Fig. with open squares). The data plot at 2K/h is shifted along the y-axis in both figures for better eye guidance.

Up / down scan rate	T_{WEB} (°C)	ΔC_v^{STEP} (cal/ °C) [1Φ to $2\bar{\Phi}$]	T_{OEB} (°C)	ΔC_v^{STEP} (cal/ °C) [1Φ to 2Φ]
2 °C/h	27.0	0.007	19.4	0.002
5 °C/h	27.1	0.008	19.4	0.002

Figure 3.6: Analysed DSC data for microemulsions with 1:1 water : oil and 31% of surfactant volume fraction. ΔC_v^{step} while crossing WEB and OEB, at two different scan rates, hardly depend on scan rate within experimental accuracy. T_{WEB} and T_{OEB} are also recorded.

with a step height $\Delta C_v^{step} = 9.7 \times 10^{-3} cal/^\circ C$. Fresh samples were used for both the runs. Note that ΔC_v^{step} is reproducible within very high accuracy.

The variation of the height of the step with ϕ_s is shown in FIG. 3.8, FIG. 3.9 and FIG. 3.10 for the three different ratios of water to oil. Height of the full step (solid symbol) and the mean height (open symbol) are recorded. Eventhough the absolute values are different for full step height and mean height, the trend of the specific heat steps are the same for both sets of data.

For 1:1 water-decane ratio (FIG. 3.8), the phase transition temperatures T_{WEB} increases from 300K to 326K if surfactant concentration (ϕ_s) increases from 31% to 60%. With increasing T_{WEB} , an increase in the step height is observed upto $T_{WEB} \sim 326K$ [FIG. 3.8]. The last three data points shows almost the same height.

For 3:7 water-decane ratio, initially ΔC_v^{step} increases with increasing T_{WEB} [FIG. 3.9] and passes a maximum value at $T_{WEB} \sim 320K$. This indicates that with increasing surfactant concentration, the step height increases and drops after reaching a maximum value. The temperature $T_{WEB} \sim 320K$ could be of interest in further studies in understanding the mechanism of the system. [how to relate this non-monotonic trend of steps in specific heat with the phase transition in the microemulsion which is not visible in the phase diagram]. For bigger domain

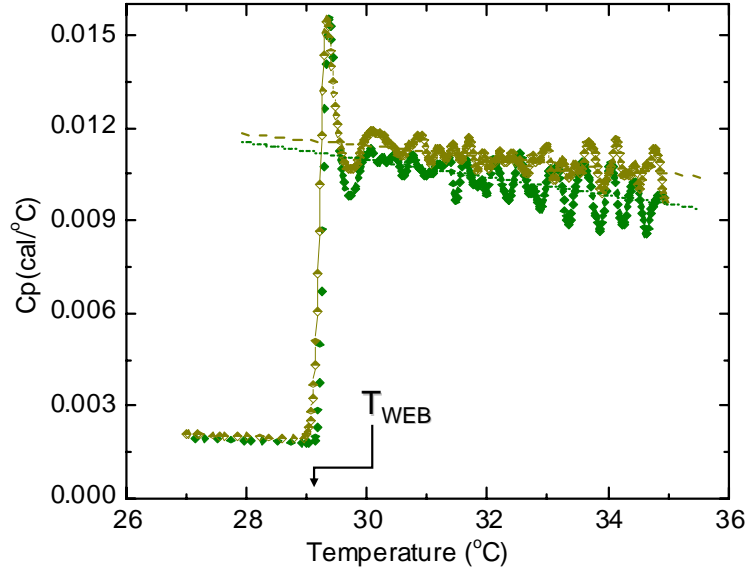


Figure 3.7: DSC data for microemulsion sample with 1:1 water:oil and 35% of surfactant volume fraction. Experiments are done at 1.4 K/h. ΔC_v^{step} while crossing WEB is obtained with an accuracy of 0.01 cal/ $^{\circ}$ C. The T_{WEB} showed a reproducibility with an accuracy of 0.1 $^{\circ}$ C. The mean height of the step is shown by dotted and dashed lines.

sizes as well as for small domain sizes, the step height is less than that for the intermediate ones. The effect of the changed solubility of surfactant in the water and decane may also effect the step height at high temperatures. The max.step height ΔC_v^{step} of 3:7 water-oil ratio microemulsion is reduced by nearly 1 $mcal/^{\circ}C$ compared to the maximal step height of 1:1 water-oil ratio microemulsion.

The third sample, 7:3 water-decane microemulsion also showed an increase of ΔC_v^{step} with increasing surfactant concentration [FIG. 3.10]. The data points correspond to ϕ_s from 35% to 55%. For this sample, ΔC_v^{step} increases monotonically with surfactant concentration.

All data sets from the three different compositions of water-decane- C_8E_3 sample are fitted to a polynomial fit of third order for better eye guidance [FIG. 3.11].

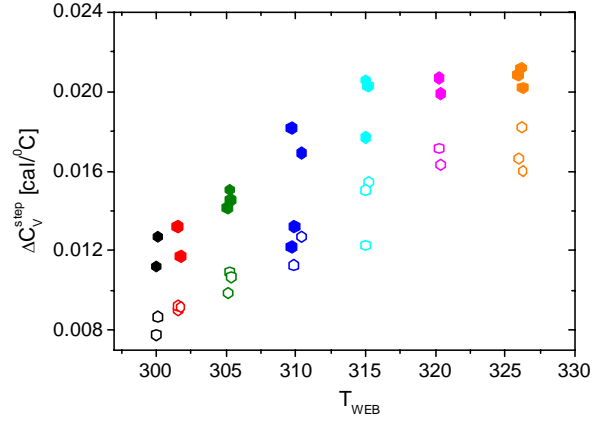


Figure 3.8: Dependence of ΔC_v^{step} on phase transition temperature T_{WEB} for 1:1 water-decane microemulsion samples with varying surfactant concentrations. Solid symbols shows the full height of ΔC_v^{step} while open symbol shows the mean height of ΔC_v^{step} . Different colors correspond to different surfactant concentrations (ϕ_s). The various symbols for one T_{WEB} are the data taken at various scan rate ranging between 2 K/h to 15 K/h.

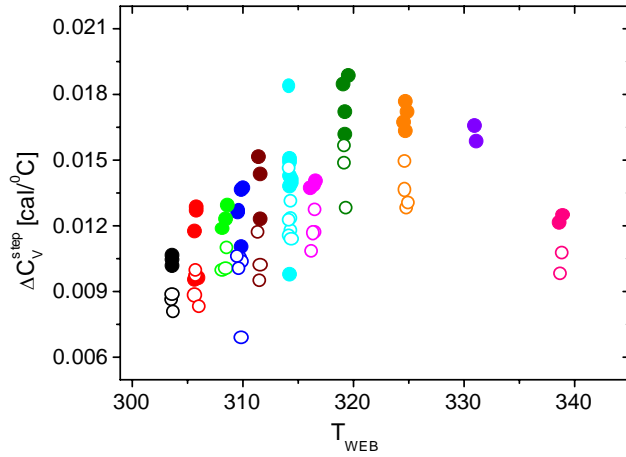


Figure 3.9: Dependence of ΔC_v^{step} on phase transition temperature T_{WEB} for sample with 3:7 water-to-oil ratio and varying surfactant concentration. Different data points for the same T_{WEB} denote the scattering of the data at varying scan rates between 2K/h to 15 K/h. Solid symbols show the full height of ΔC_v^{step} while open symbol shows the mean height of ΔC_v^{step} .

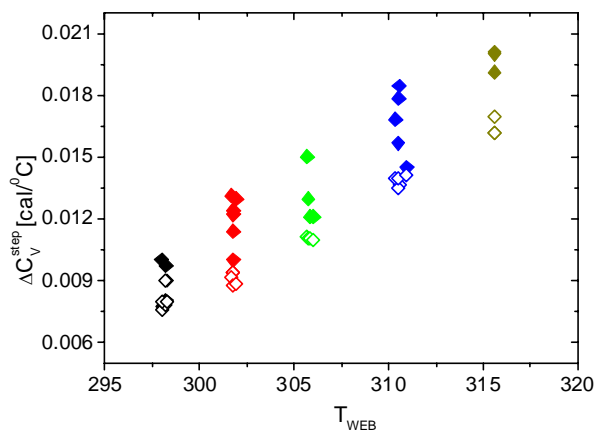


Figure 3.10: Dependence of ΔC_v^{step} on phase transition temperature T_{WEB} for sample with 7:3 water-decane ratio and varying surfactant concentration ranging between 35% and 55% (different colored diamonds). Solid symbols show the full height of the step in the specific heat ΔC_v^{step} , while open symbols show the mean height of the step. The data at different scan rates on the same sample are shown by the same colored symbols.

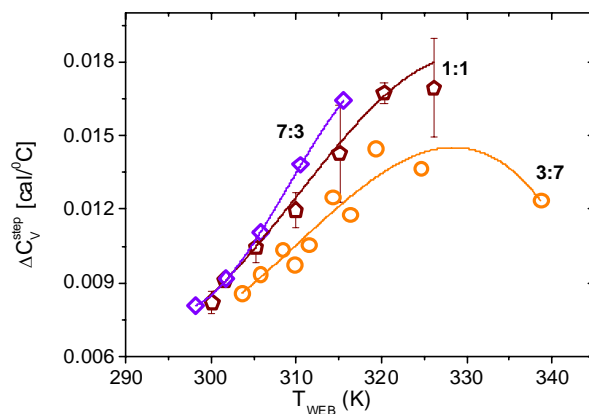


Figure 3.11: Mean height of the specific heat-step with increasing temperature for water emulsification boundaries. The data correspond to three different compositions : 7:3 water-decane (purple diamond), 1:1 water-decane (wine pentagons) and 3:7 water-decane microemulsion (orange circles). A third order polynomial fit is given for a better eye guidance.

3.3.1 Comparison of the phase transition temperature determined from turbidity measurements and DSC

The following table shows the water emulsification boundary (T_{WEB}) of 1:1 water to oil ratio microemulsion, determined from turbidity measurements and calorimetry. The phase transition temperatures obtained from these two experimental methods showed a difference of less than 1 K except for a higher surfactant volume fraction 0.6. Evaporation of water or decane inside the vial, at higher temperature might contribute to this temperature difference. The T_{WEB}

ϕ_s (C ₈ E ₃)	T_{WEB} (K)		
	Visual (water-bath)	DSC	ΔT
0.31	300.31	300.08	0.23
0.35	302.21	301.61	0.60
0.4	305.53	305.24	0.29
0.45	310.72	309.92	0.80
0.5	315.78	315.07	0.71
0.55	320.99	320.31	0.68
0.6	327.99	326.13	1.86

Figure 3.12: Difference in the phase transition temperature obtained from visual inspection (scattering) in water bath and microcalorimetry (DSC) for microemulsion sample with equal water to oil ratio. The scan rate is added in brackets.

determined from the turbidity measurement (in thermo stated water bath) always slightly exceed the values obtained from calorimetry. The calibration of the calorimeter might cause this systematic variation.

3.4 Experiment Results of DLS

The average domain size of microemulsion samples is measured by dynamic light scattering. Samples at 1Φ , 2Φ or 3Φ regions are chosen [FIG. 3.14]. Initially, the refractive index of the microemulsion samples as a function of composition and temperature is determined which enters the analysis of the DLS data later.

$\phi_s \backslash T(^{\circ}\text{C})$	11°C	14°C	24°C	37°C
14 %	1.377		1.394	1.406
22 %		1.389	1.397	1.406
27 %		1.397	1.397	1.406
40 %			1.405	

Figure 3.13: Refractive index of the microemulsion samples with different surfactant concentrations at different temperatures.

The average domain size is measured for temperatures from 14°C to 37°C [cross marks in FIG. 3.14]. The temperature dependence of the size of the oil/water domains are shown in [FIG. 3.15]. The left most column lists ϕ_s for a 1:1 water-decane microemulsion.

The domain size in a two phase region depends on temperature and in the one phase region on surfactant concentration [Section X]. In the 1Φ region, the average domain size for C_8E_3 -water-decane microemulsion with $\phi_s = 27\%$ is $R_w^{1\Phi} = 7.3$ nm. After crossing T_{WEB} , the droplets shrink by expelling excess water. Hence, at 32°C and 37°C the domain size decreased to 6.5 nm and 5.6 nm respectively. Below T_{OEB} , the size of the oil domain decreased to 3.3 nm at 14°C . A similar trend can be seen for the other two sets of sample. Note, near to the tricritical point, the morphology of microemulsions is not spherical but bicontinuous. However, in data analysis a spherical morphology is assumed. Still, the measured data reflect the typical length scale of the underlying morphology.

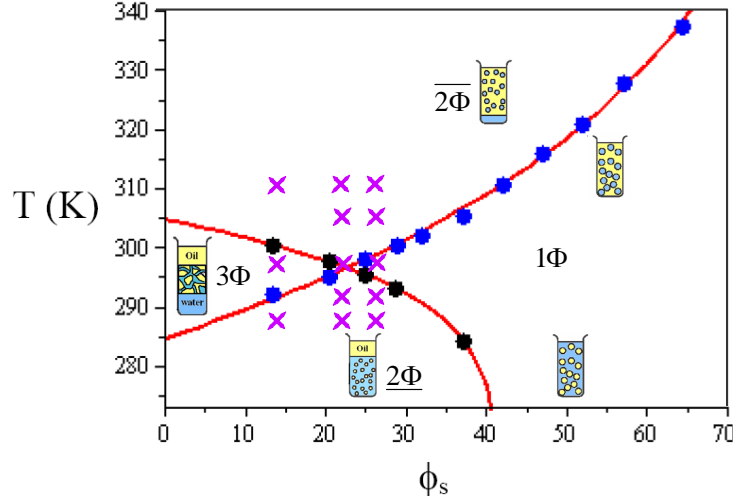


Figure 3.14: Fish cut phase diagram of a 1:1 water-decane microemulsion as a function of ϕ_s . T_{WEB} and T_{OEB} are shown by the blue and black circles respectively. The temperatures at which samples are investigated by DLS are marked by pink crosses. The macroscopic appearance of the microemulsion is sketched too.

3.4.1 Calculated versus measured domain size

The simplified domain size is assumed to be spherical. In that case the size of the droplets can be calculated using Eq.1.15 and Eq.1.16. These calculated values are compared with the experimental data [FIG. 3.16]. As mentioned, the morphology of the microemulsion is bicontinuous at $24^{\circ}C$ (tricritical point) for this composition. We can see that even with a wrong morphological assumption, the calculated domain size matches with the experimental data with a mismatch of approximately 2 nm. DLS measures hydrodynamic radius (R_h), slightly larger than the calculated radius. This is in agreement with my data. The domain size could not be calculated for 14% of surfactant concentration because the sample was in 3Φ - region, i.e the amount of water and oil in the microemulsion phase are unknown.

ϕ_s \ T (°C)	14°C (2Φ)	17°C (2Φ)	24°C ($1\Phi/3\Phi$)	32°C (2Φ)	37°C (2Φ)
	R (nm)				
14 %	7.5		8.3		5.8
22 %	3.4	5.1	8.3	6.4	4.1
27 %	3.3	5.1	7.3	6.5	5.6

Figure 3.15: Hydrodynamic radius of oil/water domains obtained from DLS. Microemulsion samples with 1:1 water-decane and three different surfactant concentrations are used.

ϕ_s	calculated R (nm)	measured domain size (nm)
14%		8.3 (3ϕ)
22%	6.6	8.3
27%	5.4	7.3

Figure 3.16: Calculated and the experimental data (DLS) of the domain sizes of 1:1 water-decane microemulsion sample with varying surfactant concentration at 24°C. Results are presented in nanometers.

3.5 Results from Tensiometry

Tensiometry is done for determining the critical micelle concentration for the non-ionic surfactant C_8E_3 , using the Wilhelmy Plate method [FIG. 3.17]. A solution with a concentration of 4 times CMC is dispensed into Milli Q water at regular intervals. The surface tension of water decreases with increasing surfactant concentration. Initially, the surface tension decreases rapidly from a higher value to 38 mN/m. Further increase in the surfactant concentration leads to a kink [FIG. 3.17 inset] at 7.5 mM. Afterwards the surface tension is almost constant. This concentration (7.5 mM) is the CMC of the sample. This value is comparable with the available data of CMC of this particular surfactant [6]. The ring method was also used for comparison. Although the shape of the curve is identical, the CMC was higher by 1.8 mM [FIG. 3.18]. The CMC obtained using the ring geometry was 9.3 mM. This difference in the CMC may be due to the high sensitivity of the ring geometry regarding clean initial conditions.

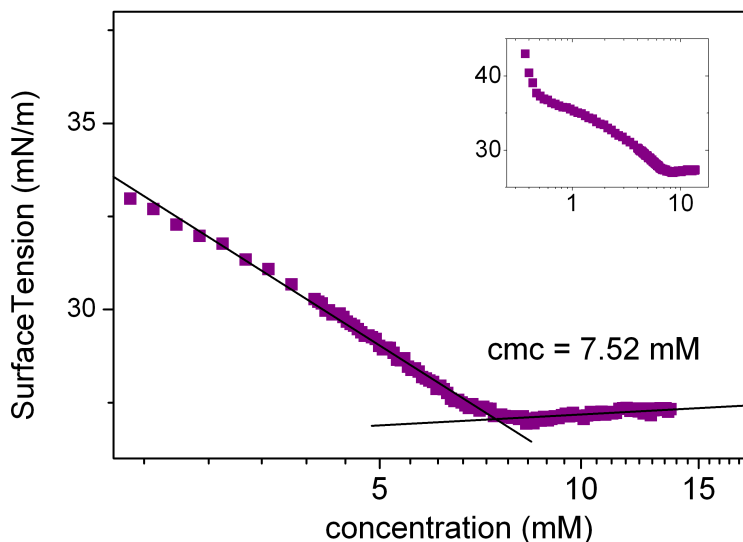


Figure 3.17: The concentration dependence of the surface tension of a C_8E_3 solution at $20.4^\circ C$ obtained using a Wilhelmy plate. The complete data set is shown in the inset.

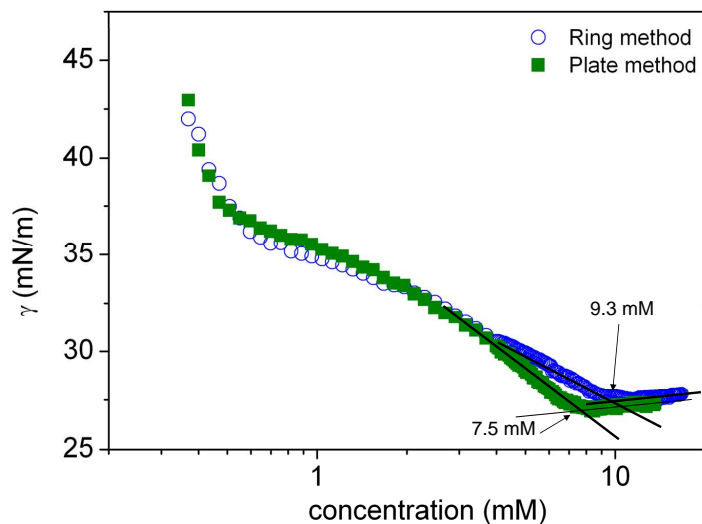


Figure 3.18: Measurement of dependence of the surface tension on surfactant concentration using a Wilhelmy plate (solid squares) and a ring geometry (open circles). The surfactant solutions with an initial concentrations of 4 times CMC was dispensed to pure water.

In FIG. 3.19, the initial concentrated surfactant used for dispensing into clean water differs. First set of data is collected using C_8E_3 dispensed in water with a surfactant concentration of 5 times the CMC (green up triangles). Data from the surfactant solution with 4 times CMC (purple triangles) overlap with the first data giving the same CMC for C_8E_3 . The reproducible values from our own experiments [FIG. 3.19] using samples of different concentrations and the comparable values from the literature show the robustness of the plate method. Hence all the tensiometric experiments performed here are obtained with the Wilhelmy plate method.

The CMC of 7.5 mM for the non-ionic surfactant C_8E_3 , is equivalent to 0.2% surfactant volume fraction in equal water-decane ratio. The 3Φ region starts [approx.] from this concentration [FIG. 3.20].

The CMC of surfactant in alkane is also of interest in my studies. Due to the increased solubility of surfactant in alkane, the surfactant shows a lower interface activity. Along with the low surface tension of alkane, even adding a solution with much higher surfactant concentration hardly changes the values for the surface

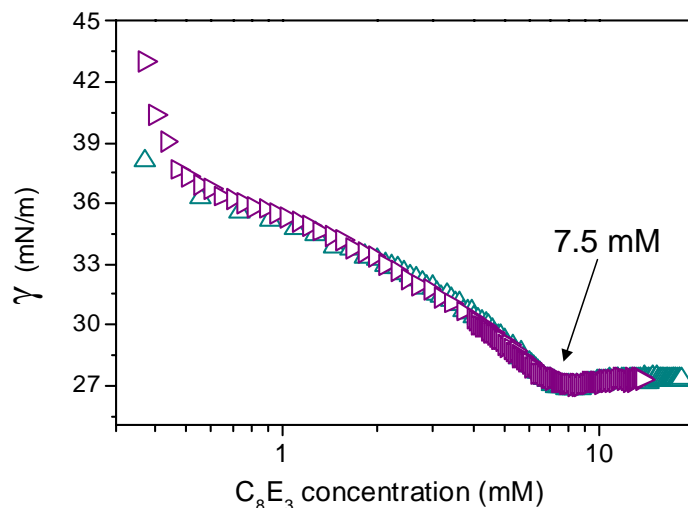


Figure 3.19: Concentration dependence of the surface tension of a C_8E_3 solution at $20.5^\circ C$ measured using a Wilhelmy plate. A solution of 5 times CMC (green up triangles) and 4 times CMC (purple right triangles) are dispensed to pure water, respectively.

tension [open stars in FIG. 3.21].

Within experimental accuracy, the CMC of the surfactant in water at 6 different temperatures linearly declined up to $T = 50^\circ C$ [FIG. 3.22]. After that the CMC slightly increases. Evaporation of water effect of these CMC values at high temperatures as each data point needs about 1h measurement time. Eventhough the experiment is performed in a closed chamber, the evaporation of water from the vessel could not be controlled. The sample vessel was open throughout the experiment and the water droplets condensed on the chamber walls within one hour of the experiment. This evaporation might have led to an increase of the surfactant concentration of the solution, resulting in causing a saturation of the surfactant molecules at the interface much earlier.

The solubility of non-ionic surfactants is determined by the hydrogen bonds formed between the oxygen atom of the ethylene oxide chains and the water molecules. Increase in temperature causes breakage of these hydrogen bonds resulting in a dehydration of the hydrophilic groups. This favors micellization. The decrease in CMC with temperature as seen in FIG. 3.22 is due to this effect. But an opposite effect, i.e. disruption of the structured water at higher temperature

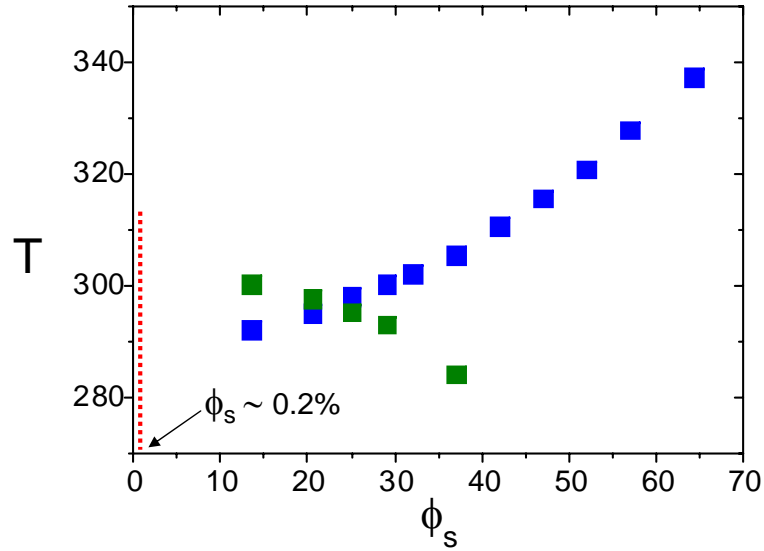


Figure 3.20: Appearance of 3 Φ region (red dotted line) according to the CMC of C_8E_3 in water. The experimental data for the emulsification boundaries [T_{WEB} [green squares] and T_{OEB} [blue squares]] for 1:1 water to oil ratio microemulsion with varying surfactant concentration.

can disfavor micellization [11]. A minimum in the CMC-temperature curve is due to domination of this effect over micellization. Experiments on strong surfactant $C_{12}E_5$ showed a similar trend as in [FIG. 3.22] [10].

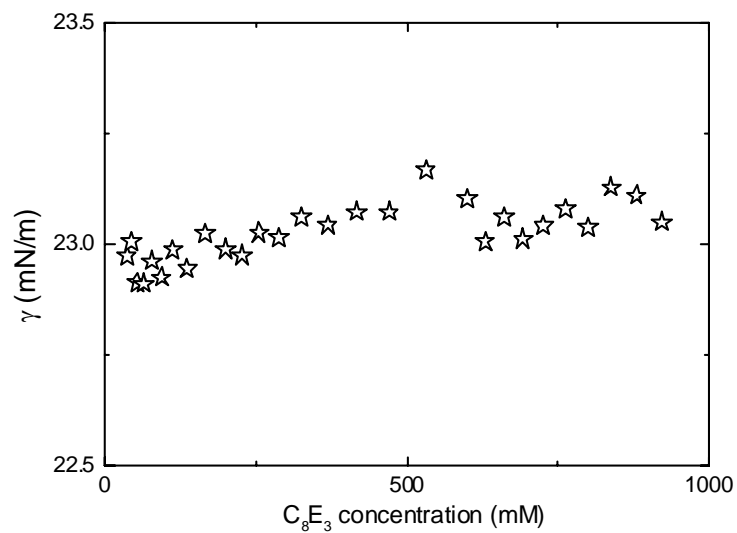


Figure 3.21: Tensiometric data of the concentration dependent surface tension of C_8E_3 in decane.

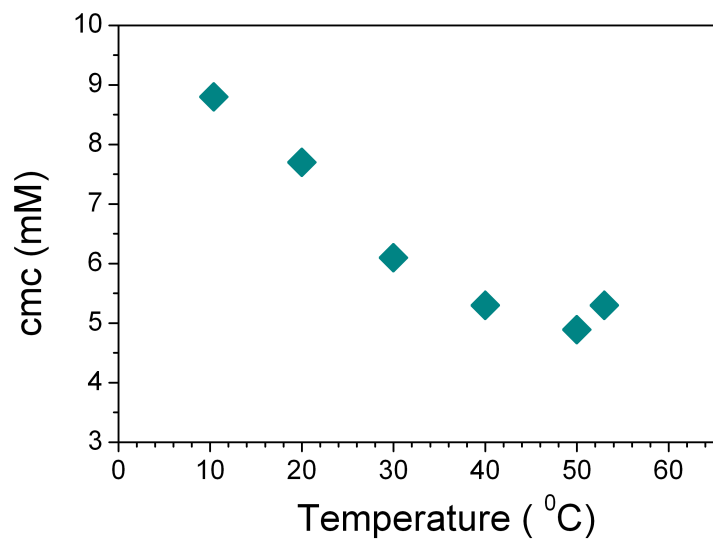


Figure 3.22: Variation of the critical micelle concentration (CMC) of C_8E_3 in water with increase in temperature. A linear decline upto 50°C is observed.

3.6 Validating the predictions to the phase boundaries

In this section, the experimental data for the water and oil emulsification phase boundaries are examined to investigate the predictions of the phase boundary.

3.6.1 Fitting and the Material Parameters: R_w^{mic} , T_l , a_w , R_o^{mic} , T_u and a_o

The material parameters are quantified by fitting the experimental data [FIG. 3.2, 3.3] with the modified equations Eq.1.31 and Eq.1.32 for T_{WEB} and T_{OEB} ;

$$T_{WEB} = T_l - \frac{1}{a_w} \ln \left(1 - \frac{R_w^{mic}}{3l_s} \frac{\phi_s}{\phi_w + x\phi_s} \right) \quad (3.1)$$

$$T_{OEB} = T_u + \frac{1}{a_o} \ln \left(1 - \frac{|R_o^{mic}|}{3l_s} \frac{\phi_s}{\phi_o + (1-x)\phi_s} \right) \quad (3.2)$$

and the values of the material parameters, R_w^{mic} , T_l , a_w , R_o^{mic} , T_u and a_o , are later compared with that of the microemulsions of different composition.

The surfactant concentrations are corrected for the CMC of C_8E_3 in water and decane. i.e. only the surfactant concentrations above the CMC are considered for determining the morphology of the surfactant monolayer. The CMC of C_8E_3 in water is 7.5 mM at 25⁰C which corresponds to a volume fraction of 0.2%. The temperature dependence of the CMC is neglected in the recalculation of ϕ_s . The surfactant showed a high miscibility in decane. From the the lowest surfactant concentration where a 3 Φ -region of water-decane- C_8E_3 [Kahlweit et al.] showed up, the corrected value for the CMC in decane is estimated. Thus we approximated the CMC in decane as $0.02 \times \phi_o$,

$$\phi_s^{new} = (\phi_s - 0.002 \times \phi_w - 0.02 \times \phi_o) \quad (3.3)$$

Then,

$$T_{WEB} = T_l - \frac{1}{a_w} \ln \left(1 - \frac{R_w^{mic}}{3l_s} \frac{\phi_s^{new}}{\phi_w + x\phi_s^{new}} \right) \quad (3.4)$$

$$T_{WEB} = T_u + \frac{1}{a_o} \ln \left(1 - \frac{R_o^{mic}}{3l_s} \frac{\phi_s^{new}}{\phi_w + (1-x)\phi_s^{new}} \right) \quad (3.5)$$

3.6.2 Interfacial surfactant after the CMC correction

Including the CMC of the surfactant in water and decane in Eq.3.4 we estimated the interfacial active surfactant. This corrected value for the surfactant volume fraction has been used in further studies. Despite the high solubility of C_8E_3 in decane, the interfacial active surfactant is only just below the total surfactant concentration. This is due to the high surfactant concentration, i.e. low volume fraction of decane.

ϕ_s (total surf.)	ϕ_s^{new} (interfacial)
0.13	0.12
0.21	0.19
0.24	0.23
0.32	0.31
0.42	0.41
0.52	0.51
0.64	0.63

Figure 3.23: Table showing the actual volume fraction of the surfactant in the sample and the interfacial active surfactant obtained using the equation 3.3 for equal volume fraction of water and decane.

3.6.3 Microemulsion with equal proportion of water and decane (1:1)

The experimental data for T_{WEB} and T_{OEB} for C_8E_3 -water-decane microemulsion with equal proportions of water and decane is shown in FIG. 3.24. T_{WEB} of the sample investigated between $\phi_s = 0.15$ to 0.65 increases with increasing

surfactant volume fraction, whereas T_{OEB} decreases with increasing ϕ_s . The least square fits (red lines along the data points) of the experimental data for T_{WEB} and T_{OEB} according to the modified equations Eq.3.4, Eq.3.5 is also shown in FIG. 3.24. The three phase region is clearly visible above the CMC of the surfactant, which helps to determine the boundary of the three phase region. Here the three phase region starts from surfactant volume fraction of 0.002 (dashed line near to temperature axis). This determines the lowest surfactant concentration for finding a bicontinuous microemulsion. The values for the material parameters

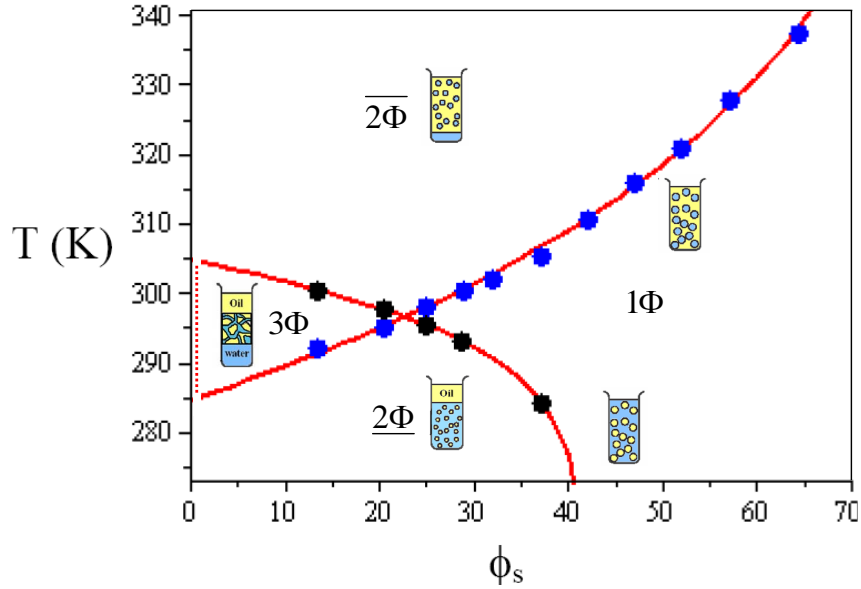


Figure 3.24: The least square fitting (red line) of the emulsification boundary data for 1:1 water to oil ratio microemulsion, according to the modified equation. Water emulsification boundary, T_{WEB} [solid blue circles] and oil emulsification boundary, T_{OEB} [solid black circles] are shown for the microemulsion samples with varying surfactant concentration.

determining the temperature dependent phase boundaries T_{WEB} and T_{OEB} for a 1:1 oil : water microemulsion are listed in the table in FIG. 3.25 (first row). The parameter value obtained, show a reverse micellar radius ($R_w^{mic} = 1.7$ nm) which is almost one third of the micellar radius ($R_o^{mic} = 3.9$ nm). This is in contrast to some previous results showing $R_w^{mic} \sim R_o^{mic}$ [35]. This may be due to the strong dehydration of the reverse micelles at high temperature and the existence of some

oil in the micelles due to the high solubility of the surfactant in oil. The change of a swollen micelle to a micelle or reverse micelle is quantified using the material parameter a_o and a_w . The meaning of a_o and a_w will be discussed in detail in later sections.

water : decane	R_w^{mic} (nm)	T_l (K)	a_w (K ⁻¹)	R_o^{mic} (nm)	T_u (K)	a_o (K ⁻¹)
1 : 1	1.7	285	0.026	3.4	304	0.10
3 : 7	1.8	286	0.029	5.1	304	0.15
7 : 3	1.9	284	0.028	3.0	306	0.07

Figure 3.25: Values for the parameters from the fitting of the emulsification boundary data for 1:1, 3:7 and 7:3 water to oil ratio microemulsion according to the modified Helfrich equation. Fitting of T_{WEB} yielded R_w^{mic} , T_l and a_w . The effective length of the surfactant is kept fixed, $l_s = 1$ nm. Fitting of the oil emulsification boundary, T_{OEB} gave R_o^{mic} , T_u and a_o .

3.6.4 Microemulsion with 3:7 and 7:3 water to decane ratio

The trend of the phase boundaries with increasing temperature for 3:7 and 7:3 water to decane microemulsions are the same as in the previous sample. A change in the water to decane ratio changed the location of the tricritical point (\bar{T}). For the 3:7 composition, we can see that for $\phi_s > 36\%$, all the oil is emulsified for temperature above the freezing point of water. Whereas, at higher temperatures water still gets expelled out. For the 7:3 composition, at $\phi_s > 32\%$ all the oil is emulsified while water still expelles out at higher temperatures. The experimental data for T_{WEB} and T_{OEB} of 3:7 and 7:3 water- oil microemulsions are fitted using the modified equations Eq.3.4, Eq.3.5. The values of the material parameters obtained from the fit are given in the last two rows of FIG. 3.25.

From the table [FIG. 3.25] we can see that the values of the material param-

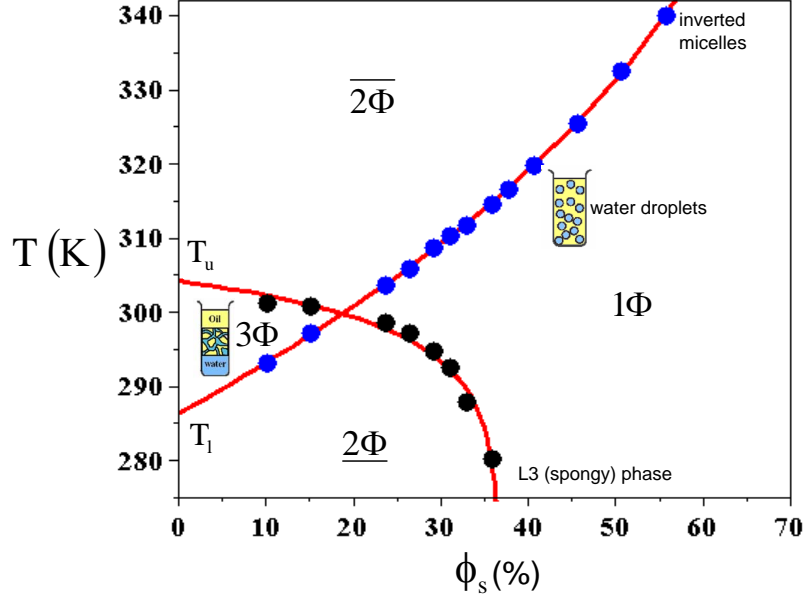


Figure 3.26: Fits of the emulsification boundaries for microemulsion with a 3:7 water to oil ratio according to the modified equation. Water emulsification boundary, T_{WEB} [solid blue circles] and oil emulsification boundary, T_{OEB} [solid black circles] are shown for the microemulsion samples with varying surfactant concentration. The red lines show the fits.

eters obtained from the least square fit of T_{WEB} [Eq.3.4] are comparable for the three investigated compositions. A slight increase of the inverse micellar radius (R_w^{mic}) from 1.7 nm to 1.9 nm is observed for microemulsion with a 7:3 water to oil ratio. It may be due to the higher solvation of the inverse micelles. Even at high temperature, water molecules may be enclosed in the inverse micelle. A detailed study on the solubility of C_8E_3 in water at higher temperatures may give a better understanding of the scenario. The value of the temperature at which the 3Φ region appears (T_l) is consistent for all three compositions. Within experimental accuracy, $T_l = 284 \text{ K} - 286 \text{ K}$ agrees well with the available data ($T_l = 289 \text{ K}$) from previous works [29, 74, 75]. This difference could be due to the purity of C_8E_3 , which slightly differs between various batches and different companies. The parameter a_w yields almost the same value $a_w \sim 0.03 \text{ K}^{-1}$ for the three different water to oil ratio microemulsions. This hints that the process determining the value of a_w does not depend on the composition but is generic

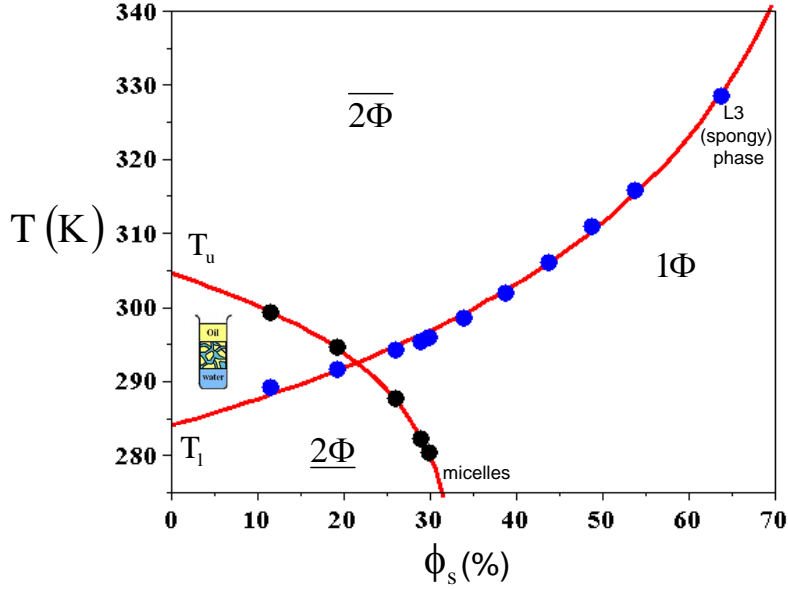


Figure 3.27: Fitting of the emulsification boundary data for 7:3 water to oil ratio microemulsion according to the modified equation. Water emulsification boundary, T_{WEB} [solid blue circles] and oil emulsification boundary, T_{OEB} [solid black circles] are shown for the microemulsion samples with varying surfactant concentration. The red line shows the fitting

for C_8E_3 -water-decane ternary microemulsions.

The values of the parameters from the least square fit of T_{OEB} , are less consistent. The micellar radius (R_o^{mic}) for water to oil ratios of 1:1 and 7:3 are comparable, $R_o \sim 3$ nm. But an increase of the micellar radius to $R_o \sim 5$ nm is obtained for 3:7 water to oil ratios. Here it needs to be considered that the proportion of oil exceeds those of water, whereas the average curvature of surfactant monolayer is directed towards oil. Hence, the microstructure cannot be spherical but is bicontinuous, i.e. a L3 (sponge)-phase forms. But according to the assumptions, it should not affect the micellar size at low temperature. A systematic study of the solubility of the non-ionic surfactant C_8E_3 in decane is required for a better understanding. The highest temperature where the 3Φ region appears is consistent ($T_u = 304K - 306K$) for all three compositions. Within experimental accuracy, this value is in accordance with the available data for T_u which is 302 K [29, 74, 75]. The parameter a_o is close to $a_o \sim 0.1K^{-1}$ for the

three investigated ratios of water to oil. Again, a_o is slightly higher for water to oil ratios of 3:7. Similar to a_w , the consistency in the value of a_o , points towards a generic process that does not depend on the ratio of water to oil in microemulsions.

As already mentioned, the morphology of the microemulsion at the emulsification boundaries depends on composition. The underlying morphology can be bicontinuous, sponge-like, cylindrical and spherical. Close to tricritical point \bar{T} , the distribution of water and oil will be similar on either side of the surfactant monolayer in a bicontinuous morphology. However, in the derivation of the modified equation it is assumed that the surfactant monolayer is spherical. Amazingly, even with the wrong assumption of a droplet morphology, the phase boundaries near to the tricritical point are fitted very well. The consistency in the parameter values for different proportions of water to oil, keeping all other conditions constant, points that the factor determining the phase boundaries or the emulsification failure depends only on the choice of the surfactant and oil.

3.7 Prediction of the phase boundaries

Next, the predictive power of the expressions for T_{WEB} and T_{OEB} is evaluated. Henceforth, we insert the material parameter values of the 1:1 water to oil ratio to calculate the phase boundaries according to Eq.3.4 and Eq.3.5. An equal proportion of water and oil gave a symmetric fish cut horizontally along the tricritical point. This calculated parameter free expression for the phase boundaries is then compared with the experimental data for T_{WEB} and T_{OEB} .

The predicted phase transitions (green lines) for the water and oil emulsification boundaries [T_{WEB} and T_{OEB}] is plotted with the experimental data points of 3:7 water to decane in FIG. 3.28. Here the parameter free prediction for the T_{WEB} matches very well with the experimental data. In case of T_{OEB} , the phase boundary determined from experiment is well described for low values of ϕ_s . However, when increasing the surfactant concentration the experimental data points stay below the theoretical prediction. A possible explanation for this deviation can be that microemulsion has an L3 (sponge-like) morphology at lower temperature and is not spherical as assumed in the equation. An L3- morphology implies that the

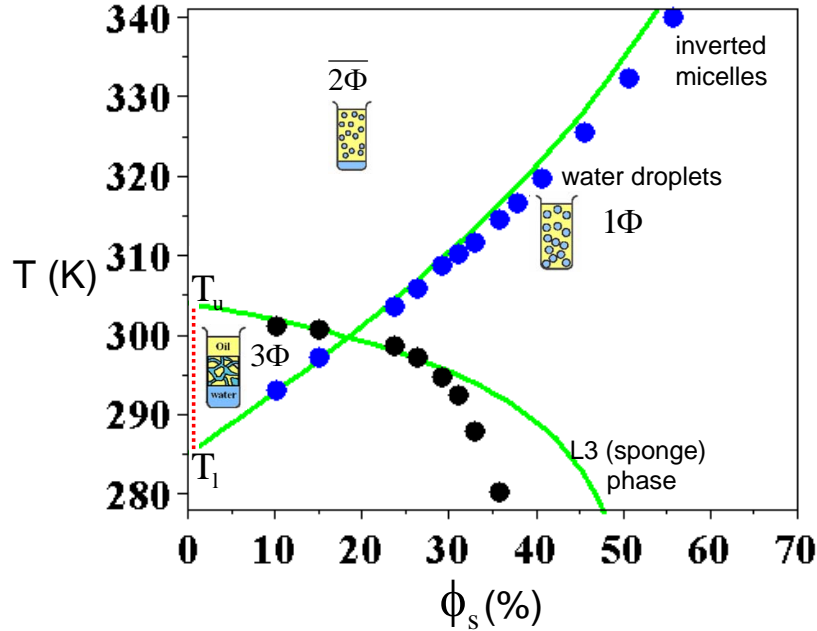


Figure 3.28: Experimental data for the water emulsification boundary, T_{WEB} [solid blue circles] and oil emulsification boundary T_{OEB} [solid black circles] of 3:7 water to oil ratio microemulsion. Predicted emulsification boundaries with the modified equations is given as green lines.

surfactant molecules self assemble in the form of bilayers instead of monolayers. Still, within the achievable experimental parameters, the prediction describes the experimental observations quite well. In FIG. 3.29, the experimental data for T_{WEB} and T_{OEB} of 7:3 water to decane is plotted along with the predicted phase boundaries (green lines). An amazingly well matching between the predicted T_{WEB} and the experimental data is observed, although the underlying morphology is L3 (sponge-like). Surprisingly, the bilayer morphology has little influence on the phase behaviour in the curvature towards water. The T_{OEB} prediction also matches well with the experimental data within the experimental accuracy. Again, an increased discrepancy is observed at higher surfactant concentration. However, in this case the experimentally observed phase boundary exceeds the predicted boundary by about $2^{\circ}C$.

In order to test the validity of the predictions, a different section of the phase prism is chosen too [FIG. 3.30]. Here the surfactant concentration is kept constant

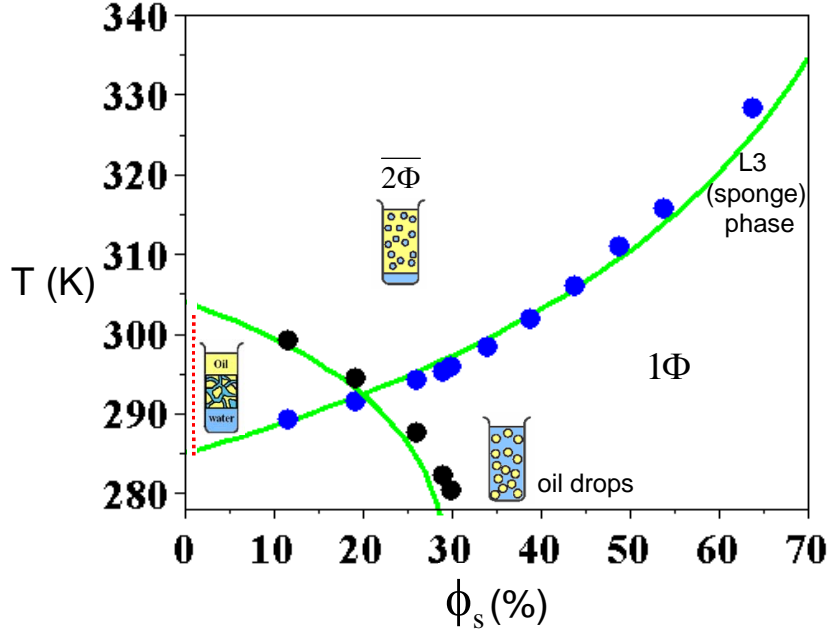


Figure 3.29: Plotting of the emulsification boundary for 7:3 water to oil ratio microemulsion according to the prediction with the modified equation (green line). Experimental data for the water emulsification boundary, T_{WEB} [solid blue circles] are shown for the microemulsion samples with varying surfactant concentration.

and the parameter α_o , i.e. the ratio of oil to water plus oil ($\alpha_o = \phi_o / (\phi_w + \phi_o)$) is varied. At low temperature ($T < T_l$) and high water proportion, surfactants are well hydrated with the water molecules. Hence the surfactant monolayer bend towards oil. An increase in temperature leads to the dehydration of the surfactant molecules, changing the curvature of the monolayer and hence the microstructure of the microemulsion. For ($T_l < T < T_u$), the surfactant possess a bicontinuous structure, with surfactant monolayer bending towards both oil and water molecules. Dehydration of the surfactant molecules at higher temperatures ($T > T_u$), bends the surfactant monolayer to enclose water molecules.

Three different sets of experimental data for T_{WEB} and T_{OEB} are shown which correspond to three different surfactant concentration - 35% (green circles), 40% (blue circles) and 50% (orange circles) respectively. The parameter-free predictions are calculated using the material parameters given in FIG. 3.25 for 1:1 water

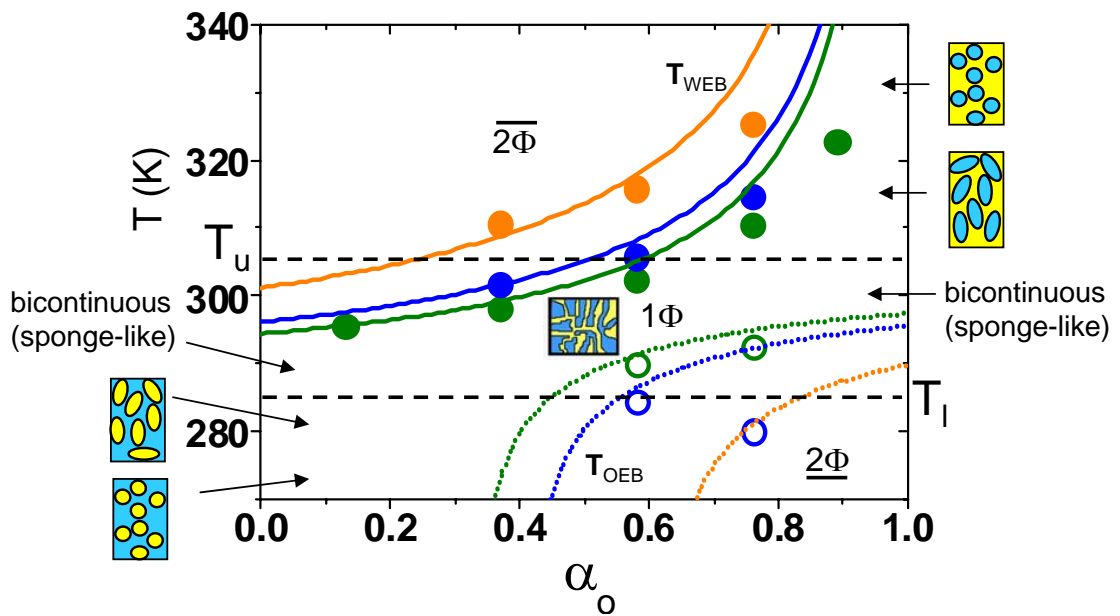


Figure 3.30: Experimental data for the evolution of water and oil emulsification boundaries with temperature and varying α_o are given by solid and open circles respectively. Surfactant concentration is fixed at 35% (green), 40% (blue) and 50% (orange). The predictions (lines) for the water emulsification boundaries (solid lines) and the oil emulsification boundaries (dotted lines) according to the modified equation for the three different surfactant concentrations are shown. The dashed line shows the temperature T_l and T_u . Microstructure of the sample at various temperatures are sketched.

to oil ratio. So there are no free-parameters in the modified equation used for the prediction-plots. The experimental data and the calculated phase boundaries are shown in FIG. 3.30. They match quite well except at higher values of α_o , where a slight mismatch is observed. In the 1ϕ -channel, between T_u (304 K) and T_l (285 K), the microstructure of the emulsion is bicontinuous. For $\alpha_o \leq 0.6$, the surfactant monolayer is bicontinuous for samples with comparatively low surfactant concentrations, $\phi_s = 35\%$ and 40% , while for $\phi_s = 50\%$, the morphology is spherical. Again for $\phi_s = 50\%$, morphology takes a bicontinuous structure for $\alpha_o \leq 0.15$.

Eventhough all the assumptions are made for a spherical morphology, the modified Helfrich equation predicts the regions with bicontinuous structure (data at intermediate temperature) amazingly well. This leads to an assumption that the bicontinuous structure may be equivalent to broken pieces of spherical droplets, where some pieces have a preferred curvature towards oil and the other towards water. At higher values of α_o (above 0.6) a deviation (5 K-10 K) of the prediction from the experimental data is observed for the water emulsification boundary. Considering a low value for the experimental data than expected T_{WEB} , at higher α_o , is due to the cylindrical and ellipsoidal shape formed by the water domains due to conservation of total interfacial area and internal water volume [76]. The oil emulsification boundaries (T_{OEB}) shift away from the water emulsification boundaries with increase in the surfactant concentration, making the 1ϕ -channel wider. Higher surfactant concentration in the microemulsion sample stabilises the water and oil domains, preventing phase separation. Within the bicontinuous regime, the experimentally determined oil emulsification boundaries for $\phi_s = 35\%$ and 40% , agrees well with the predicted phase boundaries, whereas, the experimentally determined values for T_{OEB} at $\alpha_o > 0.6$ and $\phi_s = 40\%$ showed lower phase boundaries than the predicted phase boundaries.

3.8 Coexistence of the curvatures and the interpretation of the curvature plot for C_8E_3

A good agreement between the calculated phase boundaries and the experimental data, is observed if the surfactant self-assembles into a bicontinuous or spherical morphology. This provides a deeper insight into the spontaneous curvature of the surfactant monolayer at varying temperatures. More detailed information on the spontaneous curvature (c_0) of the surfactant monolayer can be yielded from the values of the material parameters obtained in FIG. 3.30.

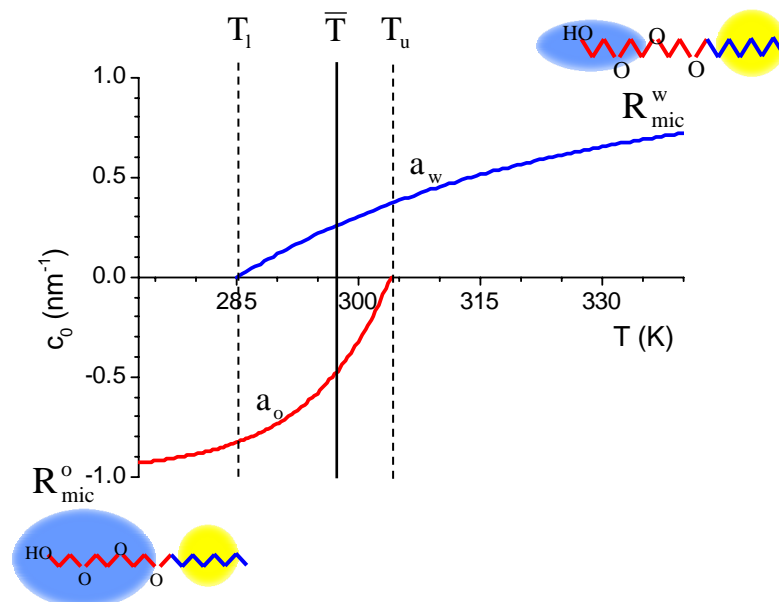


Figure 3.31: Spontaneous curvature as a function of temperature for a microemulsion with equal proportion of water to oil. At higher and lower temperatures the water and oil droplet reaches inverse micellar radii R_{mic}^w and micellar radii R_{mic}^o respectively. $'a'_w$ and $'a'_o$ gives the scaling of the surfactant morphology from a droplet structure to inverse micelle and micelle.

FIG. 3.31 shows the implication of this least square fit, on the temperature dependence of the spontaneous curvature. For the C_8E_3 -water-decane system, T_l and T_u are 19 K apart. In this region I assume two coexisting spontaneous curvatures of the surfactant monolayer. The coexistence of the two different

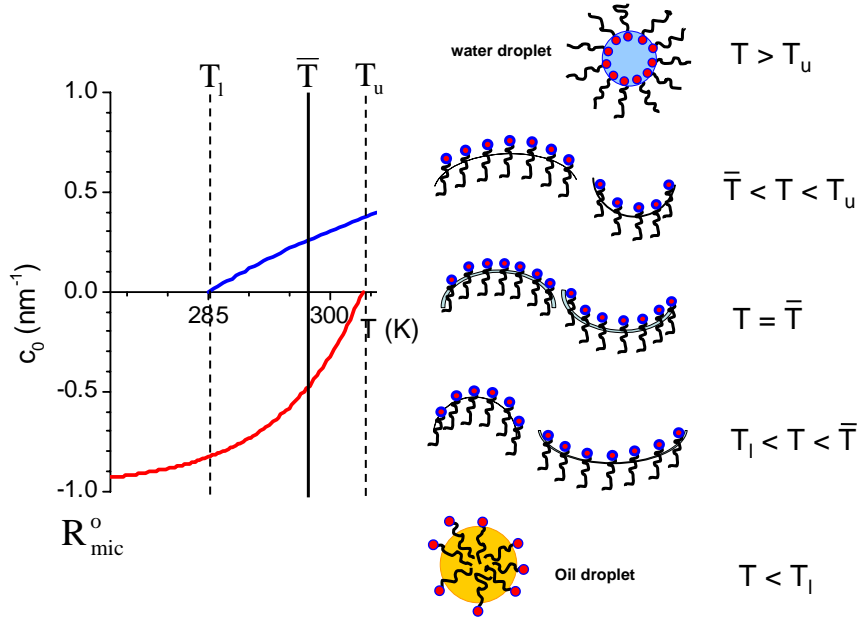


Figure 3.32: Sketch of the coexisting spontaneous curvature as a function of temperature for a microemulsion with equal proportion of water and oil. At higher and lower temperatures the water and oil droplet reaches inverse micellar radii R_{mic}^w and micellar radii R_{mic}^o respectively. $'a'_w$ and $'a'_o$ gives the scaling of the surfactant morphology from a droplet structure to inverse micelle/micelle.

curvatures could be the reason for the good agreement of the predicted and experimentally determined phase transition temperatures. A bicontinuous structure with surfactant monolayer curving towards both oil and water can be considered as broken pieces of droplets stitched together. The temperature dependent ratio of surfactant molecules that like to be curved towards water and oil contribute to the evolution of the bicontinuous structure from oil droplets ($T < T_l$) to water droplets ($T > T_u$) with varying temperature FIG. 3.32. The curvature plot hits the temperature axis at two points, at 285 K (T_l) and 304 K (T_u). The spontaneous curvature $c_0^w(T)$ increases from zero curvature at $T = T_l$ to the inverse micellar radius $c_0^w(T) \propto (R_{mic}^w)^{-1}$ at higher temperature ($T > 335\text{K}$). Similarly, $c_0^o(T)$ decreases from zero curvature at $T = T_u$ to the micellar radius $c_0^o(T) \propto (R_{mic}^o)^{-1}$ at sufficiently low temperatures ($T > 275\text{K}$).

The material parameters $'a'_w$ and $'a'_o$ are a measure of the temperature depen-

dent variation of the spontaneous curvature. This parameter contains information on the temperature dependence of the hydration of the surfactant molecules.

We can rewrite the exponential part of $R_w^{opt}(T)$, equation 1.27 as :

$$\exp(a_w(T_l - T)) = \exp\left(\frac{\kappa_B(T_l - T)}{a_{new}^w}\right) \quad (3.6)$$

where $\kappa_B = 1.38 \times 10^{-23} JK^{-1}$ is the Boltzmann constant and

$$a_{new}^w = \frac{\kappa_B}{a_w} \quad (3.7)$$

From the fits of the water emulsification boundary we have $a_w = 0.026 K^{-1}$ [FIG. 3.25]. Then,

$$a_{new}^w = \frac{\kappa_B}{0.026K^{-1}} \approx 38\kappa_B K \approx 53 \times 10^{-23} J \quad (3.8)$$

The strength of most hydrogen bonds lies between 10 and 40 kJ/mol [4]; i. e, the energy associated with one hydrogen bond is nearly 1.6×10^{-23} KJ. Then the energy comprising a_w is about $1/30^{th}$ of one hydrogen bond.

Similarly from Eq.1.28 we find :

$$\exp(a_o(T - T_u)) = \exp\left(\frac{\kappa_B(T - T_u)}{a_{new}^o}\right) \quad (3.9)$$

$$a_{new}^o = \frac{\kappa_B}{a_o} \quad (3.10)$$

From the fits of the oil emulsification boundaries we obtained, $a_o = 0.1 K^{-1}$ [FIG. 3.25] is obtained. Then,

$$a_{new}^o = \frac{\kappa_B}{0.1K^{-1}} \approx 10\kappa_B K \approx 13.8 \times 10^{-23} J \quad (3.11)$$

a_{new}^o corresponds to an energy about $1/100^{th}$ of those of a typical hydrogen bond.

The molecular origin of this energy is not clear yet and it might be related to the binding strength between the alkane tails of the surfactant molecules and

decane or to the interactions between the hydrophilic head with water molecules.

3.9 Prediction of the step of the specific heat

The specific heat is an extremely sensitive probe of the temperature dependence of the free energies, since it involves the second derivative of the temperature. Hence it probes the curvature of the free energy. From the material parameters obtained from the least square fits of the phase boundary data, we predict the values of the step of the specific heat. The curvature value is then inserted into Eq.1.42 to yield the height of the step in the specific heat. The height of the specific heat-step depends on the square of the first derivative of the spontaneous curvature with respect to temperature as,

$$\Delta C_v^{step} = \frac{4\kappa\phi_s T}{l_s} \cdot \frac{1}{1 + \frac{\bar{\kappa}}{2\kappa}} \left(\frac{\partial c_0}{\partial T} \right)^2 \quad (3.12)$$

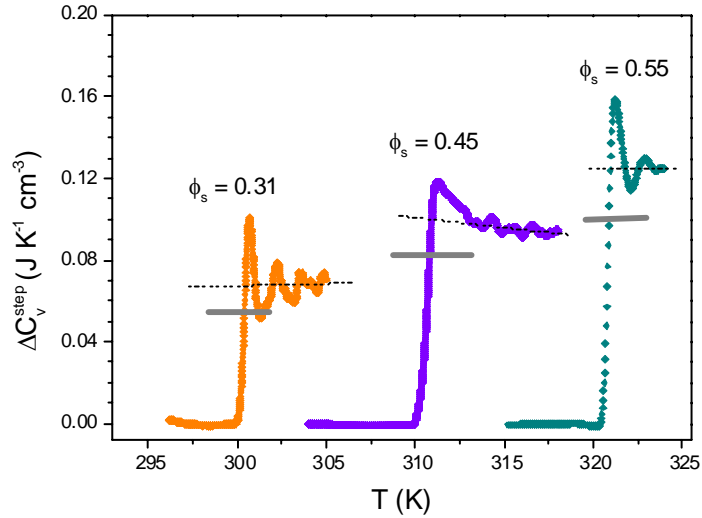


Figure 3.33: Temperature dependent variation of the specific heat for equal water to oil ratio and surfactant concentration $\phi_s = 0.31$ (orange diamonds), $\phi_s = 0.45$ (purple diamonds) and $\phi_s = 0.55$ (dark cyan diamonds). Data has been subtracted with a baseline. Mean height of the specific heat and the prediction (with the pre-factor) are shown. The thermograms are taken at 5 K/h across water emulsification boundary.

Prediction of ΔC_v^{step} according to Eq.3.12 yield values well below the experimentally determined height of ΔC_v^{step} . This lead to redefining the temperature

'T' in Eq.3.12. In water-oil-nonionic microemulsion, as the macroscopic phase transition temperatures of the microemulsion system starts from the upper (T_u) and the lower(T_l) phase boundaries of a 3ϕ -region, a temperature pre-factor is added to Eq.3.12. This prefactor, $(T - T_l)/(T_u - T_l)$, should account for the material curved towards water or oil. Addition of this concept (Eq.3.13) predicted the height of the extremely sensitive specific heat-step well.

$$\Delta C_v^{step} = \frac{4\kappa\phi_s T(T - T_l)}{l_s(T_u - T_l)} \cdot \frac{1}{1 + \frac{\bar{\kappa}}{2\kappa}} \left(\frac{\partial c_0}{\partial T}\right)^2 \quad (3.13)$$

The variation of the specific heat with temperature for microemulsion samples are given in FIG. 3.33 when crossing the water emulsification boundary $1\phi - \bar{2}\phi$. The consistency of the mean height of the specific heat-step from the calorimetry (dashed line) and the theoretical prediction according to the above equation (grey solid line) is checked for three different samples with equal water to oil ratio and increasing surfactant concentration $\phi_s = 0.31$ (orange diamonds) to $\phi_s = 0.55$ (dark cyan diamonds) are shown. The specific heat-height increases with increase in the surfactant concentration.

FIG. 3.34 shows the mean height in the specific heat step when crossing T_{WEB} for microemulsions with three different water to oil ratio and varying surfactant concentrations. Accordingly the phase transition temperatures range over a wide region from 295 K to 340 K. Open circles shows the data obtained through calorimetry experiments. The predictions according to the Eq.3.12 and Eq.3.13 are given by green dashed and solid grey lines respectively. Eq.3.13 used the parameter values obtained from the least square fit of phase diagram: $T_u = 304$ K and $T_l = 285$ K.

The data from the experiments and the predictions showed non-linearity in the height of the specific heat step with increase in temperature. The non-linear curve showed a saturation at $T \sim 320K$ for 1:1 and 3:7 water to decane ratio. The non-linearity is related to the curvature of the surfactant monolayer. Along the temperature range investigated, the surfactant monolayer encloses water. With increasing temperature, the curvature of the surfactant monolayer also increases leading the water domains enclosed by surfactant monolayer approaching inverse micellar radius. From the phase behavior studies, no significant change is ob-

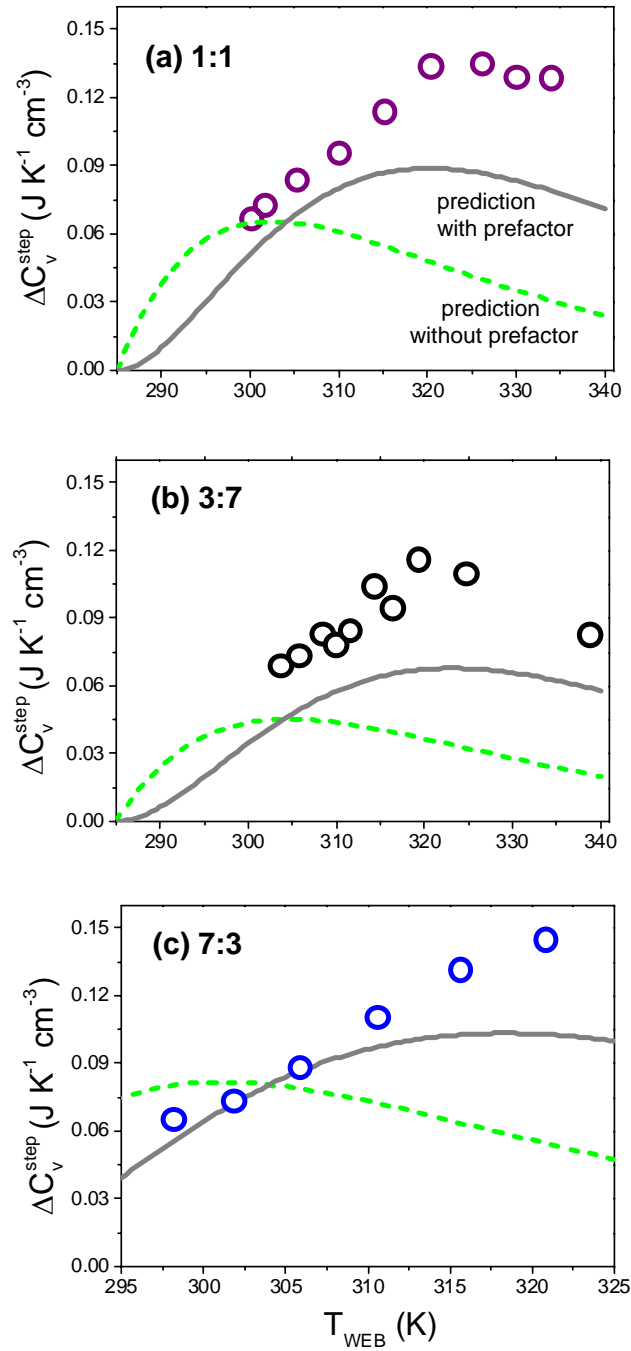


Figure 3.34: Experimental data from DSC (open circles) and the prediction to the height of the specific heat-step according to Eq.3.12 (dashed line) and Eq.3.13 with prefactor (solid line) with increasing phase transition temperature for (a) 1:1 water to oil ratio microemulsion; (b) 3:7 water to oil ratio microemulsion and (c) 7:3 water to oil ratio microemulsion.

served at this temperature. The critical micellar concentration of C_8E_3 showed demicellization at $T \sim 320K$. The underlying phenomena is not clear yet, but this could be related with the hydration of the surfactant molecules at higher temperatures which got probed by the extremely sensitive calorimetry.

The predictions according to the Eq.3.12(dashed line) also showed a non-linear trend but turned around at $T \sim 300K$. This prediction had lower values ($\Delta C_v^{step} \sim 0.03J/Kcm^3 - 0.09J/Kcm^3$) than the experimental data, over the entire temperature range at which the three different compositions investigated [FIG. 3.34]. Whereas, incorporating the lower and upper temperatures of the water and oil emulsification boundaries (T_l and T_u) for the prediction as in Eq.3.13 gave a good prediction (grey solid line) to the sensitive step-height [FIG. 3.34].

Furthermore, the height of the specific heat-step sensitively depends on the value for T_l and T_u . The sensitiveness is demonstrated using the experimental values for $T_l = 288K$ and $T_u = 301K$ from [74, 75] and inserting those into Eq.3.13. This yielded an extremely well prediction to the specific heat-step values [solid magenta lines in FIG. 3.35]. Both values varied only by 3K from my results, reflecting the sensitivity of the specific heat on the details of the width of the coexistence of both curvatures.

In both FIG. 3.34 and FIG. 3.35, the trend of the height of the specific heat-step according to Eq.3.12 passed a maximum well below those observed experimentally. For $T > 300K$ it decreased contrary to the experimental findings.

The evolution of the height in the specific heat step for microemulsion samples with a constant surfactant volume fraction of 35% with α_o [FIG. 3.36] shows nearly same value $\Delta C_v^{step} \sim 0.07 J/Kcm^3$. In FIG. 3.36, the prediction (cross) and experimentally determined data (open circles) are consistent. In this case, the total area covered by the surfactant is almost constant. The constant value for ΔC_v^{step} points that also the specific heat is determined by the total size of the surfactant monolayer and less by morphology. The specific heat is extremely dependent on the interfacial property by surfactant.

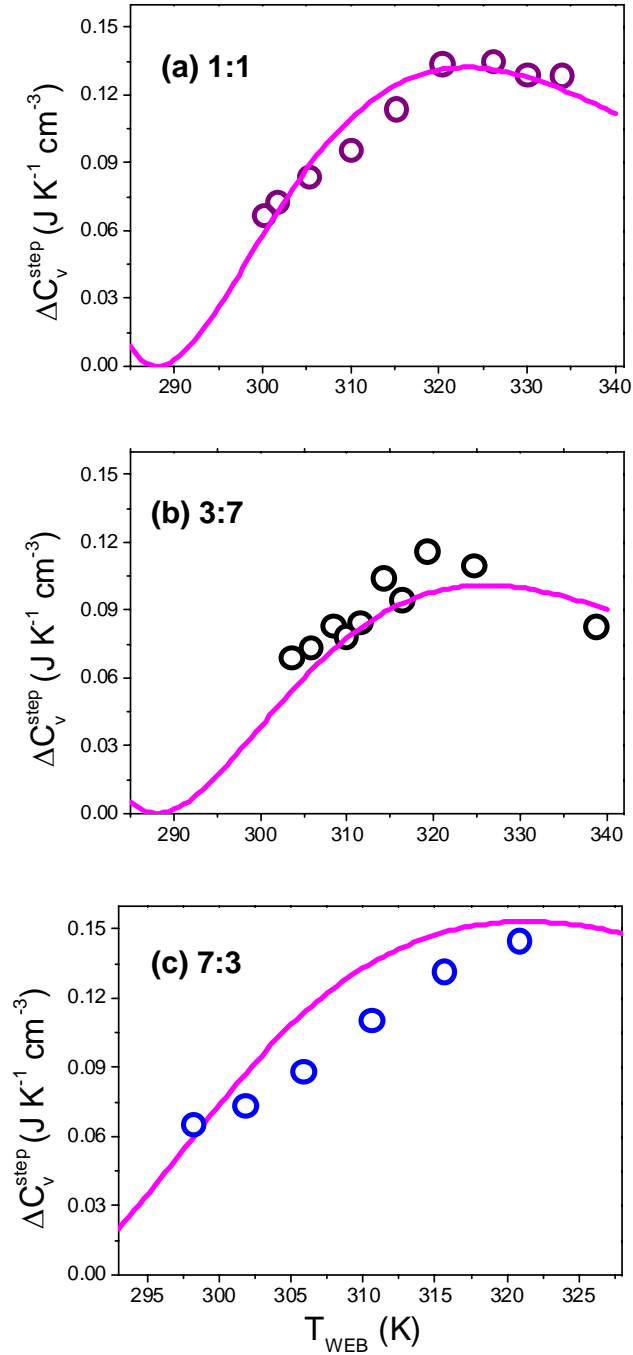


Figure 3.35: Experimental data (open circles) for the the mean height of the specific heat-step for with increasing T_{WEB} for (a) 1:1 water to oil ratio microemulsion (purple) ; (b)3:7 water to oil ratio microemulsion (black) and (c) 7:3 water to oil ratio microemulsion (blue). Theoretical prediction of the height of the specific heat-step with prefactor are shown by solid lines (magenta) for the three different data.

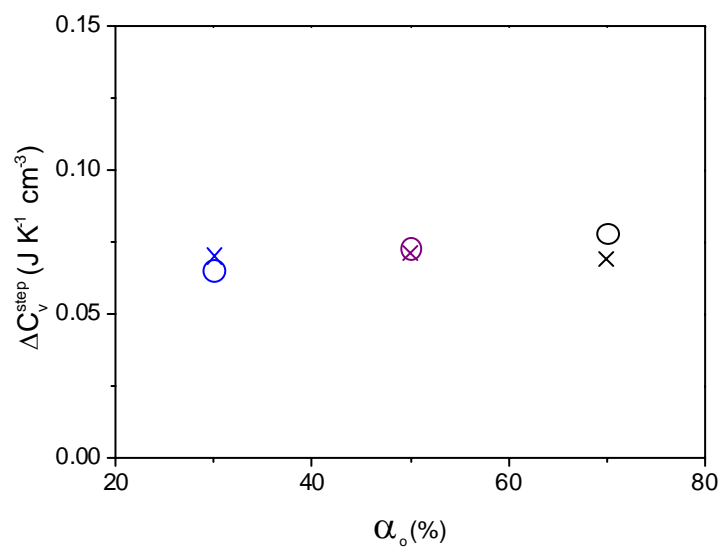


Figure 3.36: The mean height of the specific heat-step of microemulsion samples with three different $\alpha_o = \alpha_o/(\alpha_o + \alpha_w)$ and fixed surfactant volume fraction 0.35: from the differential scanning calorimetry (open circles) and according to the prediction Eq.3.13(cross).

3.10 Predictions to weak surfactant microemulsion water-octane- C_4E_1

Microemulsion with an extremely weak surfactant is investigated. C_4E_1 - octane - water ternary microemulsion is the chosen system. Here phase boundaries are predicted initially, using the material parameters. These material parameters are obtained from the previous works [34]: $T_u = 296.9$ K, $T_l = 285.9$ [34], $R_w^{mic} = 2.13$ nm, $a_w = 0.21$ K^{-1} , $R_o^{mic} = 2.2$ nm and $a_o = 0.3$ K^{-1} [35]. Later, the water and oil emulsification boundaries, (T_{WEB} and T_{OEB}), are determined experimentally by the visual inspection of the C_4E_1 - octane - water, with increasing and decreasing temperature [followed the same procedures used for C_8E_3 -decane-water]. The experimentally obtained phase boundaries are plotted with the prediction of the phase boundaries T_{WEB} and T_{OEB} [FIG. 3.37]. Surprisingly, even for an an

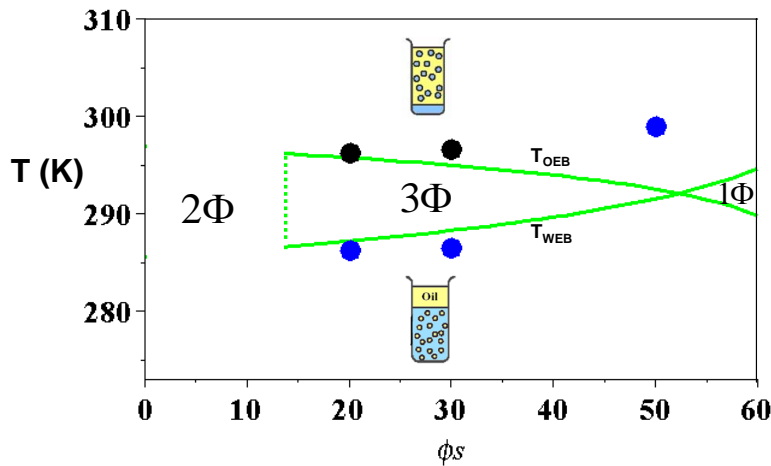


Figure 3.37: Experimental data for the T_{WEB} (blue circles) and T_{OEB} (black circles) for the C_4E_1 - octane - water microemulsion. A 10% surfactant-volume fraction the sample is in 2Φ . Dotted line separates 2Φ and 3Φ . Green line shows the prediction.

extremely weak surfactant microemulsion, where the interfacial profile becomes diffuse, the prediction works very well for a 3ϕ -region.

Chapter 4

Conclusions

My work characterizes and predicts macroscopic phase transitions of nonionic microemulsions. To investigate the phase behaviour two different approaches were followed. In the first approach, the phase behaviour of C_8E_3 -water-decane is described using conservation of the interface. This yielded the length scale of the microstructure which was later revealed by dynamic light scattering experiment.

In the second approach, Helfrich bending free energy is used for explanation of the phase behaviour of the ternary system. Calorimetric experiments probed this free energy and thereby the temperature dependent spontaneous curvature of the surfactant monolayer.

Both these approaches converged to the same phase diagram upon investigation. Eventhough the modification to the Helfrich free energy has been done for a spherical morphology, it predicted a major region of the phase diagram with other morphologies amazingly well. In particular, in 3Φ -region surfactant monolayer takes bicontinuous morphology.

Here, the non linear evolution of the spontaneous curvature with temperature, unlike previous works, showed a coexisting region as wide as the 3Φ -region of the non-ionic microemulsion. Quantifying this nonlinearity might lead to a clear picture in future about the interplay of the surfactant monolayers with the water.

The successful prediction of the extremely sensitive specific heat-height shows the validity of the modified Helfrich free energy in moderate as well as in weak surfactant system. Consistency of the experimentally determined data and predictions for microemulsions with various compositions and surfactants underlines

the concept and its generic property.

Appendix A

First derivative of the Helfrich free energy per unit volume for spherical droplets can be written as

$$\frac{\partial F}{\partial R} = \frac{2\kappa\phi_s}{l_s} \frac{\partial}{\partial R} \left\{ \frac{[1 - Rc_0(T)]^2}{R^2} + \frac{(\bar{\kappa}/2\kappa)}{R^2} \right\} \quad (1)$$

$$\frac{\partial F}{\partial R} = \frac{2\kappa\phi_s}{l_s} \frac{\partial}{\partial R} \left\{ \frac{[1 - 2Rc_0(T) + R^2c_0^2(T)]}{R^2} + \frac{(\bar{\kappa}/2\kappa)}{R^2} \right\} \quad (2)$$

$$= \frac{2\kappa\phi_s}{l_s} \frac{\partial}{\partial R} \left\{ \frac{1}{R^2} - \frac{2c_0(T)}{R^2} + c_0^2(T) + \frac{(\bar{\kappa}/2\kappa)}{R^2} \right\} \quad (3)$$

$$= \frac{2\kappa\phi_s}{l_s} \left\{ \frac{-2}{R^3} - \frac{2(-1)}{R^2} \cdot c_0(T) + \frac{-2}{R^3}(\bar{\kappa}/2\kappa) \right\} \quad (4)$$

$$= \frac{2\kappa\phi_s}{l_s} \left\{ \frac{-2[1 + \bar{\kappa}/2\kappa]}{R^3} + \frac{2c_0(T)}{R^2} \right\} \quad (5)$$

$$\frac{\partial F}{\partial R} = 0 \quad (6)$$

Therefore,

$$\frac{2\kappa\phi_s}{l_s} \frac{-2[1 + \bar{\kappa}/2\kappa]}{R^3} + \frac{2\kappa\phi_s}{l_s} \frac{2c_0(T)}{R^2} = 0 \quad (7)$$

$$R^{opt}(T) = \frac{[1 + \bar{\kappa}/2\kappa]}{c_0(T)} \quad (8)$$

Appendix B

.0.1 The height of the specific heat-step at the emulsification boundary

$$\Delta C_v = C_v^{2\Phi} - C_v^{1\Phi} \quad (9)$$

$$C_v^{1\Phi}(T) = -T \frac{\partial^2 F(R_{1\Phi})}{\partial T^2} \quad (10)$$

Inserting the droplet radius in 1Φ from gives,

$$\frac{\partial F(R_{1\Phi})}{\partial T} = \frac{\partial}{\partial T} \left\{ \frac{2\kappa\phi_s}{l_s R^2} \left(1 - 2Rc_o(T) + R^2 c_o^2(T) + \frac{\bar{\kappa}}{2\kappa} \right) \right\} \quad (11)$$

$$= \frac{2\kappa\phi_s}{l_s R^2} \left\{ -2R \frac{\partial c_o(T)}{\partial T} + R^2 \frac{\partial c_o^2(T)}{\partial T} \right\} \quad (12)$$

$$\frac{\partial^2 F(R_{1\Phi})}{\partial T^2} = \frac{2\kappa\phi_s}{l_s R^2} \frac{\partial}{\partial T} \left[-2R \frac{\partial^2 c_o(T)}{\partial T^2} + R^2 \frac{\partial^2 c_o^2(T)}{\partial T^2} \right] \quad (13)$$

$$= \frac{2\kappa\phi_s}{l_s} \left[\frac{\partial^2 c_o^2(T)}{\partial T^2} - \frac{2}{R_{1\Phi}} \frac{\partial^2 c_o(T)}{\partial T^2} \right] \quad (14)$$

$$C_v^{1\Phi} = \frac{-2\kappa\phi_s T}{l_s} \left[\frac{\partial^2 c_o^2(T)}{\partial T^2} - \frac{2}{R_{1\Phi}} \frac{\partial^2 c_o(T)}{\partial T^2} \right] \quad (15)$$

Now $C_v^{2\Phi}$:

$$C_v^{2\Phi}(T) = -T \frac{\partial^2 F(R_{opt})}{\partial T^2} \quad (16)$$

R_{opt} is inserted from eq. ,

$$F = \frac{2\kappa\phi_s}{l_s\left(\frac{1+\bar{\kappa}}{c_o(T)}\right)^2} \left[\left(1 - \frac{1+\bar{\kappa}}{c_o(T)} \cdot c_o(T)\right)^2 + \frac{\bar{\kappa}}{2\kappa} \right] \quad (17)$$

$$= \frac{2\kappa\phi_s c_o^2(T)}{l_s\left(1 + \frac{\bar{\kappa}}{2\kappa}\right)^2} \left[\left(1 - \frac{2\kappa + \bar{\kappa}}{2\kappa}\right)^2 + \frac{\bar{\kappa}}{2\kappa} \right] \quad (18)$$

$$= \frac{2\kappa\phi_s c_o^2(T)}{l_s\left(1 + \frac{\bar{\kappa}}{2\kappa}\right)^2} \left[\left(\frac{\bar{\kappa}}{2\kappa}\right)^2 + \frac{\bar{\kappa}}{2\kappa} \right] \quad (19)$$

$$= \frac{2\kappa\phi_s c_o^2(T)}{l_s\left(1 + \frac{\bar{\kappa}}{2\kappa}\right)^2} 2\kappa \left[1 + \frac{\bar{\kappa}}{2\kappa}\right] \quad (20)$$

$$F(R_{opt}) = \frac{\bar{\kappa}\phi_s c_o^2(T)}{l_s\left(1 + \frac{\bar{\kappa}}{2\kappa}\right)} \quad (21)$$

$$\frac{\partial^2 F(R_{opt})}{\partial T^2} = \frac{\bar{\kappa}\phi_s}{l_s\left(1 + \frac{\bar{\kappa}}{2\kappa}\right)} \frac{\partial^2 c_o^2(T)}{\partial T^2} \quad (22)$$

$$C_v^{2\Phi}(T) = -T \frac{\partial^2 F(R_{opt})}{\partial T^2} = \frac{-T \bar{\kappa}\phi_s}{l_s\left(1 + \frac{\bar{\kappa}}{2\kappa}\right)} \frac{\partial^2 c_o^2(T)}{\partial T^2} \quad (23)$$

The step in the specific heat $\Delta C_v^{step} = \Delta C_v^{2\Phi} - \Delta C_v^{1\Phi}$

$$\Delta C_v = \left[\frac{-T \bar{\kappa}\phi_s}{l_s\left(1 + \frac{\bar{\kappa}}{2\kappa}\right)} \frac{\partial^2 c_o^2(T)}{\partial T^2} \right] - \left[\frac{-2\kappa\phi_s T}{l_s} \left(\frac{\partial^2 c_o^2(T)}{\partial T^2} - \frac{2}{R_{1\Phi}} \frac{\partial^2 c_o(T)}{\partial T^2} \right) \right] \quad (24)$$

$$= \frac{4\kappa\phi_s T}{l_s} \left[\frac{1}{4\kappa} \cdot \frac{-\bar{\kappa}}{\left(1 + \frac{\bar{\kappa}}{2\kappa}\right)} \frac{\partial^2 c_o^2(T)}{\partial T^2} + \frac{1}{2} \frac{\partial^2 c_o^2(T)}{\partial T^2} - \frac{1}{R_{1\Phi}} \cdot \frac{\partial^2 c_o(T)}{\partial T^2} \right] \quad (25)$$

$$= \frac{4\kappa\phi_s T}{l_s} \left[\frac{\partial^2 c_o^2(T)}{\partial T^2} \left(\frac{1}{2} - \frac{-\bar{\kappa}}{4\kappa\left(1 + \frac{\bar{\kappa}}{2\kappa}\right)} \right) - \frac{1}{R_{1\Phi}} \frac{\partial^2 c_o(T)}{\partial T^2} \right] \quad (26)$$

$$= \frac{4\kappa\phi_s T}{l_s} \left[\frac{1}{2} \frac{\partial^2 c_o^2(T)}{\partial T^2} \frac{1}{\left(1 + \frac{\bar{\kappa}}{2\kappa}\right)} - \frac{1}{R_{1\Phi}} \frac{\partial^2 c_o(T)}{\partial T^2} \right] \quad (27)$$

$$= \frac{4\kappa\phi_s T}{l_s} \left\{ \frac{1}{2} \left[2 \left(\frac{\partial c_o(T)}{\partial T} \right)^2 + 2c_o(T) \frac{\partial^2 c_o(T)}{\partial T^2} \right] \frac{1}{\left(1 + \frac{\bar{\kappa}}{2\kappa}\right)} - \frac{1}{R_{1\Phi}} \frac{\partial^2 c_o(T)}{\partial T^2} \right\} \quad (28)$$

$$= \frac{4\kappa\phi_s T}{l_s} \left\{ \left[\left(\frac{\partial c_o(T)}{\partial T} \right)^2 + c_o(T) \frac{\partial^2 c_o(T)}{\partial T^2} \right] \frac{1}{\left(1 + \frac{\bar{\kappa}}{2\kappa}\right)} - \frac{1}{R_{1\Phi}} \frac{\partial^2 c_o(T)}{\partial T^2} \right\} \quad (29)$$

$$= \frac{4\kappa\phi_s T}{l_s} \left\{ \frac{\left(\frac{\partial c_o(T)}{\partial T}\right)^2}{\left(1 + \frac{\bar{\kappa}}{2\kappa}\right)} + \frac{c_o(T)}{\left(1 + \frac{\bar{\kappa}}{2\kappa}\right)} \frac{\partial^2 c_o(T)}{\partial T^2} - \frac{1}{R_{1\Phi}} \frac{\partial^2 c_o(T)}{\partial T^2} \right\} \quad (30)$$

$$= \frac{4\kappa\phi_s T}{l_s} \left\{ \frac{\left(\frac{\partial c_o(T)}{\partial T}\right)^2}{\left(1 + \frac{\bar{\kappa}}{2\kappa}\right)} + \frac{1}{R_{opt}} \frac{\partial^2 c_o(T)}{\partial T^2} - \frac{1}{R_{1\Phi}} \frac{\partial^2 c_o(T)}{\partial T^2} \right\} \quad (31)$$

Then,

$$\Delta C_v = \frac{4\kappa\phi_s T}{l_s} \left\{ \frac{\partial^2 c_o(T)}{\partial T^2} \left[\frac{R_{1\Phi} - R_{opt}}{R_{opt} R_{1\Phi}} \right] + \frac{\left(\frac{\partial c_o(T)}{\partial T}\right)^2}{1 + \frac{\bar{\kappa}}{2\kappa}} \right\} \quad (32)$$

Program (MAPLE) for the least square fit of the phase boundary data of 1:1 water to oil microemulsion

```
> restart:
> with(Statistics):
> with(Maplets[Elements]):
> with(LinearAlgebra):
> with(ArrayTools):
> with(linalg):
```

READ DATA : Tweb

```
> fit_range := 80;
> fd := open
  ("D:\\Programs_Maple_ME\\volfrac_correction_weightfraction\\
  50_50_data\\doc-files\\volume fraction_waterbath_Tweb.txt",
  READ );
```

PLOTTING Tweb THE DATA

```
> data_in:=readdata(fd,float,2):
> close(fd);
> plot (data_in, x=30..60, y=290..330,style=point,symbol=
  solidcircle,symbolsize=25,color=blue):
```

Reading Tweb data in matrix:

```
> in_matrix := convert(data_in, Matrix):
  dim := Dimension(in_matrix)[1];
> x_data_all := Vector[column]( dim, datatype=anything):
  y_data_all := Vector[column]( dim, datatype=anything):
  Fill(0.0,x_data_all);
> Fill(0.0, y_data_all);
> Copy(in_matrix, dim, 1, y_data_all);
  Copy(in_matrix, 0, 1, x_data_all);
> list[in_matrix]:
> list[x_data_all]:
```

Pre-fix values :

```
> ls:=1.0:
```

```
> phi_w :=(100-phi_s)/2:
```

Fitting with the formula:

```
> Tweb := Tl-(1/aw)*(ln(1-((R/(3*ls))*((phi_s)/(phi_w+0.5*  
(phi_s)))))):
```

```
> fit_sol :=  
NonlinearFit(Tweb, x_data_all, y_data_all, phi_s,  
parameternames=[R,aw,Tl],parameterranges=[R=0.000000001.  
.4,aw=0.001..2,Tl=273..296],initialvalues=[R=1.8,aw=0.03,  
Tl=289],output=solutionmodule):
```

```
> #fit_sol:-Results(parametervalues):
```

```
> param := fit_sol:-Results(parametervector):
```

```
> R_f := param[1];
```

```
> Tl_f:= param[3];
```

```
> aw_f:= param[2];
```

```
      R_f:= 1.73699242089939543  
      Tl_f:= 284.815966789140418  
      aw_f:= 0.0257601951549700366
```

(2.2.1)

Equation with the new parameters :

```
> fit_Tweb := Tl_f-(1/aw_f)*(ln(1-((R_f/(3*ls))*((phi_s)/  
(phi_w+0.5*(phi_s))))));
```

```
fit_Tweb := 284.815966789140418 - 38.81958169 ln(1 - 0.01157994947  $\phi_s$ )
```

(2.2.2)

```
> plot([fit_Tweb,data_in],phi_s=0..70,273..345,color=[red,  
blue],style=[line,point],symbolsize=[3,20]):
```

Toeb Values:

```
> fit_range := 80;
```

```
fit_range := 80
```

(2.2.3)

```
> fd := open
```

```
("D:\\Programs_Maple_ME\\volfrac_correction_weightfractio  
n\\50_50_data\\doc-files\\volume fraction_WBath_Toeb.txt",  
READ );
```

```
fd := 0
```

(2.2.4)

PLOTTING BOTH THE DATA

```
> data_in3:=readdata(fd,float,2):
```

```
> close(fd);
```

```
> plot([data_in,data_in2,data_in3], x=20..65, y=273..335,  
style=[point,point],symbol=[solidcircle,circle,  
solidcircle],symbolsize=[25,25],color=[blue,black,blue],  
axes=boxed):
```

Reading data in matrix:

```
> in_matrix3 := convert(data_in3, Matrix):
```

```
dim := Dimension(in_matrix3)[1];
```

```

> x_data_all3 := Vector[column]( dim, datatype=anything):
  y_data_all3 := Vector[column]( dim, datatype=anything):
  Fill(0.0,x_data_all3);
> Fill(0.0, y_data_all3);
> Copy(in_matrix3, dim, 1, y_data_all3);
  Copy(in_matrix3, 0, 1, x_data_all3);
> list[in_matrix3]:
                                     dim := 5

```

(2.2.5)

```
>
```

non-fitted values

```

> phi_w:=0.5*(100-phi_s);
> ls:=1.0;
> phi_o:=0.5*(100-phi_s);
                                      $\phi_w := 50.0 - 0.5 \phi_s$ 
                                      $ls := 1.0$ 
                                      $\phi_o := 50.0 - 0.5 \phi_s$ 

```

(2.2.6)

Fitting with the formula:

```

> Toeb := Tu+(1/ao)*(ln(1-((Ro/(3*ls))*((phi_s)/(phi_o+0.5*
  (phi_s)))))):
> fit_sol :=
  NonlinearFit(Toeb, x_data_all3, y_data_all3, phi_s,
  parameternames=[Ro,ao,Tu],parameterranges=[Ro=0.001..4,
  ao=0.0005..2,Tu=274..340],initialvalues=[Ro=2.2,ao=0.1,
  Tu=304],output=solutionmodule):
> #fit_sol:-Results(parametervalues):
> param := fit_sol:-Results(parametervector):
> Ro_f := param[1];
> Tu_f:= param[3];
> ao_f:= param[2];
                                      $Ro_f := 3.44549370168633784$ 
                                      $Tu_f := 304.242836156682870$ 
                                      $ao_f := 0.0965701869133676754$ 

```

(2.2.7)

```

> fit_Toeb :=Tu_f+(1/ao_f)*ln(1-(Ro_f*(phi_s)/(3*ls*
  (phi_o+0.5*(phi_s)))));
  fit_Toeb := 304.242836156682870 + 10.35516273 ln(1 - 0.02296995801  $\phi_s$ )

```

(2.2.8)

```
>
```

Final plot :

```

> plot([fit_Tweb,data_in,fit_Toeb,data_in3],phi_s=0..70,
  275..340,color=[red,blue,red,black,gold],style=[line,
  point,line,point,point],symbol=[solidcircle,solidcircle,
  circle],symbolsize=[25,25,25],font=[TIMES, BOLD, 20]):

```

```
>
```


References

- [1] Hakan Wennerstrom D. Fennell Evans. *The Colloidal Domain : Where Physics, Chemistry, Biology, and Technology Meet*. Wiley-VCH, 1999. [x](#), [8](#), [9](#)
- [2] M Kahlweit and R Strey. Phase behavior of ternary systems of the type h2o-oil-nonionic amphiphile (microemulsions). *Angew. Chem. Int. Ed. Engl.*, 24: 654–668, 1985. [xi](#), [19](#), [20](#), [23](#)
- [3] M Daoud and C.E. Williams. *Soft Matter Physics*. Springer, 1999. [2](#), [3](#), [8](#), [14](#)
- [4] J Israelachvili. *Intermolecular and Surface Forces (second edition)*. Academic Press, 1991. [3](#), [8](#), [88](#)
- [5] Tadros F. *Applied Surfactant : Priciples and Applications*. Wiley-VCH, 2005. [3](#)
- [6] J. F. Goodman J. M. Corkill and S. P Harrold. Thermodynamics of micellization of non-ionic detergents. *Trans. Faraday Soc.*, 60:202, 1964. [3](#), [70](#)
- [7] H.-F. Eicke. Surfactants in nonpolar solvents. aggregation and micellization. *Topics in Current Chemistry*, 87:85–145, 1980. [5](#), [6](#), [7](#)
- [8] Toshihiro Jin-Noa Kijiro Kon-Noa and Ayao Kitahara. *Journal of Colloid and Interface Science*, 49:3, 1974. [5](#)

REFERENCES

- [9] A KITAHARA and K KON-NO. *Micelle Formation in Nonaqueous Media, Colloidal Dispersions and Micellar Behavior*. ACS Symposium Series; American Chemical Society, 1975. 5
- [10] D. O Shah. *Micelles, Microemulsions, and Monolayers*. Science and Technology, CRC Press, 1998. 6
- [11] Martin J. Schick. *Nonionic surfactants: Physical chemistry (Surfactant science series, Volume 23)*. Marcel Dekker, Inc., New York and Basel, 1987. 6
- [12] Nagarajan R Ruckenstein, E. Aggregation of amphiphiles in nonaqueous media. *The Journal of Physical Chemistry*, 84:1349–1358, 1980. 6
- [13] C.R Singleterry. Micelle formation and solubilization in nonaqueous solvents. *Journal of the American Oil Chemists' Society*, 32:446–452, 1955. 6
- [14] M.; Picot C. Ravey, J. C.; Buzier. Micellar structures of nonionic surfactants in apolar media. *Journal of Colloid and Interface Science*, 97:9–25, 1984. 7
- [15] R Strey. Water-nonionic surfactant systems and the effect of additives. *BERICHTE DER BUNSEN-GESELLSCHAFT-PHYSICAL CHEMISTRY CHEMICAL PHYSICS*, 100:182–189, 1996. 8
- [16] Rosen M. J. *Surfactants and interfacial phenomena (third edition)*. Wiley and Sons, Inc., New York, 2004. 10
- [17] W Helfrich. Elastic properties of lipid bilayerstheory and possible experiments. *Z. Naturforsch. C*, 28:693–703, 1973. 13, 24
- [18] U. Olsson and H. Wennerstrom. Globular and bicontinuous phases of nonionic surfactant films. *Advances in Colloid and Interface Science*, 49:113–146, 1994. 13, 32, 37
- [19] J. Daicic, U. Olsson, and H. Wennerstrm. Phase equilibria of balanced microemulsions. *Langmuir*, 11(7):2451–2458, 1995. URL www.scopus.com. Cited By (since 1996): 35. 13, 37

REFERENCES

- [20] B.Lindman and H. Wennerstrom. *Topics in Current Chemistry : Micelles. Amphiphile Aggregation in Aqueous Solution*. Springer-Verlag, 1980. [15](#)
- [21] Nabil Naouli and Henri L. Rosano. Chapter 7. In *Design of Single Surfactant Microemulsion Micro/Nanoencapsulation of Active Food Ingredients*, volume 1007 of *ACS Symposium Series*, pages 116–130, 2009. [17](#)
- [22] T.P. Hoar and J.H Schulman. Transparent water-in-oil dispersions; the oleopathic hydromicelle. *Nature*, 152:102–103, 1943. [17](#)
- [23] J.H. Schulman and D.P. Riley. X-ray investigation of the structure of transparent oilwater disperse systems.1. *J. Colloid Sci.*, 3:383405, 1948. [17](#)
- [24] J.E. Bowcott and J.H. Schulman. Emulsions- control of droplet size and phase continuity in transparent oilwater dispersions stabilized with soap and alcohol. *Z. Electrochem.*, 59:283–290, 1955. [17](#)
- [25] J.H. Schulman and J.A. Friend. Light scattering investigation of the structure of transparent oilwater disperse systems. 2. *J. Colloid Sci.*, 4:497–509, 1949. [17](#)
- [26] Stoeckenius W. Schulman, J.H. and L.M. Prince. Mechanism of formation and structure of microemulsions by electron microscopy. *J. Phys. Chem.*, 63: 1677–1680, 1959. [17](#)
- [27] M. Kahlweit. The phase behaviour of the type h2ooilnonionic surfactant-electrolyte. *J. Colloid Interface Sci.*, 90:197202, 1982. [18](#)
- [28] Lessner E. Kahlweit, M. and R. Strey. Influence of the properties of the oil and the surfactant on the phase-behaviour of systems of the type h2ooilnonionic surfactant. *J. Phys. Chem.*, 87:50325040, 1983. [18](#)
- [29] T Sottmann and R Strey. Ultralow interfacial tensions in water-n-alkane-surfactant systems. *J. Chem. Phys.*, 106:20, 1997. [18](#), [79](#), [80](#)
- [30] H.L. Rosano and M. Clause. *Microemulsion Systems : Surfactant Science Series; Volume 24*. Marcel Dekker, New York, 1987. [19](#)

REFERENCES

- [31] PA Winsor. Hydrotropy, solubilisation and related emulsification processes. *Trans. Faraday Soc.*, 44:376–398, 1948. 20, 21
- [32] R ; FIRMAN P KAHLWEIT, M; STREY. Search for tricritical points in ternary-systems - water oil nonionic amphiphile. *JOURNAL OF PHYSICAL CHEMISTRY*, 90:671–677, 1986. 21, 22
- [33] G. Gompper and M. Schick. *Self-assembling amphiphilic systems : in : Phase Transitions and Critical Phenomena*, volume 16. Academic Press, London, 1994. 22, 24, 25
- [34] R. Strey M. Kahlweit and G. Busse. Microemulsions: A qualitative thermodynamic approach. *J. Phys. Chem.*, 94:3881–3894, 1990. 23, 96
- [35] 101 (1999) Doris Vollmer rule. How to calculate phase diagrams for microemulsions - a simple rule. *Fett/Lipid*, 101:379–388, 1999. 23, 34, 77, 96
- [36] T. VanDinter O. Desrosier and S. K. Saunders. *Can. J. Chem.*, 62:56, 1984. 24
- [37] G. Perron G. Roux and J.E. Desnoyers. *J. Solution Chem.*, 7:639, 1978. 24
- [38] M. Schick and Wei-Heng Shih. Simple microscopic model of a microemulsion. *Phys. Rev. Lett.*, 59:1205–1208, Sep 1987. doi: 10.1103/PhysRevLett.59.1205. URL <http://link.aps.org/doi/10.1103/PhysRevLett.59.1205>. 24, 27
- [39] B. Widom. Ii. theoretical modeling: An introduction. *Berichte der Bunsengesellschaft fr physikalische Chemie*, 100(3):242–251, 1996. ISSN 0005-9021. doi: 10.1002/bbpc.19961000310. URL <http://dx.doi.org/10.1002/bbpc.19961000310>. 24, 27
- [40] G Gompper. Ginzburg-landau theories of ternary amphiphilic systems. *BERICHTE DER BUNSEN-GESELLSCHAFT-PHYSICAL CHEMISTRY CHEMICAL PHYSICS*, 100:264–271, 1996. 24

REFERENCES

- [41] D. Roux M. Gelbart, editor. *Micelles, Membranes, Microemulsions and Monolayers*. Springer, Berlin, 1995. [24](#)
- [42] Y. Talmon and S. Prager. Statistical thermodynamics of phase equilibria in microemulsions. *J. Chem. Phys.*, 69:2984, 1978. [25](#)
- [43] E. Ruckenstein and J. Chi. *J. Chem. Soc. Faraday Trans.*, 271:1690, 1975. [25](#)
- [44] P.G. de Gennes and C. Taupin. *J. Phys. Chem.*, 86:2294, 1982. [25](#), [26](#), [28](#)
- [45] P. Levinson J. Jouffroy and P.G. de Gennes. *J. Phys. (France)*, 43:1241, 1982. [25](#)
- [46] B. Widom. *J. Chem. Phys.*, 81:1030, 1984. [25](#)
- [47] D. Andelman. M. E. Cates. D. Roux and S. A. Safran. *J. Chem. Phys.*, 87:7229, 1987. [25](#), [29](#)
- [48] J. H. Schulman and J. B. Montagne. Formation of microemulsions by amino alkyl alcohols. *Annals of the New York Academy of Sciences*, 92:366–371, 1961. [26](#)
- [49] M. Ellerby H. Reiss and J. A. Manzanares. Configurational entropy of microemulsions: The fundamental length scale. *J. Chem. Phys.*, 99:9930, 1993. [26](#)
- [50] M. Kahlweit and H. Reiss. *Langmuir*, 7:2929, 1991. [26](#)
- [51] J. Jen M. Kahlweit and G. Busse. *J. Phys. Chem.*, 97:6917, 1992. [26](#)
- [52] Wheeler JC and B Widom. Phase transitions and critical points in a model 3-component system. *J. Am. Chem. Soc.*, 90:3064, 1968. [27](#)
- [53] A. Robledo. Exact thermodynamic correspondence between a lattice model microemulsion and simpler spin systems. *EPL (Europhysics Letters)*, 1(6):303, 1986. URL <http://stacks.iop.org/0295-5075/1/i=6/a=006>. [27](#)

REFERENCES

- [54] A. Robledo. Spin ising transcription of a lattice model of micellar solutions. *Physical Review A*, 36(8):4067–4071, 1987. URL www.scopus.com. Cited By (since 1996): 4. [27](#)
- [55] M. W. Matsen and D. E. Sullivan. Lattice model for surfactants in solution. *Phys. Rev. A*, 41:2021–2030, Feb 1990. doi: 10.1103/PhysRevA.41.2021. URL <http://link.aps.org/doi/10.1103/PhysRevA.41.2021>. [27](#)
- [56] W. Helfrich. *Z. Naturforsch. C*, 33a:305, 1978. [28](#)
- [57] S. A. Safran, L. A. Turkevich, and P. Pincus. Cylindrical microemulsions: a polymer-like phase ? *J. Physique Lett*, 45:L–64, 1984. [28](#), [32](#), [37](#)
- [58] J. Vollmer D. Vollmer and R. Strey. *Phys. Rev. E*, 54:3028, 1996. [28](#), [37](#)
- [59] H. Bagger-Jrgensen, U. Olsson, and K. Mortensen. *Langmuir*, 12:4057, 1996. [29](#)
- [60] D. Vollmer, J. Vollmer, R. Strey, H.-G. Schmidt, and G. Wolf. *Journal of Thermal Analysis*, 51:9–27, 1998. [29](#), [36](#), [37](#)
- [61] R Strey. Microemulsion microstructure and interfacial curvature. *Colloid & Polymer Science*, 272:1005–1019, 1994. [32](#)
- [62] R. Strey D. Vollmer and J. Vollmer. Oscillating phase separation in microemulsions. i.experimental observation. *J. Chem. Phys.*, 107:3619, 1997. [36](#), [37](#)
- [63] J Vollmer D. Vollmer and A. J. Wagner. Oscillatory kinetics of phase separation in a binary mixture under constant heating. *Phys. Chem. Chem. Phys.*, 4:1380–1385, 2002. [36](#)
- [64] D. Vollmer and P. Ganz. Microcalorimetric investigation of the upper phase boundary of water-in-oil microemulsions;. *J. Chem. Phys.*, 103:11, 1995. [36](#)
- [65] Strey R Vollmer J, Vollmer D. *J chem Phys*, 107:3627, 1997. [36](#)
- [66] StreyR Vollmer D, Vollmer J. *EuroPhys Lett*, 39:245, 1997. [36](#)

REFERENCES

- [67] D. Vollmer. Phase separation in microemulsions: stepwise change of the droplet size. *Colloid Polym Sci*, 278:728–735, 2000. 36, 37
- [68] Vollmer J and Vollmer D. Cascade nucleation in the phase separation of amphiphilic mixtures. *Faraday Discuss.*, 112:51–62, 1999. 37
- [69] S. A. Safran and L. A. Turkevich. Phase diagrams for microemulsions. *Phys. Rev. Lett.*, 50:1930–1933, Jun 1983. doi: 10.1103/PhysRevLett.50.1930. URL <http://link.aps.org/doi/10.1103/PhysRevLett.50.1930>. 37
- [70] S. A. Safran. *Microemulsions: an ensemble of fluctuating interfaces : Structure and Dynamics of Strongly Interacting Colloids and Supramolecular Aggregates in Solution*. Kluwer Academic Publishers, Dordrecht, 1992. 37
- [71] P. Lecomte du Noy. A new apparatus for measuring surface tension. *The Journal of General Physiology*, 1(5):521–524, 1919. doi: 10.1085/jgp.1.5.521. URL <http://jgp.rupress.org/content/1/5/521.short>. 53
- [72] 68 3 (1983) Shinoda, K. *Prog. Colloid Polym. sci.*, 68:3, 1983. 58
- [73] Tharwat F. Tadros. *Self-organised Surfactant Structures*. Wiley-VCH, 2010. 58
- [74] Schubert K.-V and Kaler E.W. Nonionic microemulsions. *Ber. Bunsenges. Phys. Chem.*, 100:190–205, 1996. 79, 80, 93
- [75] Strey R Hasse D et al. Kahlweit, M. *J. Colloid Interface Sci.*, 118:436–453, 1987. 79, 80, 93
- [76] T. Foster. *Microemulsions as compartmentalised reaction media : structural characterisation of water-in-oil microemulsions*. PhD thesis, University of Cologne, 2007. 85